12-2014

Particle scavenging by water drops in an ultrasonic standing wave field

Weiyu Ran
Clemson University, wran@g.clemson.edu

Recommended Citation

Ran, Weiyu, "Particle scavenging by water drops in an ultrasonic standing wave field" (2014). *All Dissertations*. 1446.
https://tigerprints.clemson.edu/all_dissertations/1446

Particle scavenging by water drops in an ultrasonic standing wave field

---

A Dissertation
Presented to
the Graduate School of
Clemson University

In Partial Fulfillment
of the Requirements for the Degree
Doctor of Philosophy
Mechanical Engineering

---

by
Weiyu Ran
December 2014

Accepted by:
Dr. John R. Saylor, Committee Chair
Dr. Richard S. Miller
Dr. Xiangchun Xuan
Dr. Lonny L. Thompson

Abstract

Currently the backbone of the world's energy supply is composed of fossil fuels. However, the combustion of fossil fuels results in the production of enormous quantities of particulate pollutants. The smog resulting from these particulate pollutants causes significant health problem for city dwellers. Wet scrubbers, which use a water spray to scavenge airborne particles, is one of the most widely used devices to control particulate pollutants. Typical wet scrubbers can scavenge particles with diameters bigger than 10 μm, but it is inefficient in scavenging particles with diameters on the order of 1 μm. Unfortunately these fine particles are more dangerous than the coarse particles since fine particles can penetrate deep into human lungs. This dissertation is an investigation into the use of ultrasonics to enhance the ability of wet scrubbers to scavenge fine particles.

The first part of the investigation involves testing a combination of water spray and ultrasonics on the scavenging of fine particles in a small scale scrubber. A stream of air laden with particles was flowed into the scrubber with a water spray. Experiments were conducted with and without the presence of an ultrasonic standing wave field inside the scrubber over a range of parameters: water flow rate, air flow rate, particle size and spray drop size. Compared to the water spray alone, significant increases in the scavenging of particles were observed when the water spray was combined with the standing wave field in these experiments.

The second part of the investigation involves a determination of the mechanism that causes the increase in particle scavenging of a water spray in the presence of an ultrasonic standing wave field. A review of existing theories showed that the acoustic radiation force generated by an ultrasonic standing wave field can influence the motion of the aerosols in the standing wave field. These theories predict that the spray drops used in these experiments would migrate toward the pressure nodes of the standing wave field. However, for the micron-scaled particles investigated here, some theories predict that the particles would migrate toward the pressure nodes, while other theories predict that they would migrate toward the pressure anti-nodes. Experiments were conducted where particles having a range of diameters were flowed into the region of a standing wave field and their locations in the standing wave field were recorded. Results obtained from these experiments show that the particles with diameters larger than 0.3 ± 0.1 μm would migrate toward the pressure nodes while the particles with diameters smaller than 0.3 ± 0.1 μm would migrate toward the pressure anti-nodes. A theory of the acoustic radiation force that agrees with these results was selected to build a model. This model was used to simulate the trajectories of the spray drops and the particles in the scrubber. Results obtained from the simulations show that the increased scavenging is caused by an increase in particles combining with spray drops in the pressure nodes of the standing wave field.

Acknowledgments

I would like to thank my adviser Dr. John R. Saylor, my committee Dr. Richard S. Miller, Dr. Xiangchun Xuan and Dr. Lonny L. Thompson for providing me with guidance for this thesis research. I also want to thank all of my current and former research team members: Tyler Merrell, Jie Kou, Steven Fredericks, Steven Bower, Jonathan Hodges, Rachel Sundberg-Anderson, John Isely and Jacob Kizzee for their support on this research. Especially Mr. Tyler Merrell for helping me obtaining some data that presented in Appendices of this thesis, Dr. Jie Kou for constructing some parts of the experimental setup, Mr. Steven Fredericks and Ms. Rachel Sundberg-Anderso for reviewing my thesis draft. This thesis research was funded by NIOSH and NSF whose support is gratefully acknowledged. Finally, I would like to thank Huan, my girlfriend, for your accompanying and supporting during my Ph.D. studies!

Table of Contents

List of Tables

List of Figures

Chapter 1

Introduction

Particle or aerosol emissions from fossil fuel combustion in the transportation and industrial sectors is one of the major sources of air pollutants.[1] The smog formed by these particulate pollutants has significant deleterious effects on human health. These effects include increases in the mortality rate in individuals with pulmonary[2,3] and cardiovascular[4,5,6,7] diseases and increases in the prevalence of lung cancer[8,9,10] and asthma.[11,12,13]

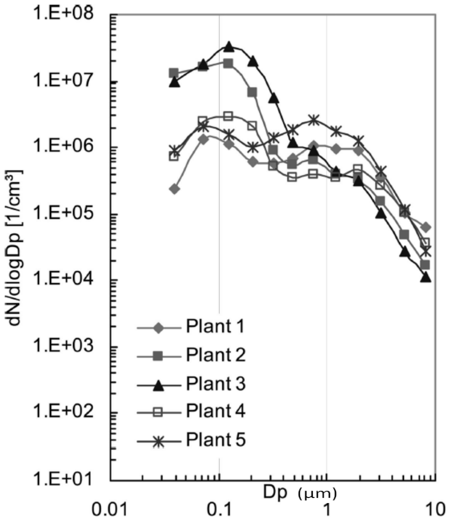

Figure 1.1: Particle size distribution (normalized particle number concentration, dNdlogDp, versus particle diameter, Dp) of untreated emissions from five typical coal-fired power plants.[14]

Particles in the smog over the world's major cities can range significantly in diameter. Particles with diameters on the order of 1 μm are believed to pose the greatest health risks[12,3] to humans and there are significant quantities of these diameters in all smogs.[15] One of major sources of these ∼1 μm particles is the coal-fired power plant[14] (see Fig 1.1). Studies show a positive correlation between daily mortality rate of city populations and the concentration of particles with diameters on the order of 1 μm in the environment.[16] The mechanism behind this correlation is still unclear; one possible explanation is deposition of particles in human lungs peaks for particle diameters slightly larger than 1 μm.[17] Although there are still some unknowns about the cause of this correlation, a method that could eliminate particles with diameters on the order of 1 μm from the sources such as coal-fired power plants would have great benefit to public health.

Particulate pollutant control technologies utilize physical processes that can remove or separate entrained particles from multi-phase gas/liquid streams. Conventional particle removal processes are gravitational settling, centrifugal separation, wet scrubbing, filtering, and electrostatic precipitation.[18] Among these, electrostatic precipitation, wet scrubbing, and filtering are the most widely used to remove particles from the pollutant streams emanating from smokestacks of coal-fired power plants and other gas-phase point sources.[19] The performance of these devices is quantified by the scavenging coefficient, E:

$$E = \frac{n_C}{n_T}, \tag{1.1}$$

where n_C is the number of particles collected by the device, and n_T is the total number of particles entering the device. Due to the significance of particle diameter on human health, among other things, the performance of particle removal devices is often compared by plotting E against particle diameter d. Figure 1.2 presents plots of E versus d obtained from the literature for the three most widely used devices for particulate pollutant control mentioned above: the electrostatic precipitator, the wet scrubber (droplet scrubber), and the filter. As this figure shows, for typical conditions, a minimum exists in E for $0.1\ \mu\text{m} \lesssim d \lesssim 10\ \mu\text{m}$ for all three kinds of particle removal devices, though they are based on different particle removal mechanisms. This decrease in collection efficiency has been verified in many other experimental and theoretical studies of electrostatic precipitators,[20, 21, 22] wet scrubbers[23, 24, 25] and filters.[26, 27]

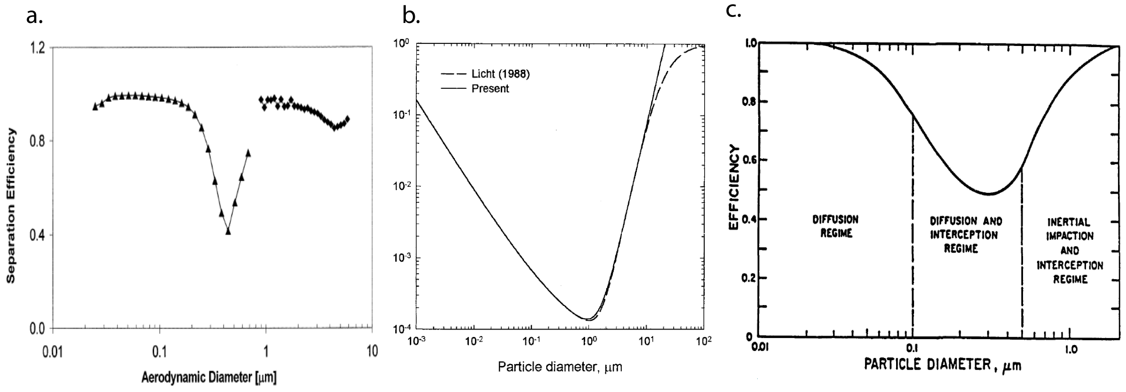

Figure 1.2: (a) Plot of E versus d for typical electrostatic precipitator.[28] (b) Plot of E versus d for typical wet scrubber.[29] (c) Plot of E versus d for typical filter.[30]

1.1 Wet scrubbers

Figure 1.3 shows the schematic diagram of a typical wet scrubber. The dirty gas enters from the bottom of the scrubber, moves upward and mixes with the spray drops. During this process particulate and gaseous pollutants are absorbed by the drops, most of these drops will then fall to the bottom of the scrubber and eventually drain out from the system. The drops that are entrained in the gas are removed by the mist eliminator, and clean gas exits from the top of the scrubber.

When compared with the electrostatic precipitator and the filter, the wet scrubber has important advantages.[31] First it is able to handle particulate pollutants regardless of their composition and condition. For example, potentially explosive particles, particles carried by high temperature gas, particles with entrained droplets, and particles composed of sticky materials can all be removed using wet scrubbers. These particles, if treated with a filter or electrostatic precipitator, could increase the danger of explosion, or could result in damage or blockage of the device. The second advantage of the wet scrubber is its ability to simultaneously remove soluble gaseous pollutants and particulate pollutants, which the filter and the electrostatic precipitator can not do. This ability is particularly useful for treating pollutants generate by coal-fired power plants, which contains gaseous pollutants such as SO_2 and NO_x in addition to particulate pollutants.[32]

Though the wet scrubber has advantages over the electrostatic precipitator and the filter, as shown in Fig. 1.2 it shares their shortcoming of ineffective removal of particles with $\mathcal{O}(1\ \mu\mathrm{m})$ diameters and, as discussed above, this overlaps with the particles that have the largest negative

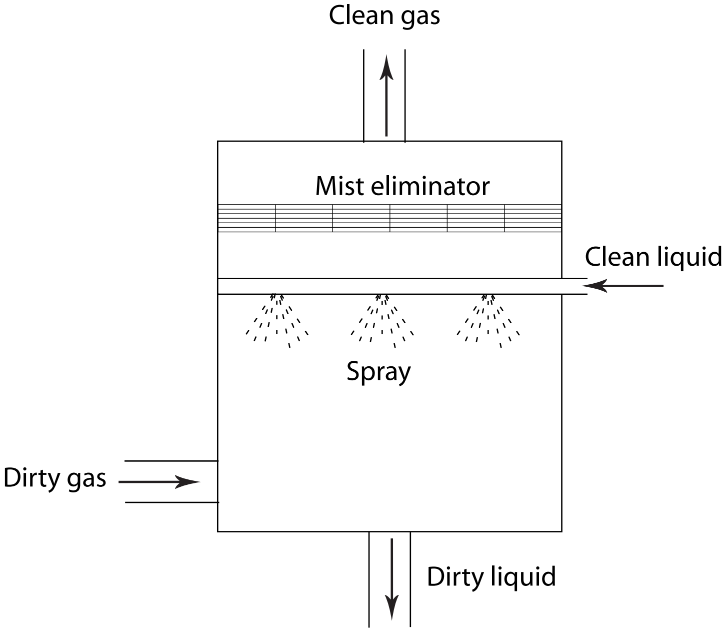

Figure 1.3: Typical wet scrubber.

impact on pulmonary health, which is on the order of 1μm. So, a method that could increase E for the wet scrubber in the micron-scale diameter range could have a significant impact on pulmonary health and fix the major shortcoming of the wet scrubber. Doing this would be a step toward developing the wet scrubber as an all-purpose device for removal of both particulate and gaseous pollutants. One of the main motivations for this thesis research is to develop a method to enable this type of improvement in the wet scrubber.

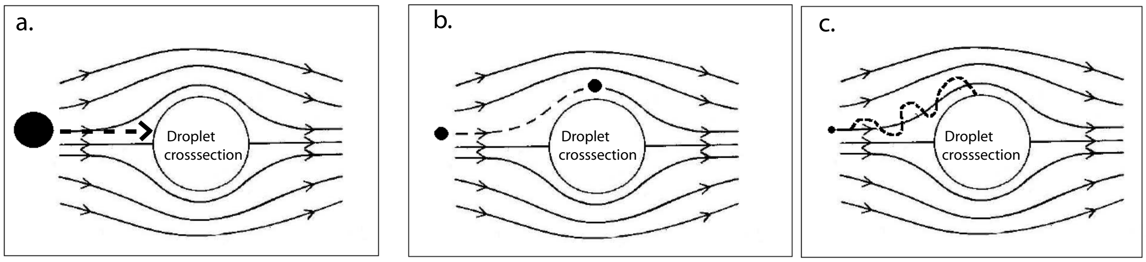

Figure 1.4: Particle collecting mechanisms of a single droplet. (a) Particle diameter much larger than ~1 μm. (b) Particle diameter between ~0.1 μm and ~1 μm. (c) Particle diameter much smaller than ~0.1 μm.

To improve the performance of wet scrubbers, one must first identify the reason why the wet scrubber is ineffective in removing micron-scale particles. The particle removal mechanism of the wet scrubber differs little from the interaction between a single particle and a single droplet. The diagram presented in Fig. 1.4 shows a particle in an air flow approaching a spherical drop. As the particle approaches the drop, it tends to follow the streamlines. However, for a particle having a large diameter, its inertia is too large to follow the flow and so the particle would collide with the drop and be removed from the flow (see Fig. 1.4(a)). For a particle that has a very small diameter, though the inertial effects are minimal, it also will not follow the streamlines because Brownian motion of the particle causes deviations from the streamlines which can also result in a collision with the drop (see Fig. 1.4(c)). Brownian motion of the particle increases with decreasing d, while the inertia of the particle increases with d. So, there is a range of d that is too big for Brownian motion to have an effect and too small for inertia to have an effect, resulting in a minimum in the chance for a particle in this diameter range to collide with the drop (see Fig. 1.4(b)). Experimental and theoretical studies of particle scavenging by a single drop,[33, 34, 35] rain[36] and wet scrubbers[23, 24, 25] show that a minimum in E occurs for d ranging from ~ 0.1 μm to $\sim$1.0 μm.

Improvements in the removal of micron-scale particles by drops (and hence improvements in scrubbers) could be achieved by introducing an additional force that acts to bring the particles and drops into close proximity. Conventional methods for particle removal utilize forces such as gravitational, centrifugal, inertial and electrostatic, to work against the aerodynamic drag force exerted on the particles, to achieve particle removal. Gravitational and centrifugal forces tend to work best for coarse particles ($d >> 10\mu$m). And as shown above, inertial forces only work for $d >> 1\mu$m. Electrostatic forces also have similar problems, the chargeability of particles decreases with d, but the mobility of the particle increases with d. Particles having diameters $0.1\ \mu\text{m} \lesssim d \lesssim 1.0\ \mu\text{m}$ fall in a range where the particle is too small to be charged significantly, but still large enough to have a low mobility.[37] That is what causes the minimum in E for electrostatic precipitators seen in Fig. 1.2.

1.2 The acoustic radiation force

Particles suspended in a fluid can be influenced by acoustic waves traveling in this fluid due to the scattering of the waves by the particles. The resulting force acting on the particles due to this scattering effect is called the acoustic radiation force. This force could possibly be used to cause micron-scale particles to combine with drops in scrubber applications. Attempts at using the acoustic radiation force for such applications have never been attempted.

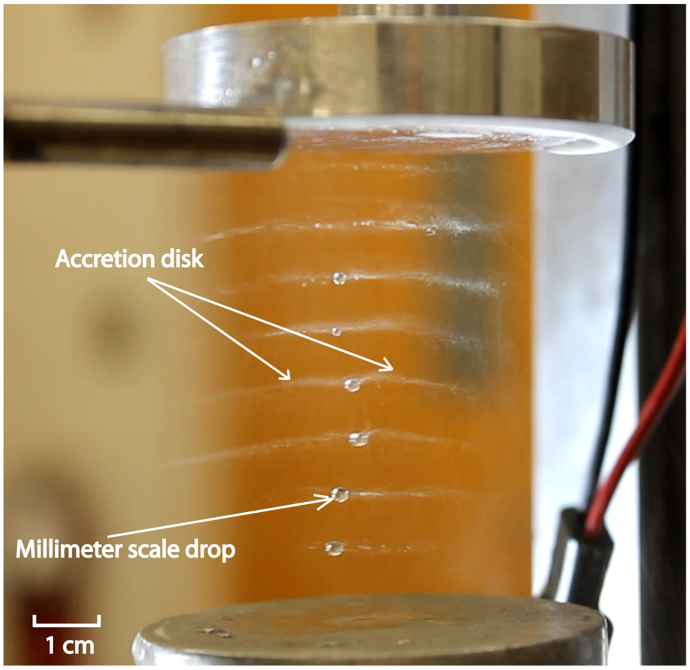

Figure 1.5: Droplets accumulate in the accretion zones of a ultrasonic standing wave field with frequency of ∼ 30 kHz. All motion is due to the acoustic radiation force. The ultrasonic transducer is the lower circular aluminum piece and the reflector is the upper circular aluminum piece. A nebulizer can be seen on the left hand side, which introduces a fine water mist into the vicinity of the standing wave field. The large drops located in the center were formed by the agglomeration of the fine water mist drops.

In this study, the acoustic radiation force is tested to find out if it can bring particles and drops into close proximity and improve the scavenging of micron-scale particles by a wet scrubber. A strong acoustic radiation force can be generated by a standing acoustic wave field,[38] which can be developed between an acoustic transducer and an acoustic reflector separated by an integer number of half wavelengths. In the standing wave field, the acoustic radiation force should act to move particles toward the pressure nodes or pressure anti-nodes of the standing wave field.[39] In this research, an ultrasonic standing wave field is used to generate the acoustic radiation force. There are two reasons for using an ultrasonic frequency. First, most studies of the acoustic radiation force are focused in the ultrasonic range (∼20kHz to ∼1MHz). Secondly, because ultrasonic frequency is beyond the audible range of humans, the future application of this technology will face less restrictions. An example of an ultrasonic standing wave field is presented in Fig. 1.5: an ultrasonic transducer and a reflector combination with an ultrasonic standing wave field between them. A fine water spray with average drop diameter on the order of 100 μm has been introduced into the general vicinity of the field (tube on upper left hand side of image), and the fine spray drops can be seen to accumulate in the pressure nodes of the standing wave, forming disk shaped accretion zones (accretion disks) due to the acoustic radiation force. In the center of these disks, enough drops have agglomerated with each other to form relatively large drops.

If the acoustic radiation force could also drive micron-scale particles into the accretion disks, the phenomenon shown in Fig. 1.5 should cause particles and drops to come into close proximity with each other, increasing the chance for a drop to scavenge a particle.

1.3 Theories of the acoustic radiation force

In order to find out whether the acoustic radiation force can also drive micron-scale particles to migrate to the pressure nodes, a review of the theories that predict the acoustic radiation force is presented below. It is noted that what follows pertains to both particles and drops. The word "particle" is used to generically refer to both particles and drops when discussing theories of the acoustic radiation force.

The theoretical study of the acoustic radiation force generated by standing acoustic waves dates back to King[38] in 1934. Later this theory was further developed by Gor′kov[40] to accommodate arbitrary acoustic fields and by Hasegawa and Yosioka[41] to calculate the force on compressible particles. However the above theories all utilize the inviscid fluid assumption; the dissipation effect of the surrounding fluid medium is neglected. This assumption is reasonable only when the particle size is much larger than the thickness of the acoustic boundary layer, δ:[42]

$$\delta = \sqrt{\frac{2\nu}{\omega}} \tag{1.2}$$

where ν is the kinematic viscosity of the surrounding fluid medium, and ω is the angular frequency of the acoustic field. For particle diameters comparable to or smaller than δ, the inviscid fluid assumption becomes invalid due to the presence of the boundary layer and the effect of streaming around the particle. Herein ultrasonic frequencies of $\sim$ 30 kHz are considered where $\delta \sim 13$ μm in air. Hence, for micron-scale particles, the inviscid assumption is not valid.

The effect of viscosity on the acoustic radiation force has been considered by Doinikov,[43] Danilov and Mironov,[44] and Settnes and Bruus.[42] The acoustic radiation force of a standing wave field predicted by these authors has the general functional form:

$$F_{ar} = C\Phi k d^3 E_{ac} sin(2kz) \tag{1.3}$$

Where F_{ar} is the acoustic radiation force generated by a standing wave on a particle, z is the position on the central axis in the standing wave field, E_{ac} is the acoustic energy density, d is the particle diameter, k is the wave number, $k = 2\pi/\lambda$, where λ is the wavelength, and Φ is the acoustophoretic contrast factor, which is a function of the material properties of the particle and the surrounding fluid medium, the particle size, and the frequency of the standing wave, and C is a constant. The value of C and the functional form of Φ are different for each theory. The results of these authors can be compared by modifying Eq. (1.3) to create a dimensionless acoustic radiation force $\mathcal{F}$:

$$\mathcal{F} = \frac{F_{ar}}{sin(2kz) E_{ac} A} \tag{1.4}$$

where A is the particle cross-sectional area. The non-dimensionalized acoustic radiation force $\mathcal{F}$ defined in this way is independent of the acoustic energy density of the standing wave field and the position of the particle in the field; it only depends on the material properties of the particle and the surrounding fluid medium, the particle size and the frequency of the standing wave. The particle diameter can also be scaled to create a dimensionless quantity. The non-dimensionalized particle diameter d_0 is defined as:

$$d_0 = \frac{d}{\delta} \tag{1.5}$$

The utility of d_0 is that: first, d_0 can determine whether the acoustic radiation force is dependent on the viscosity of the surrounding fluid medium at that diameter. If $d_0 >> 1$ that means the effect of viscosity can be ignored, if otherwise, that means the viscosity should be considered. Second, as will be shown below, the theory of Doinikov[43] and Danilov & Mironov[44] only applies for certain range of d_0.

Figure 1.6 is a plot of $\mathcal{F}$ versus d_0 for the theories of Doinikov,[43] Danilov & Mironov,[44] and Settnes & Bruus.[42] The plot shows that the theories by Doinikov[43] and Settnes & Bruus[42] exhibit reasonable agreement for $d_0 > 1$ (the theory by Danilov & Mironov[44] does not extend above $d_0 = 1$), where the theories are well-studied and where experimental data has been obtained and

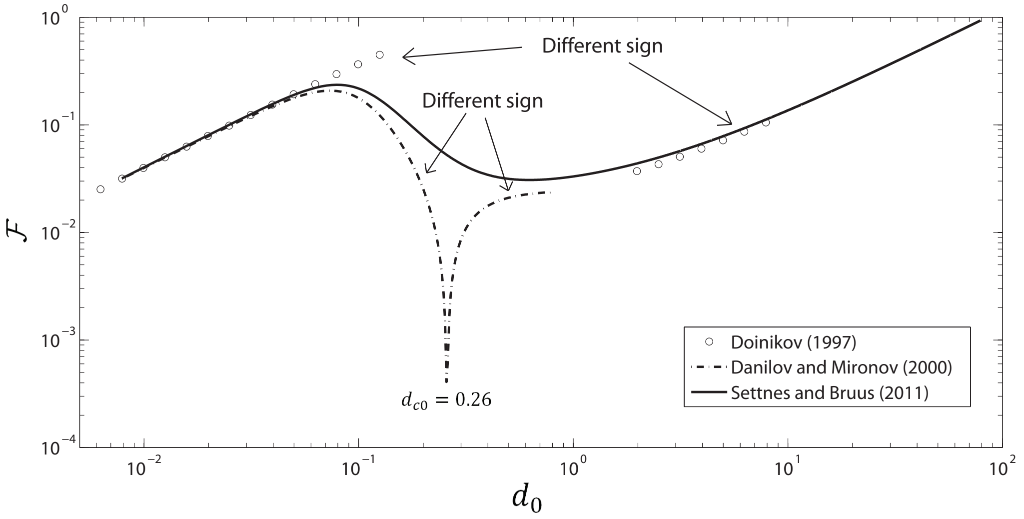

Figure 1.6: Acoustic radiation force on a water drop generated by a standing wave field at a frequency of 30 kHz in air as predicted by the theories of Doinikov,[43] Danilov and Mironov[44] and Settnes and Bruus.[42] Arrows indicate regions where the sign of $\mathcal{F}$ is different. The critical non-dimensional diameters at which $\mathcal{F}$ changes sign is d_{c0}.

used to validate them.[45] However, for the diameter range $d_0 < 1$, these theories' prediction of $\mathcal{F}$ deviate significantly from each other, not only in magnitude but also in sign. The theories of Doinikov[43] and Danilov & Mironov[44] predict a change in the sign of $\mathcal{F}$ at intermediate d_0, as shown in Fig. 1.6. Negative $\mathcal{F}$ can not be plotted in log-log space so the arrows in Fig. 1.6 are used to indicate regions of different sign. On the other hand, no sign change is predicted by the theory of Settnes & Bruus.[42] Here, d_c and d_{c0} are defined as the dimensional and dimensionless diameters at which the sign change occurs, respectively. The diameter at which a sign change occurs for the theory of Danilov & Mironov[44] is $d_{c0} = 0.26$. The gap in Doinikov's[43] theory is due to the fact that it only applies for $d_0 << 1$ and $d_0 >> 1$, hence a value of d_c cannot be obtained for this theory. A sign change in $\mathcal{F}$ means the stable position for the particle in the standing wave will change from the pressure nodes to the pressure anti-nodes or vice versa depending on the material properties of the particle and the surrounding fluid.

The presence or absence of a sign change in $\mathcal{F}$ is critical to this thesis research, as is now described. Figure 1.7 shows two scenarios where the sign of $\mathcal{F}$ is independent or dependent on the particle diameter. For a standing wave field generated between a transducer and a reflector separated by two half wavelengths, a pressure node and two pressure anti-nodes will form. If the sign of $\mathcal{F}$ is independent of the particle size, then as Fig. 1.7(a) shows, all particles, regardless of their size, as

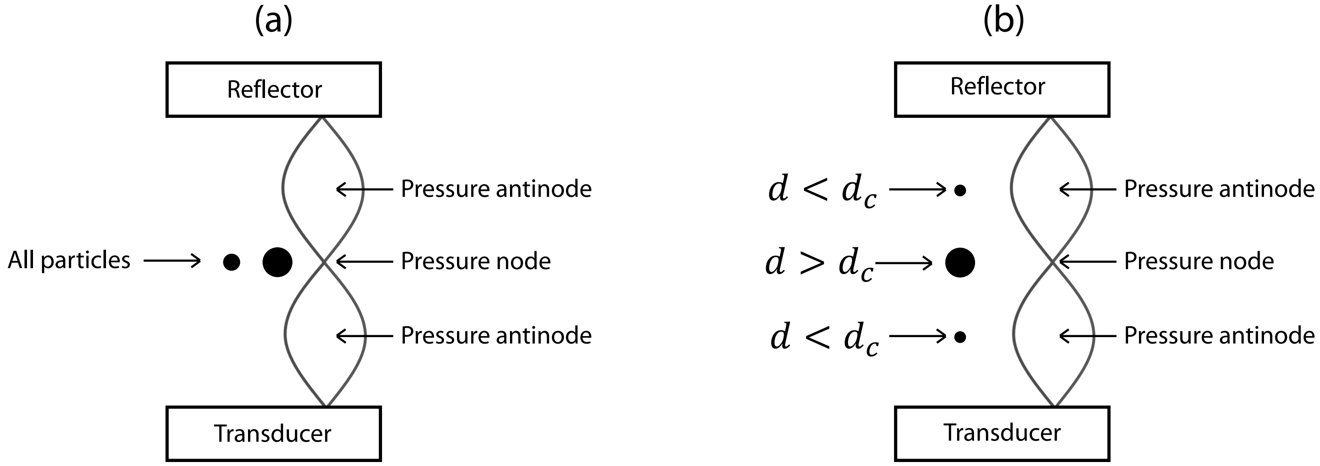

Figure 1.7: Schematic illustration showing how a change in the sign of $\mathcal{F}$ affects the location of particles in an ultrasonic standing wave field. (a): The sign of $\mathcal{F}$ is independent of the particle size. (b): The sign of $\mathcal{F}$ is dependent on the particle size.

long as they have same material properties, will go to the pressure node in the standing wave field. If the sign of $\mathcal{F}$ is dependent on the particle size, then as Fig. 1.7(b) shows those particles larger than the d_c will go to the pressure node, and particles that are smaller than d_c will go to the pressure anti-nodes. The difference between these two cases is critical. If what is shown in Fig. 1.7(b) is the case, then it is possible that use of an ultrasonic standing wave field could actually separate the (larger) water drops from the particles, worsening the scavenging capability of water sprays.

There are no experimental studies in the literature that prove or disprove any of the three viscous theories presented in Fig. 1.6 for the range $d_0 < 1$. An experimental study was conducted by Barnkob[45] which validated the theory of Settnes and Bruus[42] down to $d_0 \sim 1$. No sign change was observed in that work. For the current study the frequency of the standing wave is around 30 kHz and the surrounding fluid medium is air, $\delta \sim 13$ μm. This means that for a micron-scale particle, $d_0 \sim 0.08$. So, as shown in Fig. 1.6, if the theory by Settnes and Bruus[42] is correct, then the micron-scale particles should migrate to the pressure nodes along with the spray drops which are on the order of 100 μm, therefore, potentially improving the scavenging capability of water sprays. If the theory of Danilov and Mironov[44] is correct, then the micron-scale particles should migrate to the pressure anti-nodes. Then these micron-scale particles would be separated from the spray drops, potentially reducing the scavenging capability of water sprays. This uncertainty in the current state of understanding of the acoustic radiation force prevents a determination as to whether the acoustic radiation force can drive micron-scale particles to migrate to pressure nodes in a similar fashion as it drives fine water droplets on the order of 100 μm as shown in Fig. 1.5. It is critical to resolve this uncertainty in order to evaluate the potential of the acoustic radiation force in improving the scavenging capability of water sprays.

1.4 Goal

This introduction has showed that the wet scrubber has many advantages over other widely used particulate pollutant control devices, but it also has a major shortcoming of ineffective removal of micron-scale particles, which are a significant threat to the pulmonary health of humans. The above sections also showed that an ultrasonic standing wave field could potentially be used to improve the performance of the wet scrubber. Specifically the acoustic radiation force generated by an ultrasonic standing wave field can move water drops on the order of 100 μm into the pressure nodes. However based on the current understanding of the acoustic radiation force, it is not clear whether micron-scale particles would also be moved into the pressure nodes.

The goal of the present thesis is to:

(1) Ascertain if an ultrasonic standing wave field could improve the scavenging of micron-scale particles by water sprays, and hence potentially improve the performance of wet scrubbers.

(2) Find out how the different operating conditions of a wet scrubber affect the improvement, if it exists. The long term motivation of this research is to develop a method that could be used to improve the performance of wet scrubbers. So, in addition to ascertaining if an ultrasonic standing wave field could improve the scavenging of micron-scale particles by a wet scrubber, it would also be beneficial to determine how such a field performs under different operating conditions, such as: spray water flow rate, gas flow rate, particle size and spray drop size. And by analyzing its performance under these conditions, it may also help to reveal the mechanism of any observed improvements.

(3) Find out if there is a direction change in the acoustic radiation force at a critical diameter d_c. The motivation of this goal is twofold. First, to simply improve understanding of this important force. Secondly, to determine if the acoustic radiation force can drive micron-scale particles to migrate to the pressure nodes in a similar fashion as it drives fine water droplets on the order of 100 μm shown in Fig. 1.5 to accumulate in the pressure nodes. This is critical because even if improvement is observed in goals (1) and (2), it may not be clear why improved scavenging occurred and whether it would continue to do so with drop or particle diameters outside of the range explored

in goals (1) and (2). So, a better understanding of the directionality of the acoustic force would lay a foundation to answer the following questions: (i) what is the mechanism that causes the improvement of the scavenging? (ii) under what conditions can the acoustic radiation force be used to improve the particle scavenging?

(4) Determine the mechanism that causes the improvement of the scavenging of micron-scale particles by a combination of an ultrasonic standing wave field and water drops, if it exists.

Chapter 2

The Ultrasonic Wet Scrubber: Experiments and Results

In this chapter, the feasibility of improving the scavenging of micron-scale particles by water sprays coupled with an ultrasonic standing wave field is investigated using an ultrasonic wet scrubber. An experimental study of this ultrasonic wet scrubber is described, including the setup (Section 2.1), the procedure (Section 2.2), the data processing (Section 2.3) and the results (Section 2.4). The goal of these experiments was to determine E for this ultrasonic wet scrubber over a range of parameters: water flow rate, air flow rate, particle size and spray drop size. For each of these parameters, experiments were conducted with and without the imposition of an ultrasonic standing wave, allowing a determination of whether that field improved scavenging.

2.1 Setup

The overall view of the experimental setup is shown in Fig. 2.1. The setup is composed of five main parts: an ultrasonic wet scrubber, an aerosol generation and conditioning apparatus, particle counters and a particle size distribution measurement apparatus and a spray drop size distribution measurement apparatus.

The heart of this setup is the ultrasonic wet scrubber (dashed box in Fig. 2.1 and expanded in Fig. 2.2). The function of the ultrasonic wet scrubber is to create an enclosed environment where

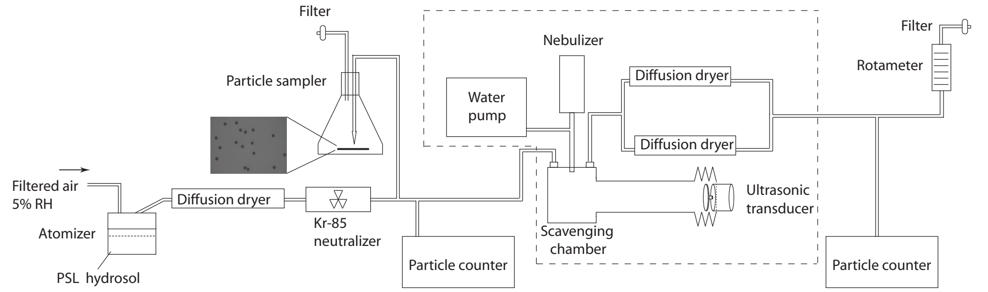

Figure 2.1: Overall view of the experimental setup.

an ultrasonic field can interact with a water spray and particle stream. This scrubber consists primarily of a small chamber equipped with a nebulizer on top, an inlet and outlet for the particle laden air. Inside the chamber, an ultrasonic field can be established. The ultrasonic wet scrubber is described in detail in Section 2.1.1.

The aerosol generation and conditioning apparatus is located upstream of the ultrasonic wet scrubber. It is composed of an atomizer, a diffusion dryer and a neutralizer. The function of the aerosol generation and conditioning apparatus is to generate a stable aerosol containing monodisperse particles with a controllable diameter. The detailed description of this apparatus is presented in Section 2.1.2.

Identical particle counters were located upstream and downstream of the ultrasonic wet scrubber. Their main function is to sample a portion of the flow from the main setup and count the number of particles in that flow. The scavenging coefficient of the ultrasonic wet scrubber was calculated based on these particle counter measurements. The detailed description of the particle counters is presented in Section 2.1.3.

The particle size distribution measurement apparatus includes a particle sampler located between the neutralizer and the upstream particle counter as shown in Fig. 2.1. The particle size distribution measurement apparatus also includes other parts such as a microscope and a digital camera that are not shown in Fig. 2.1. The detailed description of the particle size distribution measurement apparatus is presented in Section 2.1.4. The spray drop size distribution measurement apparatus includes the same microscope and the digital camera used in particle size measurement and other parts that are described in Section 2.1.5.

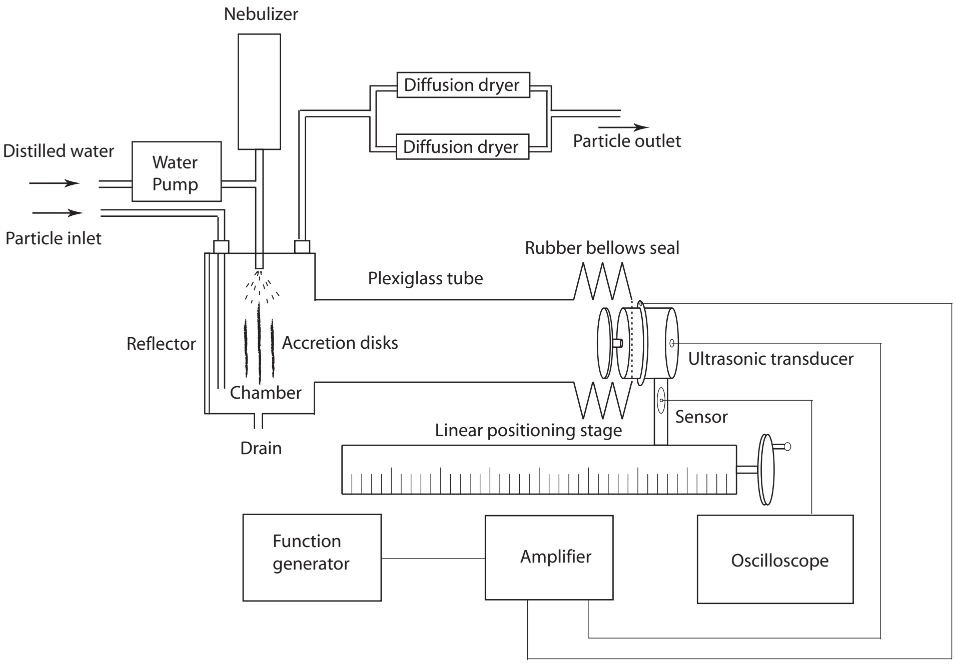

Figure 2.2: Ultrasonic wet scrubber (expanded view of dashed box in Fig. 2.1).

2.1.1 Ultrasonic wet scrubber

A detailed view of the ultrasonic wet scrubber is shown in Fig. 2.2. The ultrasonic wet scrubber is mainly composed of a rectangular chamber, a plexiglass tube and an ultrasonic transducer. The chamber is the location where particle scavenging actually occurs, so it is referred to as a scavenging chamber hereinafter. The volume of the scavenging chamber is 370 cm^3. Detailed size and geometry of the scavenging chamber is presented in Fig. 2.3. As shown in Figs. 2.2 and 2.3, there are three small ports on the top of the scavenging chamber; the two on the side are the inlet and outlet for particle laden air and the one in the middle is the inlet for the water spray. Particle laden air was introduced through the particle inlet port and was directed to the bottom of the chamber by a pipe to avoid any flow stagnation zone at the bottom of the chamber. The particle laden air exited the chamber through the particle outlet port. Spray was introduced through the spray port by an ultrasonic nebulizer (Sonics & Materials. Inc. Model VCX 134 FSJ). The ultrasonic nebulizer was mounted on the top of the scavenging chamber. Unlike conventional pneumatic nebulizers that rely on compressed gas to shear a fluid into small drops, the ultrasonic nebulizer uses only ultrasonic vibrational energy to generate a spray. It has been proven in preliminary experiments that the ultrasonic vibrational energy generated by the nebulizer was confined within the nozzle of the nebulizer;

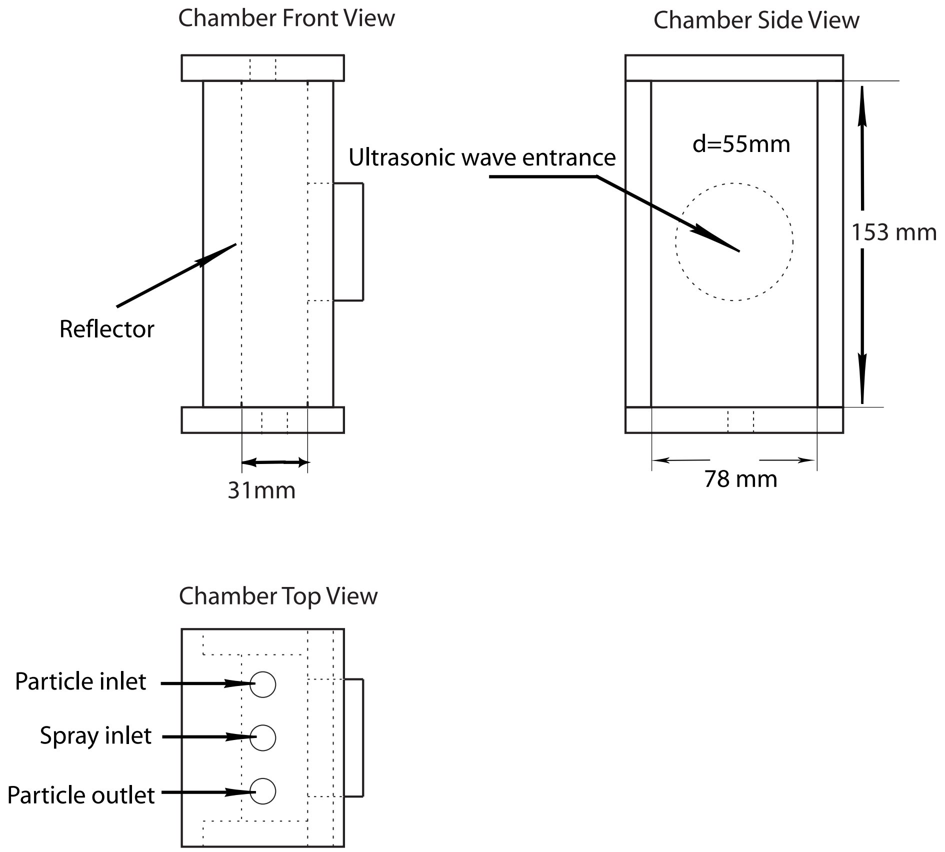

Figure 2.3: Detailed view of the scavenging chamber. The dimensions of this chamber are 153 mm × 78 mm × 31 mm.

it did not interact with the ultrasonic standing wave field created by the transducer. This check was done by using a piezoelectric vibration sensor, located inside the scavenging chamber, to detect the sound pressure generated by the nebulizer. The sensor showed the sound pressure generated by the nebulizer was negligible compared to that of the standing wave field created by the transducer. The spray droplet size distribution of the nebulizer was varied by adjusting the power delivered to the nebulizer (details on the drop size distribution are presented in Section 2.4). The water flow rate Q_l for the spray was precisely controlled using a peristaltic pump (Masterflex L/S pump drive 7554-90 with L/S Easy Load II pump head 77200-62).

As shown in Figs. 2.2 and 2.3, in addition to the three ports on the top of the scavenging chamber, there is also one small port on the bottom of the chamber and one big port on the side of the chamber. The port on the bottom of the chamber was used to drain accumulated water from the spray. The big port on the side of the chamber was the entrance for the ultrasonic wave. The ultrasonic wave emitted from the transducer was conducted into the scavenging chamber through a plexiglass tube. The tube has a length of 25 cm and a diameter of 5.5 cm. The standing wave field was established between a brass reflector plate (which is also the left side wall of the scavenging chamber, as shown in Figs. 2.2 and 2.3) and the transducer. The reason for placing this plexiglass tube between the transducer and the reflector were: first, to provide an airtight path from the transducer to the reflector; second, to recess the transducer away from the spray to ensure that the transducer did not make contact with the spray drops. The reason for preventing spray drops from making contact with the transducer was that spray drops that landed on the transducer surface would re-atomize. If these drops contained scavenged particles, then there is a possibility that these particles would be reintroduced back into the air in the scavenging chamber, causing errors in E.

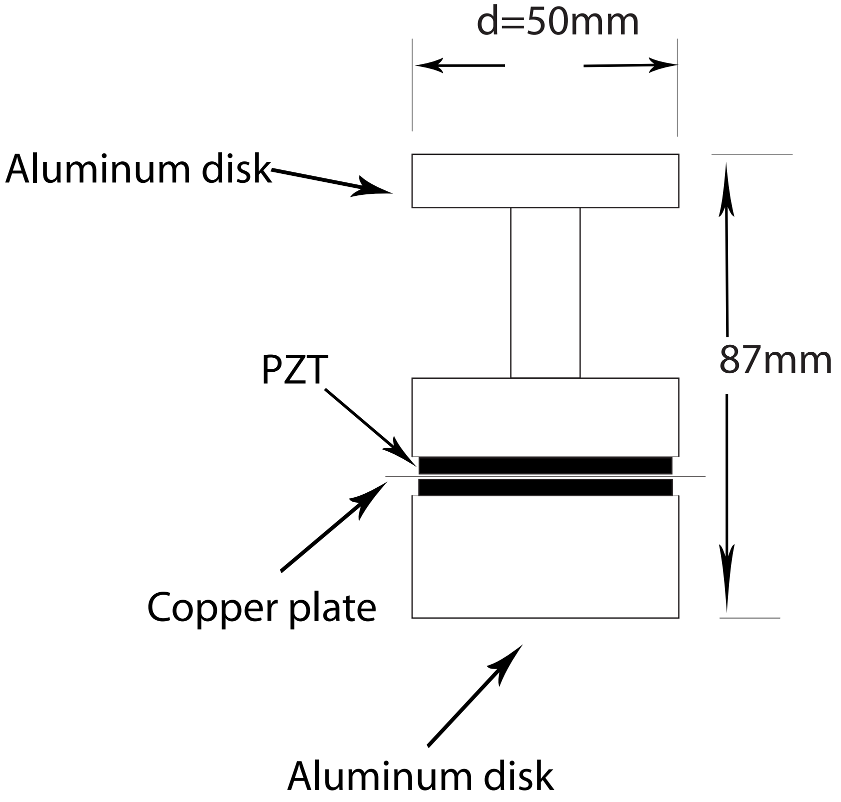

Figure 2.4: Schematic of the ultrasonic transducer used in these experiments.

The ultrasonic transducer was connecting to the plexiglass tube using a rubber bellows seal. This seal ensured the connection was airtight and also flexible which was important since adjustment of the location of the transducer is critical to maintain the standing wave field. The transducer was based on the design of Trinh[46] and is by itself illustrated in Fig. 2.4. As shown in the figure, the main body of the transducer is composed of two thick aluminum disks, two thin piezoelectric lead-zirconate-titanate (PZT) disks and one copper plate; they were stacked together and fixed by a bolt that runs through the center of them. One electrode of each transducer was the copper plate and the other electrode was the aluminum disk located at the bottom or top of the transducer shown in Fig. 2.4. When a sinusoidal voltage was sent to the two electrodes, the PZT would contract and expand periodically, causing the transducer to vibrate and emit an ultrasonic wave from the top aluminum disk. The transducer based on this design, and with dimensions presented in Fig. 2.4, has a resonant vibration frequency of $\sim$ 30 kHz. The transducer emits effectively at frequencies near this resonant value, and this is the approximate frequency used for the experiments (this number is approximate since the natural frequency varies with temperature). The sinusoidal voltage was generated by a function generator (Agilent 33220A) and was amplified by a Krohn-Hite 7500 amplifer before delivered to the transducer. During the experiment, the amplitude of the sinusoidal voltage applied to the transducer was typically set to 90 volts. Higher voltages caused the transducer to overheat and become unstable. Before the experiment, a piezoelectric sensor was attached to the back of the transducer and its output displayed on an oscilloscope (Tektronix TDS 210). This sensor was used to tune the transducer into resonance by adjusting the frequency of the sinusoidal voltage applied to the transducer until a maximum was observed, indicating that resonance had been attained. Once this was done, the next step was to tune the distance z between the tip of the transducer and the reflector plate. A standing wave will be attained when z is an integer number of half wavelengths of the ultrasonic wave:

$$z = \frac{n\lambda}{2} \tag{2.1}$$

where λ is the ultrasonic wave length obtained from:

$$\lambda = \frac{c}{f} \tag{2.2}$$

and c is the sound speed. As shown in Fig. 2.2, z can be tuned by adjusting the linear positioning stage (Velmex, A60) on which the transducer was mounted. The initial z was obtained from Eqs. (2.1) and (2.2). The z obtained from these equations is not precise because the local sound speed c varies with temperature and pressure, and a method for fine-tuning is needed. This was done by turning on the water spray and adjusting the gap distance until the fine water drops accumulated in the pressure nodes and formed accretion disks as illustrated in Fig. 2.2. The appearance of the accretion disks indicated a standing wave field had been attained between the gap.

The whole assembly, including the scavenging chamber, the plexiglass tube and the emitting part of the transducer, was airtight except for the inlet and outlet for particle laden air flow. For the water drain, a layer of water thicker than 1 cm was always present at the bottom of the scavenging chamber which prevented air from leaking out from the water drain. The air flow rate in the scavenging chamber was varied by adjusting a valve connected to the filtered shop air that was used to convect particles. An air rotameter (OMEGA Engineering, INC.), located at the very downstream end of the entire setup (shown in Fig. 2.1), was used to measure the air flow rate of the scavenging chamber.

Because the particle counters can not distinguish between particles and water droplets, it was critical that all water was eliminated before the entrance to each counter. To ensure this, two diffusion dryers (ATI DD250) were placed between the scavenging chamber and the downstream particle counter to eliminate any liquid water droplet entrained in the flow. The detailed procedure of checking whether the diffusion dryers eliminated all liquid water droplets entrained in the flow is presented in the procedure section (Section 2.2).

2.1.2 Aerosol generation and conditioning system

The aerosol generation apparatus used in these experiments was an pneumatic atomizer (TSI 9302). The particle source used in this atomizer was a hydrosol containing monodisperse polystyrene latex (PSL) microspheres. By atomizing the hydrosol containing these spheres and evaporating the remaining water, an aerosol containing monodisperse PSL particles can be formed as long as the atomized drops had only one PSL sphere per drop. The detailed description of how to ensure that there were no doublets or triplets of PSL spheres formed during this process is presented in Section 2.3.1.

There were three reasons for selecting PSL for the particles investigated in this thesis research: First, these particles are uniform in shape and size, therefore, it is very easy to quantify their diameters. Second, PSL particles are stable when in contact with water. In preliminary experiments, sodium chloride particles were used, however this created problems when phase transformation and growth occurred on the salt particles when they were exposed to high humidity environments inside the ultrasonic wet scrubber. Also very small salt particles that could not be detected by the particle counter upstream of the ultrasonic wet scrubber, would grow in the ultrasonic wet scrubber and were counted by the particle counter downstream of the ultrasonic wet scrubber, and the particle counter data did not reflect the true scavenging coefficient. Third, the laser particle counters used in these experiments are very sensitive to PSL particles.[47]

The original PSL hydrosol was supplied by Spherotech Inc. in a high concentration formulation that most likely contained agglomerated PSL particles and soluble impurities. Therefore, additional processing was needed before the PSL hydrosol from the manufacturer could be used in the atomizer. The first step was diluting the hydrosol using distilled water. After dilution the particles were washed using a centrifuge (Unico PowerSpin VX C818). During the centrifugal process, the PSL particles suspended in water were separated out by the centrifugal force and moved to the bottom of the container, after which the water (that may have contained impurities) was decanted. Finally, the resulting hydrosol was sonicated for five minutes in an ultrasonic cleaner (Fisher Scientific FS20H) to disperse any agglomerated PSL particles. After that, the hydrosol was ready for use in the atomizer. After the hydrosol was fed into the atomizer and atomized into a mist, the mist was convected through the experimental apparatus via a flow of clean dry air into the particle conditioning apparatus, which was composed of a diffusion dryer (ATI DD250) and a neutralizer (TSI 3012). In most cases the dry air evaporated the water drops containing PSL spheres, but to ensure that all water was removed, the flow was passed through the diffusion dryer to remove any remaining moisture.

PSL aerosols formed using this method have been shown to contain significant static charge.[48] To eliminate any potential charging problems, a neutralizer was used. The neutralizer used here is a steel tube containing a 74×10^6 Bq Kr-85 radioactive source. The particles were flowed through the tube and exposed to the radiation, eliminating charge on the particles. After the neutralizer, the PSL particles was deemed to be dry, charge free, and ready to be sampled for particle size and number measurement.

2.1.3 The particle counters

As shown in Fig. 2.1, two identical laser particle counters (Hach Ultra Analytics Inc., Met One 237A), located upstream and downstream of the ultrasonic wet scrubber, were used to sample a portion of the particle laden flow and count the particles in that flow. The basic operating principle of the laser particle counter involves a photo-detector to detect light scattered from a particle, while the particle travels through the sensing zone. Whenever a particle travels through the sensing zone the photo-detector will generate a voltage pulse. This pulse will be registered by a signal processor and counted as a particle. In principle the particle counter can only count one particle in the sensing zone at a time. When more than one particle enters the sensing zone at the same time, only one pulse is registered resulting in a coincidence error. The effect of this error and its uncertainty on the measurement of E is described in detail in the data processing section (Section 2.3.4).

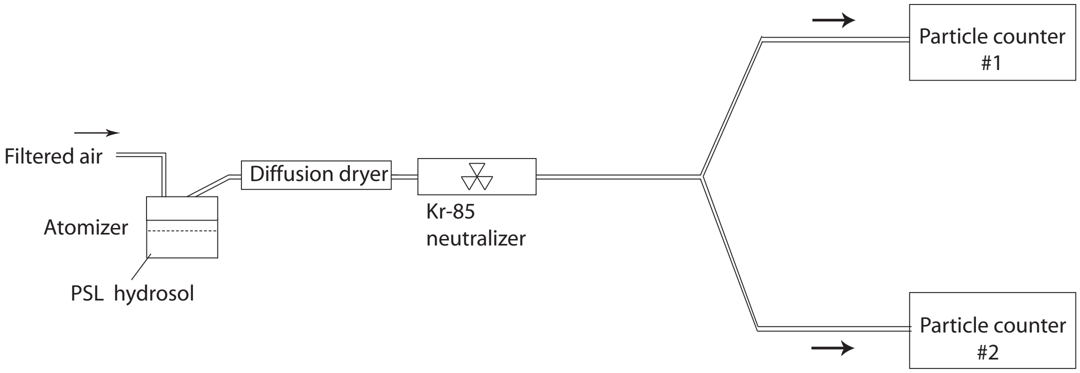

Figure 2.5: Setup used to compare the readings of two particle counters counting particles from the same particle source

The particle counters used here have a sensing zone of approximately 0.21×10^{-9} m^3 and is capable of detecting particles larger than 0.5 μm, its sampling flow rate is 50 cm^3/s. Both particle counters have been calibrated by the manufacturer for their particle detecting ability and their sampling flow rate. In principle, for a particle source composed of particles larger than 0.5 μm, both particle counters should give identical readings if the particle flow paths connecting the particle source and both particle counters are identical. A test of this was conducted using the setup shown in Fig. 2.5. The two particle counters were connected to the aerosol generation and conditioning system (described in Section 2.1.2) through tubes of equal length. During the test, PSL particles on the order of one micron were fed to the aerosol generator. The result of this test is presented in Fig. 2.6, which shows the readings of the two particle counters matched each other over wide ranges of particle concentrations. The average of the absolute value of difference in counts for the data presented in Fig. 2.6 was 23 counts which is a 0.4% error.

When using the configuration shown in Fig. 2.1 to do the same test described above, even when the spray in the ultrasonic scrubber was off during this test, the readings of the two particle

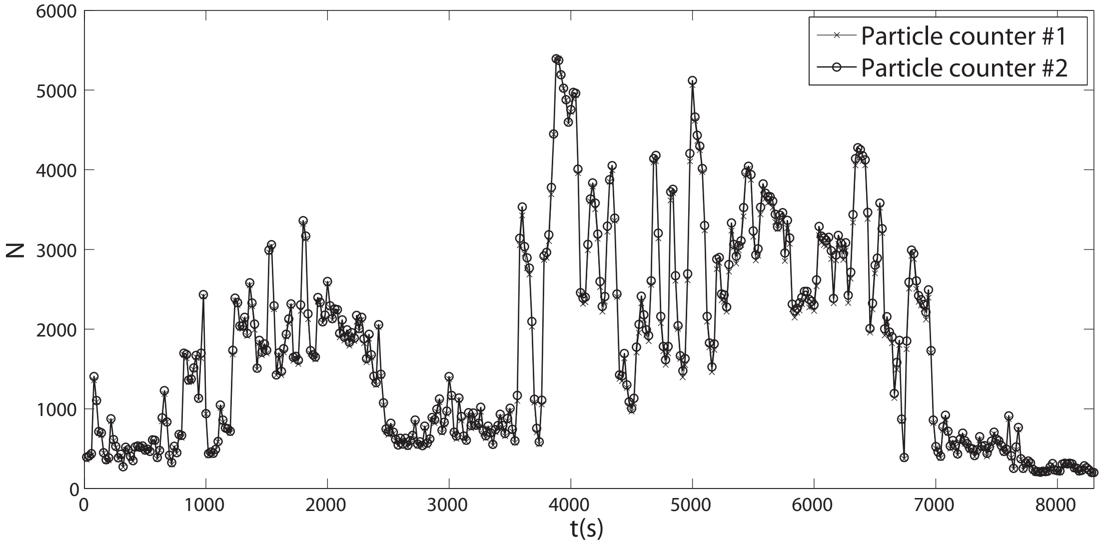

Figure 2.6: Particle counts (N) versus time (t) for the two particle counters sampling particles from the same flow (see Fig. 2.5).

counters did not match each other, as shown in Fig. 2.7. This is because in this configuration the particle flow paths, connecting each particle counter to the particle source, were very different. Figure 2.7 shows that the readings of the downstream particle counter always lag behind the readings of the upstream particle counter as expected since time is needed to travel from the upstream counter to the downstream counter. Figure 2.7 also shows that the downstream particle counter reads lower than the upstream particle counter. This is because there were particles deposited on the pipe wall. Due to this particle deposition loss, the particle number counts are lower downstream than upstream. These two differences need to be addressed in order to obtain meaningful measurements of E.

To address the first difference, the data from the two particle counters were shifted in time with respect to each other, ensuring that calculation of E was not affected by the time lag between the readings of the particle counters. The details are presented in the data processing section (Section 2.3.4). To address the second difference, the particle loss due to deposition was measured separately in every experimental run, and this loss was accounted for and eliminated in the data processing ensuring that E is solely due to droplet scavenging. The details are presented in the procedure section (Section 2.2) and data processing section (Section 2.3.4).

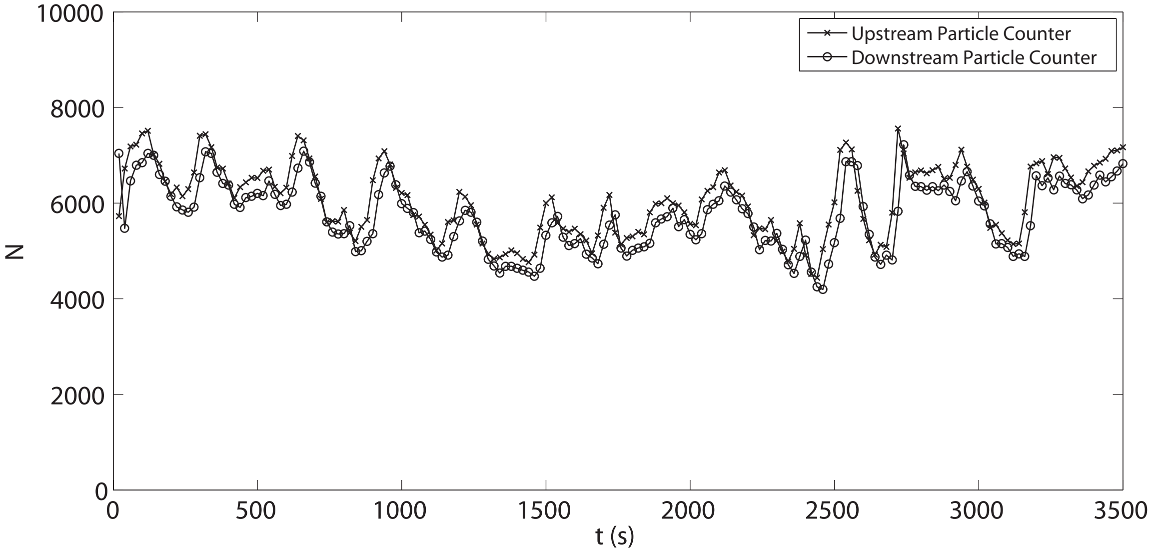

Figure 2.7: Particle counts (N) versus time (t) for the two particle counters. The spray in the ultrasonic scrubber was off in this case.

2.1.4 The particle size distribution measurement system

To measure the size distribution of the PSL particles, a portion of the particle laden flow just downstream of the neutralizer was sampled by a particle sampler as shown in Fig. 2.1. The particle sampler is essentially an Erlenmeyer flask with a clean microscope slide located at its bottom. A nozzle with a diameter of ~ 2 mm was located inside the flask was used to concentrate the particle laden flow into a jet with a velocity on the order of 1 m/s. The jet impacted the microscope slide, where particles were collected. The microscope slide was exposed to this jet flow during the entire course of an experimental run.

The diameters of the particles collected on the microscope slide were measured optically using a Leica (DM750) microscope having a digital camera mount. A digital camera (Canon DS126291) with 12 mega pixels was mounted on the microscope. This camera was used to evenly sample images of particles at different locations on each microscope slide. Particles collected on different parts of a glass slide were imaged for each experiment. The number of particles recorded for each experiment varied but typically fell in the range of 2000 to 4000 particles. The system was calibrated using a separate image of a ruler. The image of the ruler was used to generate a micron/pixel conversion. This conversion factor varied from 0.02 μm/pixel to 0.05 μm/pixel depending on the objective lens used. With this conversion factor, the actual particle diameters were obtained from the image.

An image processing algorithm was developed to obtain the diameter of the particles. A detailed description of these processes and the resulting particle size distributions of the PSL particles are presented in Section 2.3.1.

Another set of experiments were run where the particles naturally in the laboratory air were used as a particle source. When this was done, the whole aerosol generation and conditioning system and the particle sampler shown in Fig. 2.1 were removed and the pipe inlet prior to the upstream particle counter was exposed to the ambient environment as shown in Fig. 2.8. The flow through the system was due to the pumps in the particle counters.

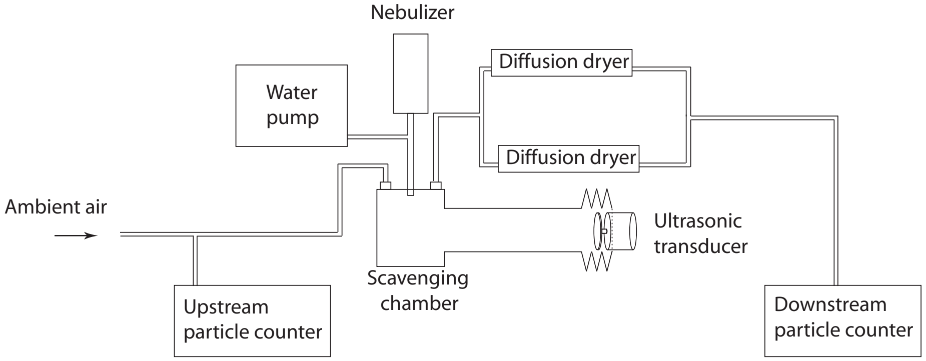

Figure 2.8: The overview of the experimental setup when ambient air particles were used.

The distribution in particle diameters for this ambient air was obtained using the upstream particle counter which is capable of crude particle diameter measurement. The particle counters used here can sort particle in six size bins: 0.5-0.7 μm , 0.7-1.0 μm , 1.0-2.0 μm, 2.0-3.0 μm, 3.0-5.0 μm and >5.0 μm. This resolution is much lower than the microscope imaging system. The reason that the microscope imaging system used for the PSL diameter measurement was not used for the ambient air particles was because ambient air particles often have irregular shapes and some were partially transparent under the microscope. A detailed description about using the records generated by the upstream particle counter to obtain the distribution of ambient air particles and the resulting particle size distribution of the ambient air particles are presented in Section 2.3.2. Due to the variability of the ambient particle concentration from day to day in the laboratory and the fact that it is difficult to control the properties of these particles, ambient particles were only used in some preliminary experiments.

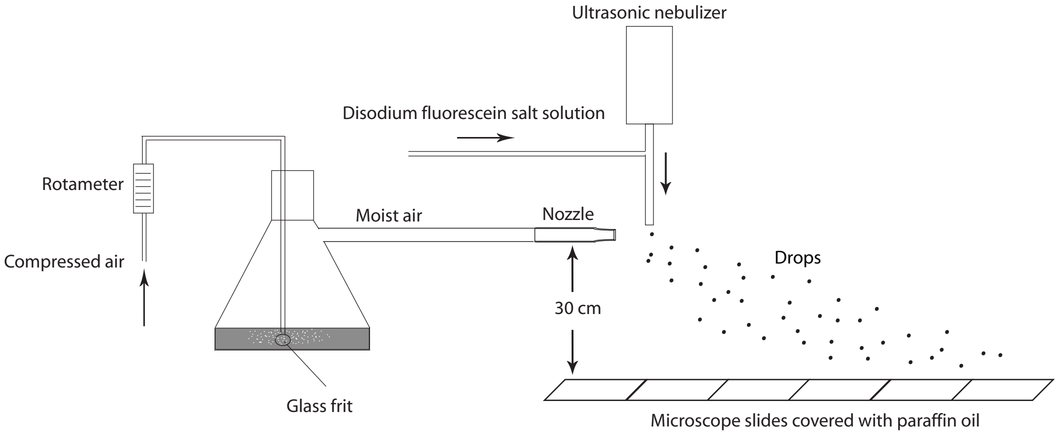

Figure 2.9: Apparatus used to measure the size distribution of drops generated by the nebulizer

2.1.5 The drop size distribution measurement system

The size distribution of the drops generated by the ultrasonic nebulizer was measured using a method similar to that used to measure the PSL particles but involving more processes. Because some drops from the ultrasonic nebulizer are large enough to deform and splash on the microscope slide a different measurement method was needed. So the method used here was to cover the slide with a layer of paraffin oil. The drops hitting this oil layer will float inside the oil, preserving the original drop shape. After that, the size distribution of these drops in the oil was obtained using the same microscope/camera setup used in obtaining the PSL distributions. The apparatus used to do this is shown in Fig. 2.9. To enhance the contrast between the drops and the oil, a green dye (disodium fluorescein salt) solution was used in the nebulizer to generate the drops. An air nozzle mounted near the tip of the nebulizer was used to spread the drops. Without this air flow, due to the high number density of the drops generated by the nebulizer, most drops would overlap with each other when they fell on the microscope slide. The average velocity of the air flow was 2 m/s, and it was monitored by a rotameter to make sure it remained constant during each experiment. To minimize the evaporation of the drops before they hit the oil, the air was first humidified by flowing it through a glass frit submerged in water. An array of microscope slides covered with paraffin oil were placed below the nebulizer, the length of this array was adjusted so that no drop could reach the last slide in the array, thereby ensuring that all drop sizes fell in the range of the microscope slide array. In each measurement, after the nebulizer reached a steady state, the microscope slide array was exposed to the spray for 5s. Then the drops collected on the slide were imaged using the microscope/camera setup. The number of drops recorded for each experiment ranged from 6,000 to 10,000.

A detailed description about how to process these images to obtain the droplet size distribution and the resulting droplet size distribution are presented in Section 2.3.3.

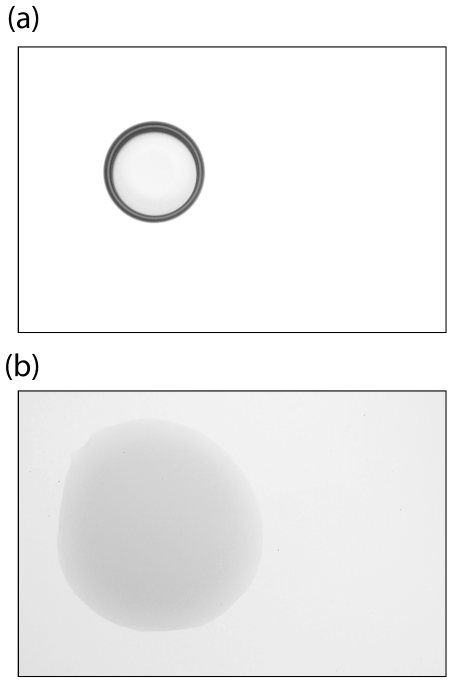

Figure 2.10: (a) Image of a drop floating in the paraffin oil layer. (b) Image of a drop that sank to the bottom of the paraffin oil layer.

There were two issues regarding the accuracy of using this method to measure the drop size distribution. The first issue was that as time passed, drops would eventually sink to the bottom of the oil layer, make contact with the solid surface of the slide, and spread on the surface. This issue was addressed by imaging these drops before they sank. As shown in Fig. 2.10, there is a significant difference between the drop that is floating and the drop that sank to the bottom of the oil layer. Fortunately, during the imaging process, it is not difficult to differentiate between these two kinds of drops and thereby ensure that the drops were imaged before they sank. The second issue was for some power levels on the nebulizer, not all the liquid delivered to the nebulizer was atomized into drops, a portion of the liquid was not atomized, this portion of the liquid formed a stream as shown in Fig. 2.11. The volume of this portion of the liquid was quantified by collecting it in a beaker as shown in Fig. 2.11, during this process, the beaker was placed such that it collected no drops. The details about how to address the influence of liquid that was not atomized on the particle scavenging are described in Section 2.4.

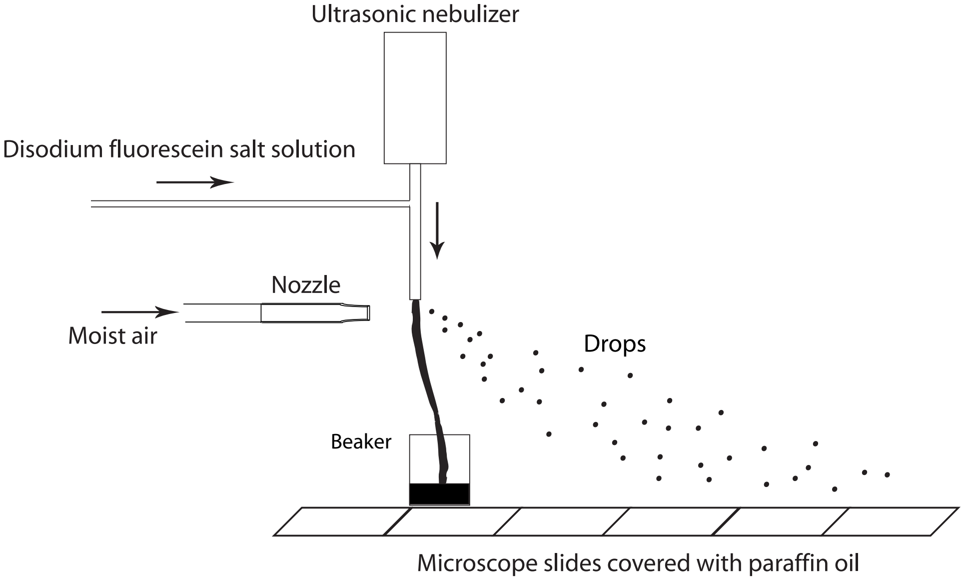

Figure 2.11: The method to quantify the volume of the liquid that is not atomized into drops.

2.2 Procedure

Before each experiment, clean air was used to flush the entire setup. The air flow used in these experiments was obtained from the building air compressor. Before entering the setup, it was dried to a relative humidity of $\sim 5\%$ and filtered by a high efficiency particle filter with a 0.3 μm cutoff size. After flushing the setup until both particle counters read zero, both the spray (ultrasonic nebulizer) and the aerosol generator (the TSI atomizer) were turned on. Initially distilled water without particles was fed to the aerosol generator to check whether all the water was removed during the particle atomizing process. Both particle counters were monitored for 5 minutes to ensure that they remained at zero, thereby ensuring that: first, all the water was removed during the atomizing process in the aerosol generator prior to the upstream particle counter; second, that droplets generated by the spray were also evaporating completely prior to the downstream particle counter. After that the spray and the aerosol generator were turned off. Then the distilled water in the aerosol generator was replaced by the diluted PSL hydrosol, and the generator was turned on again, and was allowed to run until both particle counters gave stable readings. Once this was achieved, particle data acquisition began.

During data acquisition, the ultrasonic wet scrubber was operated in two different modes, one after the other. One mode was the idle mode where the water spray in the ultrasonic wet scrubber was turned off. The difference between the particle number upstream and downstream of the ultrasonic wet scrubber in this mode was due solely to particle deposition in the pipelines. The second mode was the scavenging mode where the water spray was turned on. The difference between the upstream and downstream particle counts of the ultrasonic wet scrubber was due to the combined effect of particle deposition in the lines and particle scavenging by the spray drops. During each experiment, each mode was operated for 6 minutes in turn until the data storage buffer in the particle counters was full. Then the data was downloaded to a computer for further analysis. Detailed description of the data analysis is presented in the data processing section (Section 2.3.4). This procedure was performed several times for each run and was the same for experiments with or without the ultrasonic standing wave field.

2.3 Data processing

2.3.1 The size distribution of the PSL particles

As described in Section 2.1.4, images of PSL particles on the microscope slide were obtained by a combination of microscope (Leica DM750) and digital camera (Canon DS126291). Then, an image processing algorithm was used to obtain the particle diameters from these images. The initial step of the image processing was to convert the original color images taken by the camera into greyscale images. This was done by averaging the three color components (red, green, blue) of the original images into one component. These greyscale images were then converted into binary images by using Otsu's algorithm[49] which determines the optimum global threshold in a greyscale image that can be used to separate objects from the background. A sample greyscale image of deposited particles is presented in Fig. 2.12, and the binary version of this image obtained using the Otsu's algorithm[49] is presented in Fig. 2.13.

As shown in Fig. 2.13, the central region of the particle became "hollow" after the original greyscale image was converted into the binary form. This is because these regions are relatively light-colored, similar to the the background in the original greyscale image. This occurs for relatively large PSL particles. These "hollow" particles were filled using a hole-filling algorithm. The resulting

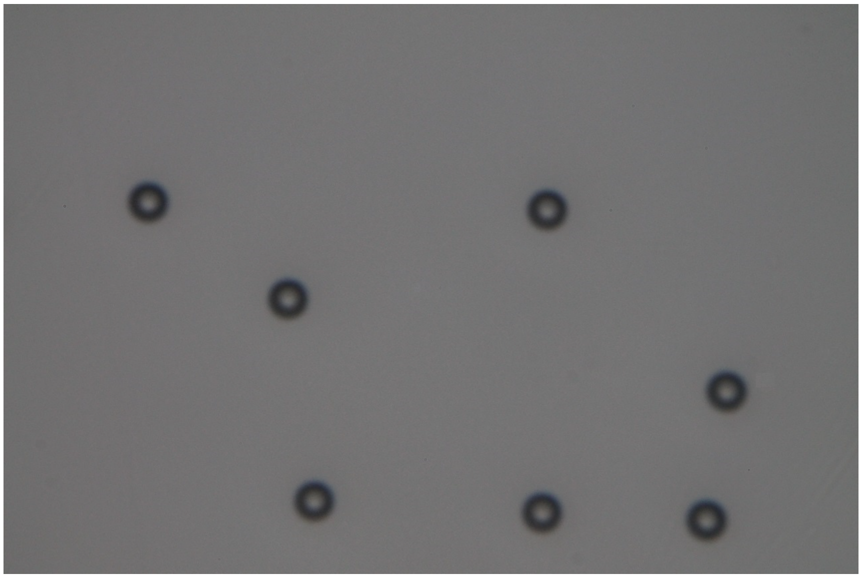

Figure 2.12: Sample greyscale image of PSL particles deposited on a microscope slide.

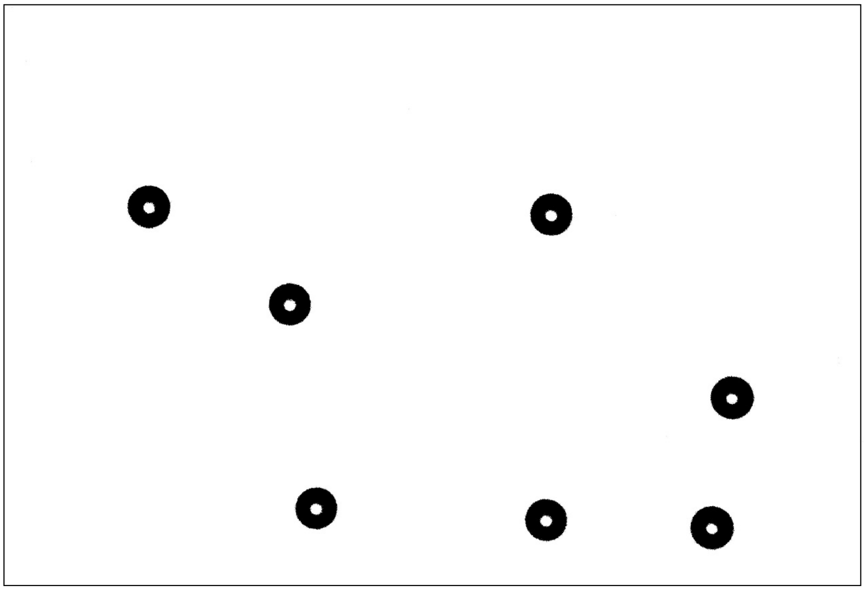

Figure 2.13: Binary version of the image presented in Fig. 2.12 obtained by applying Otsu's algorithm[49] to Fig. 2.12.

image is presented in Fig. 2.14

Each particle in the binary image was identified as an individual object based on the connectivity of the pixels. Connectivity defines groups of pixels having the same values and that are also connected in a binary image. A set of pixels in a binary image that form a connected group

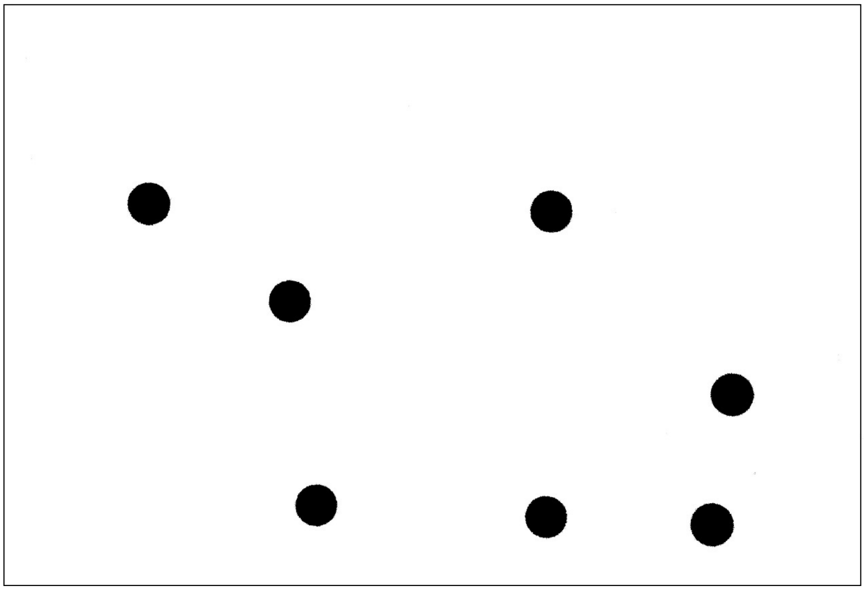

Figure 2.14: Filled version of the image presented in Fig. 2.13.

is identified as an object. The area of each particle as an identified object was then calculated by adding the areas of all of the pixels in that object. The area of each individual pixel was obtained by calibration as described in Section 2.1.4. This area was then converted to a diameter, assuming each particle was spherical. To ensure that only spherical objects were counted, a method to detect the roundness of the object was also used, so that impurities (which tend to be irregularly shaped), doublets, and triplets of PSL spheres were put in separate groups. This was done via a metric which quantifies roundness:

$$r = \frac{4\pi A}{C^2} \tag{2.3}$$

where A is the area of the object and C is the perimeter of the object. A value of r=1 is attained only for a perfect circle and is smaller or larger than one for any other shape. Because the PSL spheres were very uniform and round, images were considered to be PSL when $0.95 < r < 1.05$. After processing the images with this method, results showed the impurities and doublets or triplets of PSL spheres that were counted separately were rare. Typically only 0.2% of the imaged particles fell outside the range $0.95 < r < 1.05$.

The final result of the image processing algorithm was an array of particle diameters obtained from hundreds of particle images. The particle size distribution is defined as:

$$f_i = \frac{m_i}{M \Delta d_i} \tag{2.4}$$

where m_i is the number of particles in the i_{th} size bin, M is the total number of particles in all bins and Δd_i is the bin width of the i_{th} size bin which was set to 0.01 μm.

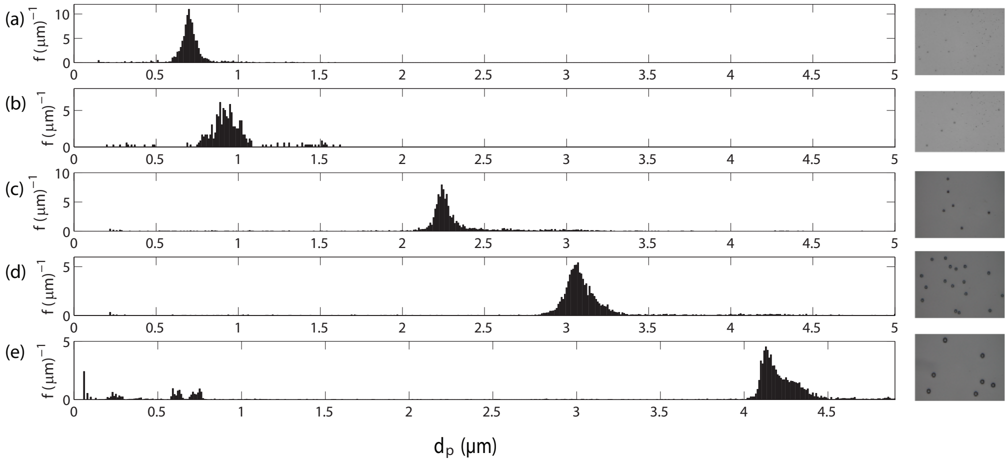

Figure 2.15: Particle size distributions for the five particle hydrosols used. (a) 0.7 ± 0.1 μm. (b) 0.9 ± 0.2 μm. (c) 2.3 ± 0.4 μm. (d) 3.1 ± 0.4 μm. (e) 4.2 ± 1.5 μm. A sample image obtained using the microscope is included to the right of each distribution.

Five sets of PSL particles having five different diameters were used in the experiments. According to the manufacturer, the average diameter for these were 0.7, 0.92, 1.7, 2.78, and 3.8 μm. The measured particle number size distributions are presented in Fig. 2.15 where f_i (Eq. (2.4)) is plotted against particle diameter d_p for each of the five sets of PSL particles used. The average diameters and standard deviations obtained from Fig. 2.15 are: 0.7 ± 0.1; 0.9 ± 0.2; 2.3 ± 0.4; 3.1 ± 0.4; 4.2 ± 1.5 μm. The rare impurities and doublets or triplets were excluded from these distributions because their number is insignificant (∼0.2%) compared to the rest of the distributions. The difference between the average diameter provided by the manufacturer and the value measured here is most likely due to inhomogeneities in the hydrosol containing particles. According to the manufacturer PSL particles will settle over time, especially those larger 1 μm. And the larger the particle, the faster it will settle. That means that in these suspensions, the larger particles tend to concentrate at the bottom of the container where the inlet to the atomizer is located. This could explain the slightly larger average diameter measured here, compared to the manufacturer's quoted value.

2.3.2 The size distribution of ambient air particles

As described in Section 2.1.4, instead of the microscope imaging system, the upstream particle counter was used to measure the size distribution of the ambient air particles. In these experiments, the upstream particle counter was used to sample the ambient air particles during the entire course of an experimental run with 5 seconds per data point. In each data point, in addition to the total particle number counts during the 5 seconds period, the particles counted were also binned by the particle counter into the six size bins described in Section 2.1.4. The final size distribution was obtained by first averaging all the data points obtained during the entire course of an experimental run for each size bin, then converting each averaged size bin into f_i using Eq. (2.4). The size distribution of ambient particles obtained using this method is presented in Fig. 2.16.

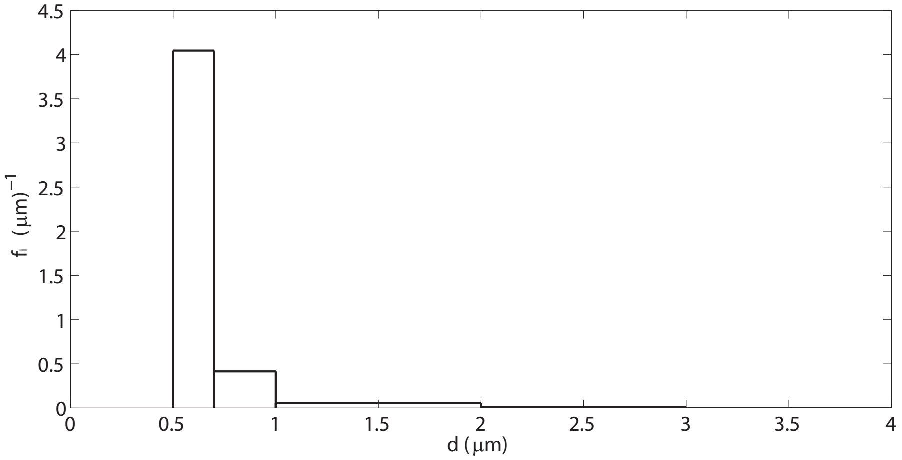

Figure 2.16: Particle size distribution for ambient air particles in the laboratory. The average particle diameter is 0.8 μm.

2.3.3 The size distribution of the spray drops

As described in Section 2.1.5, the size distribution of droplets generated by the nebulizer was measured using a method similar to that used to measure the PSL particles. Spray drops were collected on the microscope slides covered with a layer of paraffin oil. Then the microscope imaging system was used to take the images of these drops. The same image processing algorithm described in Section 2.3.1 was used to convert each of the acquired images to a binary image and then obtain the diameter of each of the drops in that binary image.

The size distributions of the spray drops were calculated using Eq. (2.4), the same as the PSL particles (the only difference is Δd_i was set to 6 μm for the drops). Figure 2.17 shows the size distributions of spray droplets, where f_i (Eq. (2.4)) is plotted against droplet diameter d_d for each of the five nebulizer power levels used to generate these droplets. For each power level, the average drop diameters $\bar{d_d}$ are 40, 71, 87, 97, and 56 μm.

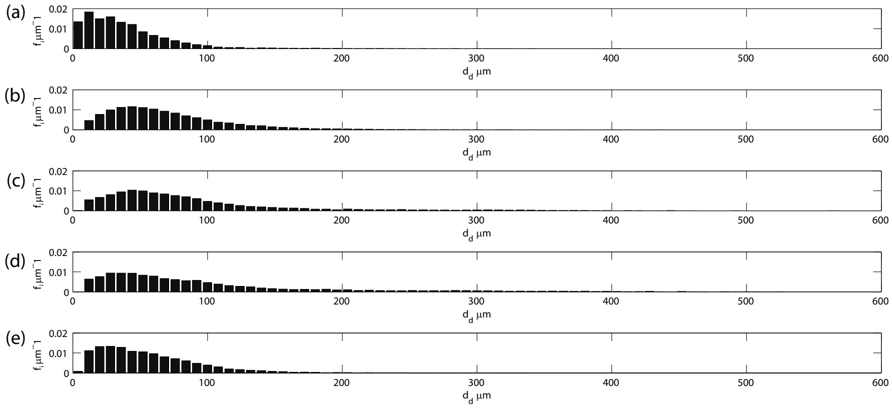

Figure 2.17: Droplets number size distributions for the different power levels on nebulizer. (a) Power level 1, $\bar{d_d} = 40$ μm. (b) Power level 2, $\bar{d_d} = 71$ μm. (c) Power level 3, $\bar{d_d} = 87$ μm. (d) Power level 4, $\bar{d_d} = 97$ μm. (e) Power level 5, $\bar{d_d} = 56$ μm.

2.3.4 Determination of E

A sample time trace is presented in Fig. 2.18 showing particle counts for the upstream particle counter (N_u) and the downstream particle counter (N_d). As shown in Fig. 2.18, N_d always lags N_u and the magnitude of N_d is always lower than the magnitude of N_u. As noted in Section 2.1.3, to ensure that calculation of E was not affected by the time lag between the readings of the particle counters, the data from the two particle counters were synchronized. This was done by shifting the time trace of the upstream particle counter with respect to the downstream particle counter by Δt. A range of Δt was considered, and the correlation coefficient R was computed for each Δt. The

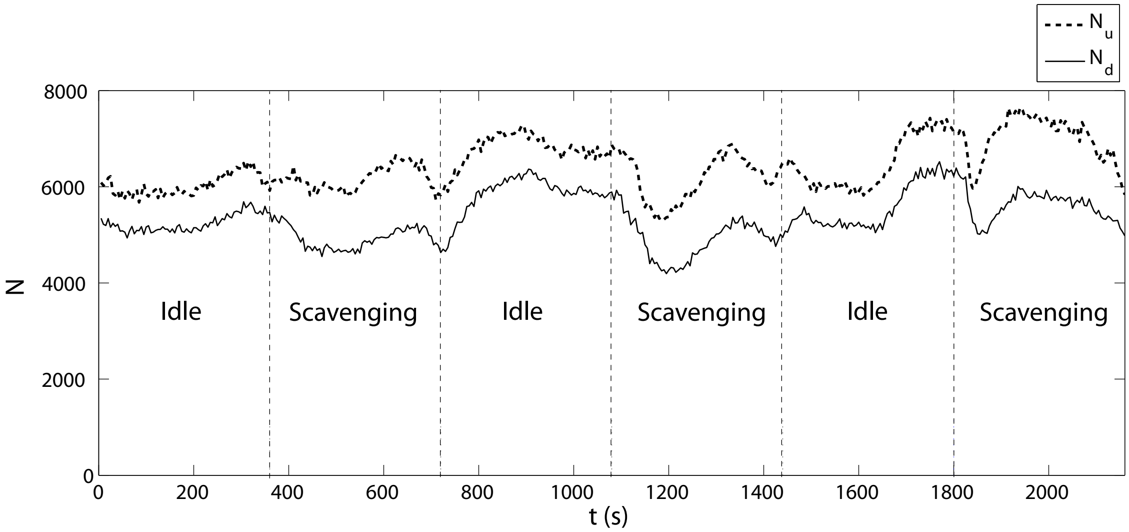

Figure 2.18: Particle count (N) time traces for the upstream (N_u) and downstream (N_d) particle counters, for a sample experiment. “Idle” and “Scavenging” represent the operational mode of the setup when the measurements were taken. The sampling period for each mode was 6 minutes.

value of Δt that maximized R was used. Here, R is defined as:

$$R = \frac{\sum\limits_{k=1}^{n} (N_{uk} - \bar{N_u})(N_{dk} - \bar{N_d})}{\sqrt{\sum\limits_{k=1}^{n} \left(N_{uk} - \bar{N_u}\right)^2} \sqrt{\sum\limits_{k=1}^{n} \left(N_{dk} - \bar{N_d}\right)^2}} \tag{2.5}$$

where n is the total number of data points in the time trace, N_{uk} is the k_{th} data point for the upstream particle counter, N_{dk} is the k_{th} data point for the downstream particle counter, $\bar{N_u}$ is the average for the upstream particle counter and $\bar{N_d}$ is the average for the downstream particle counter.

A plot of R versus Δt is presented in Fig. 2.19, showing that R reaches a maximum when Δt=5s. The optimized Δt is sensitive to the flow rate of the air and the configuration of the setup. Δt varied from 5s to 20s for different air flow rates explored in these experiments.

Once the data from the two particle counters were synchronized, the next step was to calculate E. As described in Section 2.2, the setup was operated in two modes: idle mode and scavenging mode. In the idle mode, the particle loss in the setup was only due to particle deposition on the pipe wall. In scavenging mode, because the spray was on, the particle loss was due to particle deposition plus particle scavenging by the spray. To determine E without errors due to particle

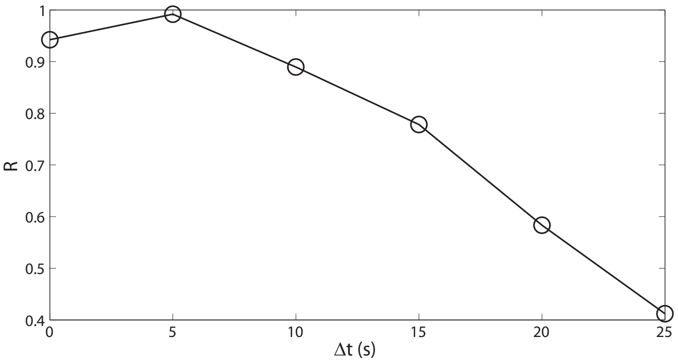

Figure 2.19: Correlation coefficient R versus shifting time Δt

deposition on the walls, the following procedure was followed.

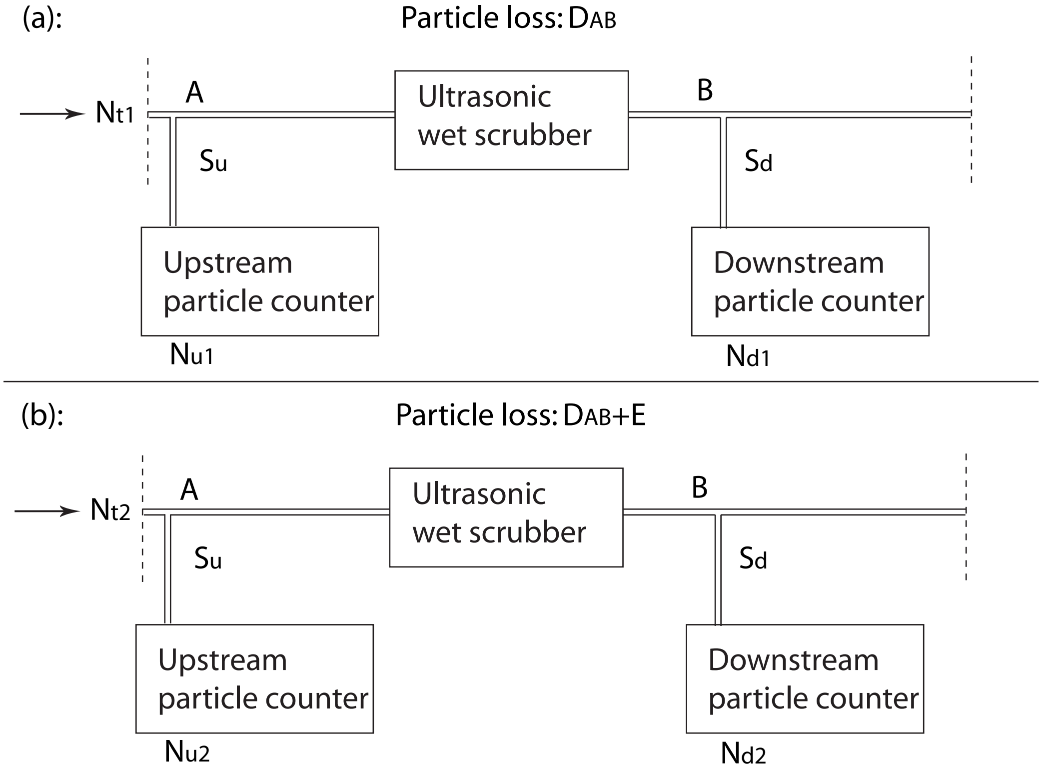

Figure 2.20: Simplified diagrams of a portion of the setup (the whole setup is shown in Fig. 2.1). (a) Setup in the idle mode. (b) Setup in the the scavenging mode.

Figure 2.20 shows a simplified diagram of a portion of the setup (the whole setup is shown in Fig. 2.1). Figure 2.20(a) shows the situation when the setup is in the idle mode, in which N_{t1} represents the total number of particles that entered this portion of the setup in a certain period of time; N_{u1} and N_{d1} are the number of particles counted by the upstream and downstream particle counters when N_{t1} particles were carried by the air flow through the setup; D_{AB} is the ratio between the number of particles deposited in the $A-B$ section of the setup and the total number of particles that entered the $A-B$ section, and S_u and S_d are the ratio between the number of particles sampled by the upstream and downstream particle counters respectively and the number of particles in the main flow (flow in the section $A-B$). Figure 2.20(b) shows the situation for the scavenging mode (water spray is on). In this mode, N_{t2} is the total number of particles that entered this portion of the setup in a certain period of time and N_{u2} and N_{d2} are used to replace N_{u1} and N_{d1} from Fig. 2.20(a). In the $A-B$ section of the setup, in addition to the particle loss due to the deposition (quantified by D_{AB}), there is also particle loss due to scavenging, E (Eq. (1.1)).

Using conservation of particles, quantitative relationships can be established between N_{u1}, N_{d1} and N_{t1}, which are shown in Eqs. (2.6) and (2.7).

$$N_{u1} = N_{t1} S_u \tag{2.6}$$

$$N_{d1} = N_{t1}(1 - S_u)(1 - D_{AB}) S_d \tag{2.7}$$

Similarly for the scavenging mode:

$$N_{u2} = N_{t2} S_u \tag{2.8}$$

$$N_{d2} = N_{t2}(1 - S_u)(1 - D_{AB})(1 - E) S_d \tag{2.9}$$

If S_u, S_d and D_{AB} are assumed to be the same in both modes, E can be extracted by combining Eqs. (2.6)-(2.9), giving:

$$E = 1 - \frac{N_{u1} N_{d2}}{N_{d1} N_{u2}} \tag{2.10}$$

This shows that E can be obtained knowing only the particle counts from the upstream and downstream counters (N_{u1}, N_{d1} and N_{u2} , N_{d2}); the unknown factors (N_{t1}, N_{t2}, D_{AB}, S_u and S_d) needn't be known since they cancel out. The prerequisite for this method to work is that S_u, S_d

and D_{AB} remain constant during the two operating modes of the setup. S_u and S_d can be regarded as constant because the sampling flow rate of the particle counters was maintained constant by their internal pumps, in addition to that the air flow rate in the setup was also maintained constant during the experiment. D_{AB} can be regarded as constant because the pipe configurations (length, diameter, bend angle, etc.) in $A - B$ section remained the same during the experiments.

During the experiments each particle counter recorded one measurement every 5s. Each operating mode (idle and scavenging) of the setup lasted for 6 minutes (see Section 2.2). During an operating mode, both the upstream and downstream particle counters would generate particle count time traces containing 72 measurements. When the setup was switched from one mode to the other some time was needed for the particle concentration to adjust to the new mode due to transients in the system. For the lowest gas flow rate in the experiment, the transit time for the setup was ∼25s, but to be conservative, the first 60s of data were discarded. Therefore, the first 12 measurements from each time trace were excluded from the calculation of E, giving 60 measurements in each time trace. The upstream particle counter's time trace was then shifted with respect to the downstream particle counter's time trace by Δt, which was determined using the method described at the beginning of this section. After time shifting, the two time traces were synchronized, and measurement pairs at any given time were considered simultaneous.

For the measurements recorded during the idle mode, each pair is a pair of N_{u1} and N_{d1}. For the measurements recorded during the scavenging mode, each pair is a pair of N_{u2} and N_{d2}. For a pair of measurements in the idle mode and a pair of measurements in the scavenging mode, E can be calculated using Eq. (2.10). So, the first pair of measurements acquired during each mode were combined to calculate a value for E, then the second pair were combined to calculate another value for E, and so on.

The scavenging coefficients reported in the results section (Section 2.4) are $\bar{E}$, averages of E calculated using the data taken during an experiment run. For each $\bar{E}$ of an experiment, the 95% confidence interval $u_{\bar{E}}$ was also calculated. The $u_{\bar{E}}$ is composed of two parts, random uncertainty P and averaged systematic uncertainty $\bar{B}$. If there is n values of E, then P is:

$$P = t_{(n-1,95)} \frac{S_E}{\sqrt{n}} \tag{2.11}$$

where $t_{(n-1,95)}$ is the t estimator of the uncertainty, $n-1$ is the degrees of freedom, and 95 represent

95% probability.[50] The actual value of $t_{(n-1,95)}$ can be found in Student-t Distribution table.[50] S_E is the standard deviations of the E.[50]

The systematic uncertainty of the particle counter has two sources: truncation uncertainty u_t and coincidence uncertainty u_c. As the resolution limit of the particle counter is one particle, for a particle data point with N particle counts, the truncation uncertainty is:

$$u_t = \frac{1}{N} \tag{2.12}$$

As noted in Section 2.1.3, the coincidence uncertainty u_c occurs when more than one particle happens to be in the sensing zone at one time. The higher the particle number density, the more likely a coincidence error will occur. One can estimate the coincidence uncertainty as:[51]

$$u_c = \frac{\frac{V}{4Q_sT}N^2}{1 - \frac{V}{2Q_sT}N} \tag{2.13}$$

where V is the volume of the sensing zone of the particle counter, Q_s is the sample flow rate of the particle counter and T is the sampling period of the particle counter. Using u_t and u_c as described above, the systematic uncertainty of the particle counter is:

$$B = \sqrt{\left(\frac{\partial E}{\partial N_{u1}}u\right)^2 + \left(\frac{\partial E}{\partial N_{u2}}u\right)^2 + \left(\frac{\partial E}{\partial N_{d1}}u\right)^2 + \left(\frac{\partial E}{\partial N_{d2}}u\right)^2} \tag{2.14}$$

where

$$u = \sqrt{{u_t}^2 + {u_c}^2} \tag{2.15}$$

The 95% confidence interval is:

$$u_{\bar{E}} = \sqrt{(t_{(n-1,95)}P)^2 + \bar{B}^2} \tag{2.16}$$

where $\bar{B}$ is the average of the individual systematic uncertainties for each $\bar{E}$.

2.4 Results

The average scavenging coefficient $\bar{E}$ of ambient air particles and PSL particles with $d_p = 0.9 \pm 0.2$ μm versus water flow rate Q_l are presented in Figs. 2.21 and 2.22, respectively. The size

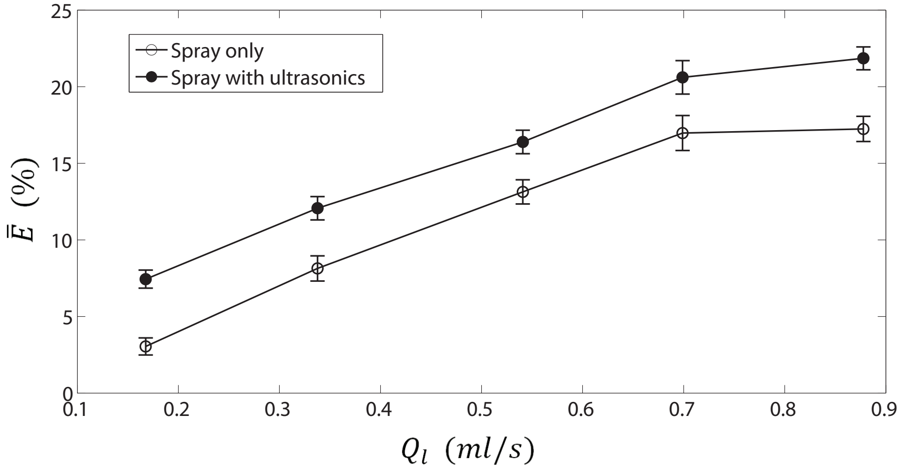

Figure 2.21: Average scavenging coefficient $\bar{E}$ versus water flow rate Q_l for ambient air particles. Open symbols represent runs without an ultrasonic standing wave field and filled symbols represent runs with an ultrasonic standing wave field.

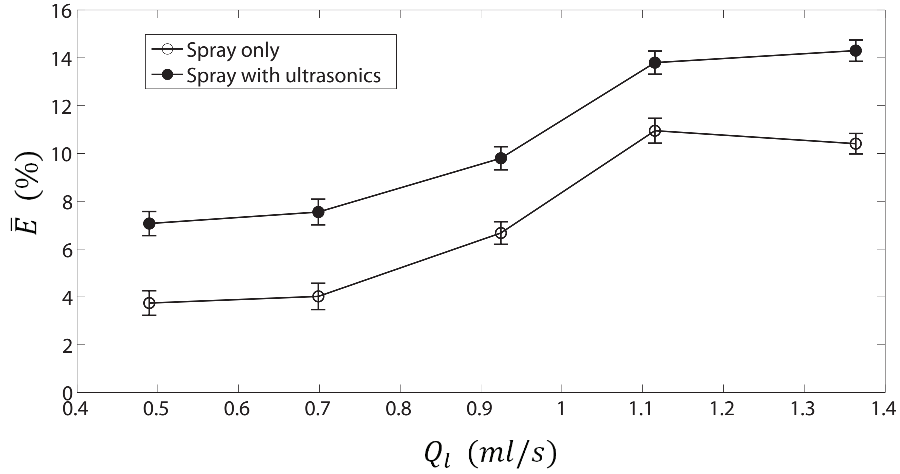

Figure 2.22: Average scavenging coefficient $\bar{E}$ versus water flow rate Q_l for PSL particles. Open symbols represent runs without an ultrasonic standing wave field and filled symbols represent runs with an ultrasonic standing wave field. (Additional data for this figure were obtained during the last period of this thesis research, these data are presented in Appendix A)

distribution of the ambient air particles is presented in Fig. 2.16. The air flow rate of the ultrasonic wet scrubber was fixed at Q_g=67 ml/s for the experiments presented in Figs. 2.21 and 2.22. The error-bars are 95% confidence intervals of $\bar{E}$ calculated using Eq. (2.16). For each liquid flow rate, $\bar{E}$ is presented with and without the ultrasonic standing wave. The results presented in Figs. 2.21 and 2.22 show that, first, there is an increase in the scavenging coefficient when the spray was combined with an ultrasonic standing wave field. Secondly, these figures show that the scavenging coefficient (both with and without an ultrasonic standing wave) increases with liquid flow rate.

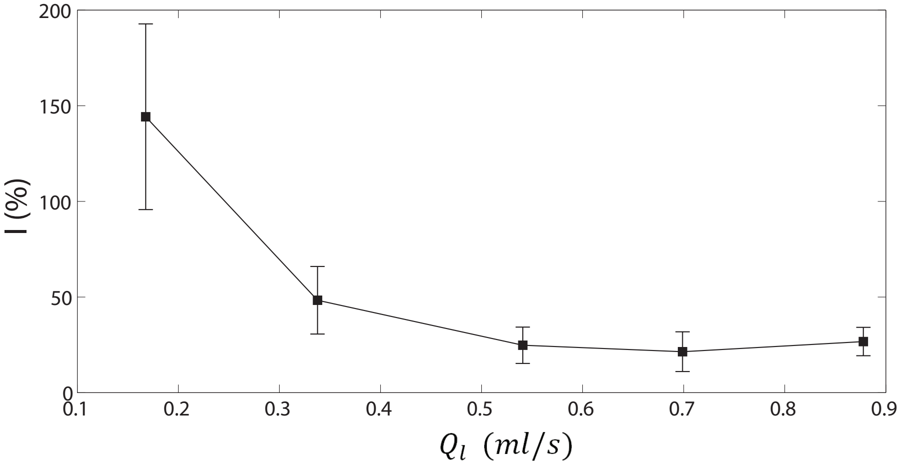

Figure 2.23: Percent improvement of scavenging coefficient I versus water flow rate Q_l for ambient air particles.

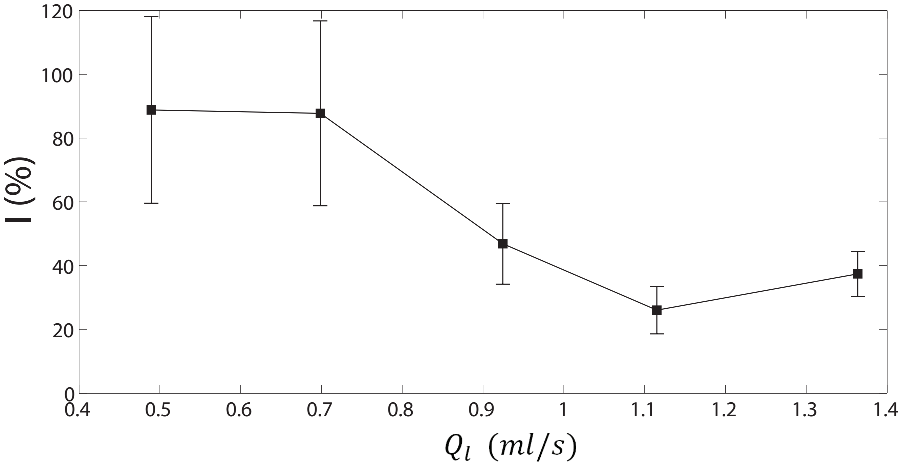

Figure 2.24: Percent improvement of scavenging coefficient I versus water flow rate Q_l for PSL particles. (Additional data for this figure were obtained during the last period of this thesis research, these data are presented in Appendix A)

The increase in the scavenging coefficient due to ultrasonics can be better revealed by the percent improvement in scavenging, I, which is defined as:

$$I = \frac{E_w - E_{wo}}{E_{wo}} \times 100\% \tag{2.17}$$

where E_w and E_{wo} are the scavenging coefficients with and without ultrasonics, respectively. Figures 2.23 and 2.24 show the percent improvement of scavenging coefficient I versus water flow rate Q_l for ambient air particles and PSL particles respectively. The error bars of I are calculated based on the theory of propagation of uncertainty[50] from 95% confidence intervals of E_w and E_{wo}. The percent improvement, I, presented in Figs 2.23 and 2.24, showing improvements is significant, reaching 140% for the ambient particles and 100% for the 0.9 μm PSL particles when the water flow rate is small.

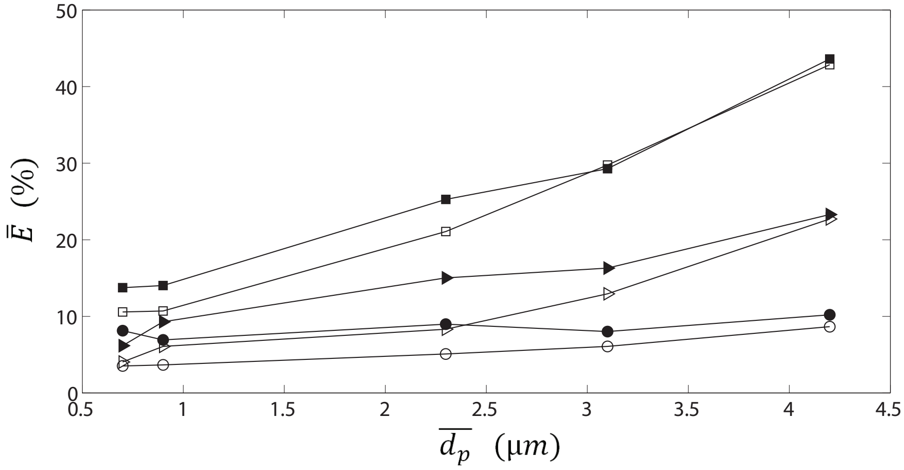

Figure 2.25: Plot of the average scavenging coefficient $\bar{E}$ versus average particle diameter $\bar{d_p}$ for experiments using PSL particles. Data is presented for three different water flow rates (○: $Q_l = 0.43$ ml/s; ▷: $Q_l = 0.87$ ml/s; □ : $Q_l = 1.23$ ml/s). Open symbols represent runs without an ultrasonic standing wave field, and filled symbols represent runs with an ultrasonic standing wave field.

Figure 2.25 is a plot of $\bar{E}$ versus average particle diameter $\bar{d_p}$ for PSL particles at three different spray flow rates. The air flow rate was fixed at Q_g=67 ml/s for these experiments. In the plot the size of the error-bars based on 95% confidence interval of $\bar{E}$ calculated form Eq. (2.16) are similar or smaller than the symbol size, so these error-bars are omitted in this plot. For each water flow rate and average particle diameter, $\bar{E}$ is presented with and without an ultrasonic standing wave. The percent improvement due to ultrasonics, I is presented in Fig. 2.26. The results presented in Figs. 2.25 and 2.26 show that first there is an improvement in the scavenging coefficient when spray was combined with ultrasonic standing wave field for nearly all the particles sizes and liquid flow rates, the improvement is especially significant when the water flow rate and particle diameter are small, and second, the scavenging coefficient (both with and without an ultrasonic standing wave)

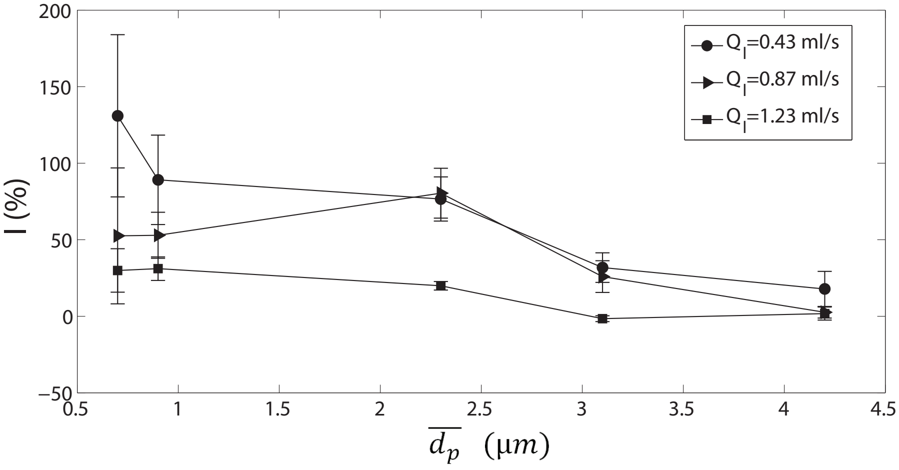

Figure 2.26: Plot of the percent improvement of scavenging coefficient I versus average particle diameter $\bar{d_p}$ for experiments using PSL particles. Data is presented for three different water flow rates (◯: $Q_l = 0.43$ ml/s; ▷: $Q_l = 0.87$ ml/s; □ : $Q_l = 1.23$ ml/s).

increases with average particle diameter and with water flow rate.

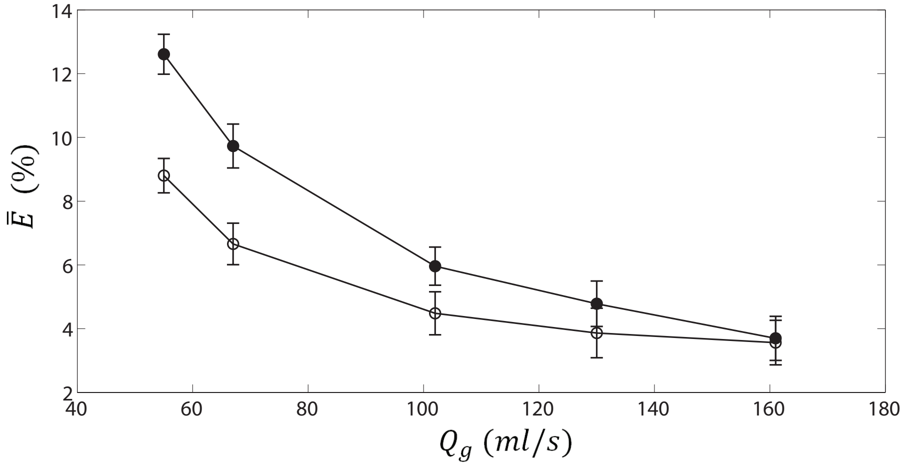

Figure 2.27: Plot of the average scavenging coefficient $\bar{E}$ versus air flow rate Q_g of the ultrasonic wet scrubber for PSL particles. Open symbols represent runs without an ultrasonic standing wave field, and filled symbols represent runs with an ultrasonic standing wave field. (Additional data for this figure were obtained during the last period of this thesis research, these data are presented in Appendix A)

Figure 2.27 is a plot of $\bar{E}$ versus air flow rate Q_g of the ultrasonic wet scrubber for PSL particles with $\bar{d_p}$=0.9 μm. The percent improvement due to ultrasonics, I corresponding to plot in Fig. 2.27 is presented in Fig. 2.28. Figs. 2.27 and 2.28 show that the increase in scavenging coefficient

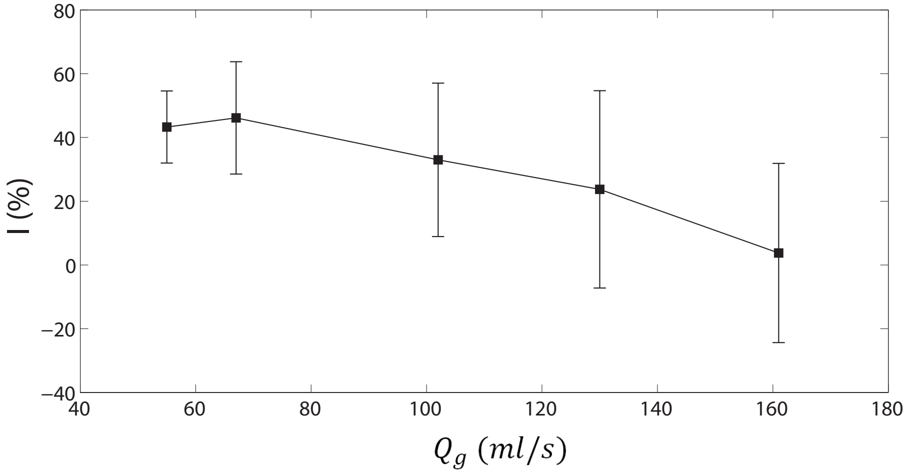

Figure 2.28: Plot of the percent improvement of scavenging coefficient I versus air flow rate Q_g of the ultrasonic wet scrubber for PSL particles. (Additional data for this figure were obtained during the last period of this thesis research, these data are presented in Appendix A)

due to the presence of an ultrasonic standing wave field diminishes as Q_g increases. Indeed there is no statistically significant effect of the ultrasonics when Q_g was greater than ∼120 ml/s in this setup. Figure 2.27 also shows that the scavenging coefficient (both with and without an ultrasonic standing wave) decreases with air flow rate.

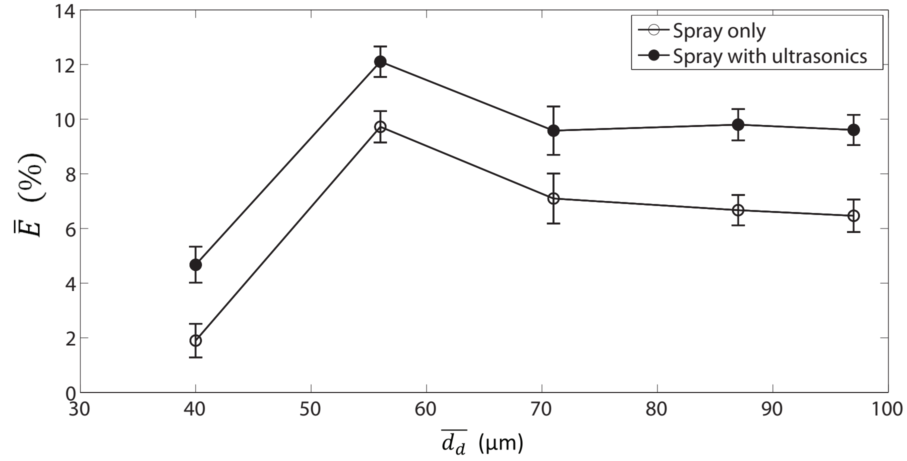

Figure 2.29: Plot of the average scavenging coefficient $\bar{E}$ versus average spray drop diameter $\bar{d_d}$ of the ultrasonic wet scrubber for PSL particles. Open symbols represent runs without an ultrasonic standing wave field, and filled symbols represent runs with an ultrasonic standing wave field.

Figure 2.29 is a plot of $\bar{E}$ versus average spray drop diameter $\bar{d_d}$. The air flow rate, Q_g, was

67 ml/s, water flow rate, Q_l, was 0.92 ml/s and particle size, $\bar{d}_p$, was 0.9 μm for these experiments. The results, presented in Fig. 2.29, show that $\bar{E}$ (both with and without an ultrasonic standing wave field) first increases with $\bar{d}_d$, reaching a maximum at $\bar{d}_d$=56 μm, then decreases with $\bar{d}_d$. This is counterintuitive, because for a fixed water flow rate, a higher $\bar{E}$ should correspond to smaller $\bar{d}_d$ as the drop number density will be much higher for a small $\bar{d}_d$ than a large $\bar{d}_d$. The reason for this counterintuitive behavior is probably because $\bar{d}_d$ does not incorporate the portion of the liquid that was not atomized. So $\bar{d}_d$ may not be the right parameter to plot versus $\bar{E}$. Below, a better parameter is developed.

The number of particles a drop scavenges is proportional to the volume the drop sweeps by as it moves through a volume of air laden with particles, and the volume the drop sweeps through is proportional to the cross-sectional area of the drop. The total volume a spray sweeps through is proportional to the total cross-sectional area of drops in that spray, so this total cross-sectional area of drops should be more closely related to $\bar{E}$. Here, the total cross-sectional area of drops generated by a unit volume of liquid for a given drop size distribution is defined as:

$$A_V = \frac{\sum_{i=1}^{\infty} m_i A_i}{V_T} \tag{2.18}$$

where m_i is the number of drops in the i_{th} size bin, A_i is the average cross-sectional area of drops in the i_{th} size bin and V_T is the total volume that passed through the nebulizer. V_T includes the portion of liquid that is not atomized (the stream shown in Fig. 2.11) and the portion of liquid that is atomized into drops. With Eq. (2.18), a single A_V was calculated for each drop size distribution that corresponds to each power level on nebulizer.

Figures 2.30 and 2.31 are plots of $\bar{E}$ and I versus A_V. The other parameters are the same as the plot shown in Fig. 2.29. The results presented in Fig. 2.30 show that $\bar{E}$ (both with and without an ultrasonic standing wave field) increases with A_V. Because Q_l is the same for these A_V, Q_l times A_V is the total cross-sectional area of the drops generated by the spray per unit time. So this means that for the drop diameters tested here, the scavenging coefficient is positively correlated to the total cross-sectional area of the drops generated by the spray per unit time. The results presented in Figs. 2.30 and 2.31 also show that there is an improvement of $\bar{E}$ when spray was combined with an ultrasonic standing wave field for all A_V tested here, I approaching 150% when A_V is small.

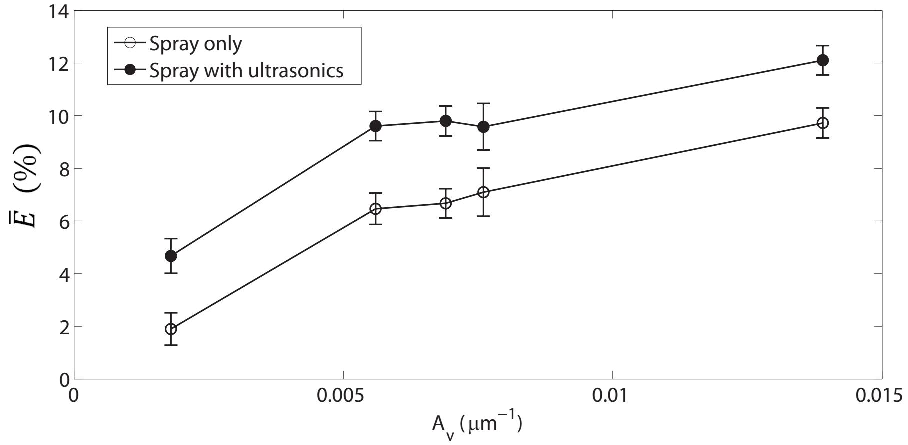

Figure 2.30: Plot of the average scavenging coefficient $\bar{E}$ versus A_V. Open symbols represent runs without an ultrasonic standing wave field, and filled symbols represent runs with an ultrasonic standing wave field.

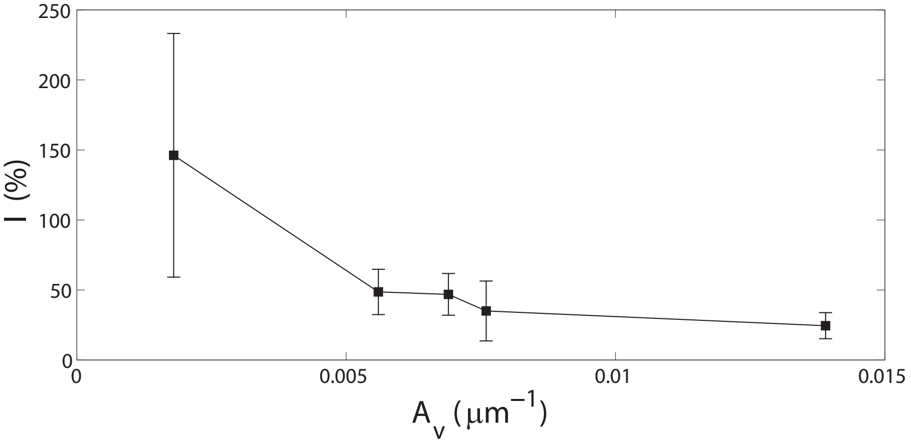

Figure 2.31: Plot of the percent improvement of scavenging coefficient I versus A_V.

Chapter 3

Sign of the Acoustic Radiation Force: Experiments and Results

In the introductory chapter, a review of existing theories showed that uncertainty in the current understanding of the acoustic radiation force $\mathcal{F}$ prevents a determination of whether this force will drive micron-scale particles to migrate to the pressure nodes or pressure anti-nodes of an ultrasonic standing wave field. As described in the Introduction, the following objectives need to be achieved to determine the exact location of these particles in an ultrasonic standing wave field: First, to verify whether the sign of $\mathcal{F}$ is a function of particle diameter. Second, if the sign of $\mathcal{F}$ is indeed a function of particle diameter, then obtain the critical diameter d_c at which the sign change of $\mathcal{F}$ occurs. In this chapter, the experiments used to achieve these objectives are described. Experiments were conducted using an ultrasonic standing wave field with a frequency around 30 kHz in air. Particles with diameters ranging from 0.2 μm to 4.5 μm were injected into the region of this ultrasonic standing wave field, and visual observation of where these particles accumulated was used to determine the sign of $\mathcal{F}$ (Both solid particles and fine water drops were used in the experiments, they are referred to collectively as "particles" unless noted otherwise in this chapter). The setup (Section 3.1), the procedure (Section 3.2) and the results (Section 3.3) of these experiments are presented in each section below.

3.1 Setup

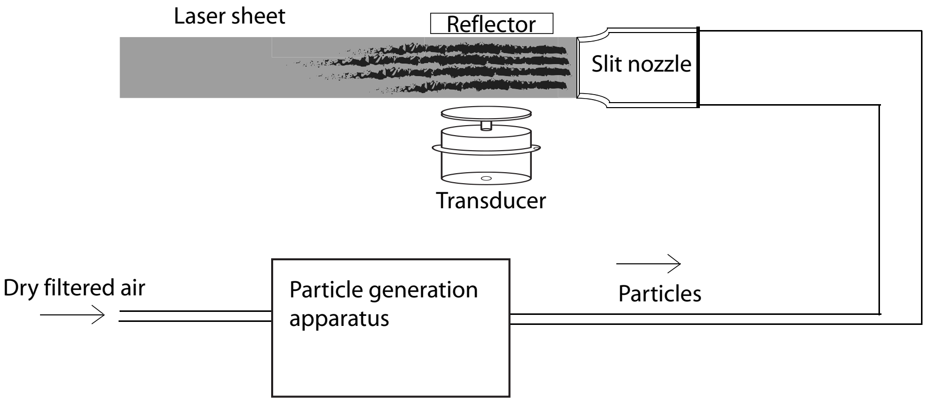

Figure 3.1: Overall view of experimental setup used to determine the location of particles with different diameters in an ultrasonic standing wave field.

The overall view of the experimental setup is shown in Fig. 3.1. The setup is composed of four parts: an ultrasonic transducer and reflector combination with a slit nozzle on its right side, an illumination and imaging apparatus (not shown in Fig. 3.1), a particle generation apparatus, and a particle size measurement apparatus (not shown in Fig. 3.1). The particles are generated, then introduced from the slit nozzle into an ultrasonic standing wave field generated by the transducer and reflector combination. After that, the patterns formed by these particles in the standing wave field were illuminated by a laser sheet, and the images of these patterns were captured by the imaging apparatus. Simple observation of these images enabled a determination of whether the particles were located in the nodes or anti-nodes. Finally, by measuring the diameters of these particles the critical diameter at which they move from the node to the anti-node was determined.

The ultrasonic transducer shown in Fig. 3.1 along with the associated amplifier and function generator are the same as described in Chapter 2. A slit nozzle with a length of 4 cm and a width of 0.4 cm was positioned on the right side of the transducer and reflector combination, as shown in Fig. 3.1. This nozzle was used to inject airborne particles into the standing wave field between the transducer and the reflector. The average flow velocity at the exit of the nozzle was on the order of 10 cm/s. The slit nozzle was oriented perpendicular to the transducer and reflector combination and the exit of the nozzle was also directed so that the resulting planar jet encompassed the axis going through the center of the transducer and reflector combination. This configuration was used for two reasons: First, the particles from the nozzle would flow through the region where the ultrasonic standing wave field is strongest and most uniform. Second, the direction of the flow from the nozzle would be perpendicular to the direction of the primary acoustic radiation force, so that the aerodynamic drag force on the particles would not interfere with the primary acoustic radiation force on the particles (the acoustic radiation force in the lateral direction is estimated to be orders of magnitude smaller than the primary acoustic force, so its effect was not considered here[52]).

The illumination apparatus consisted of a JDS Unlphase Model 1135 laser (633 nm, 20 mW) and a plano-convex cylindrical lens which was used to expand the beam into a laser sheet with a height slightly smaller than the distance between the transducer and the reflector. The laser sheet was directed into the standing wave field from the left side of the transducer and into the slit nozzle, as shown in Fig. 3.1.

Images were obtained using a digital camera (Canon, DS126311) oriented with its optical axis normal to the laser sheet and focused on the laser sheet. Example images of particles captured by this camera are shown in Fig. 3.2. Figure 3.2(a) shows that when the transducer is turned off, the particles from the nozzle spread uniformly in the region between the transducer and the reflector without any organized pattern. Figure 3.2(b) shows that when the transducer is on and was properly tuned to generate a standing wave field, the particles form stripe patterns in the nodes or anti-nodes of the standing wave field.

Three different types of particles were used in the experiments: polystyrene latex (PSL) microspheres, fine water drops and smoke particles. The PSL particles used here are identical to those used in Chapter 2, as is the aerosol generation and conditioning apparatus shown in Fig. 3.3. The apparatus used to generate fine water drops with variable diameters is illustrated in Fig. 3.4. The fine water drops were first generated by an ultrasonic fog generator. The frequency of the ultrasonic fog generator was $f \sim 2$ MHz. It was located more than 1 meter away from the ultrasonic transducer. There was a concern about whether the ultrasonic wave generated by the fog generator would interact with the ultrasonic standing wave field between the transducer and the reflector and affect the experiment results. However, the fog generator was submerged in water which has an acoustic impedance mismatch with air. The transmission coefficient of acoustic energy at the water/air boundary is on the order of 10^{-3}, as predicted by Kinsler *et al.*[53] Moreover, the attenuation coefficient at $f \sim 2$ MHz in air is on the order of 10^2 dB/m as predicted by Bass *et al.*,[54] which means that for a 1 m distance, the acoustic energy of the ultrasonic fog generator is attenuated by a factor of 10^{13}, eliminating any possible interference with the ultrasonic transducer.

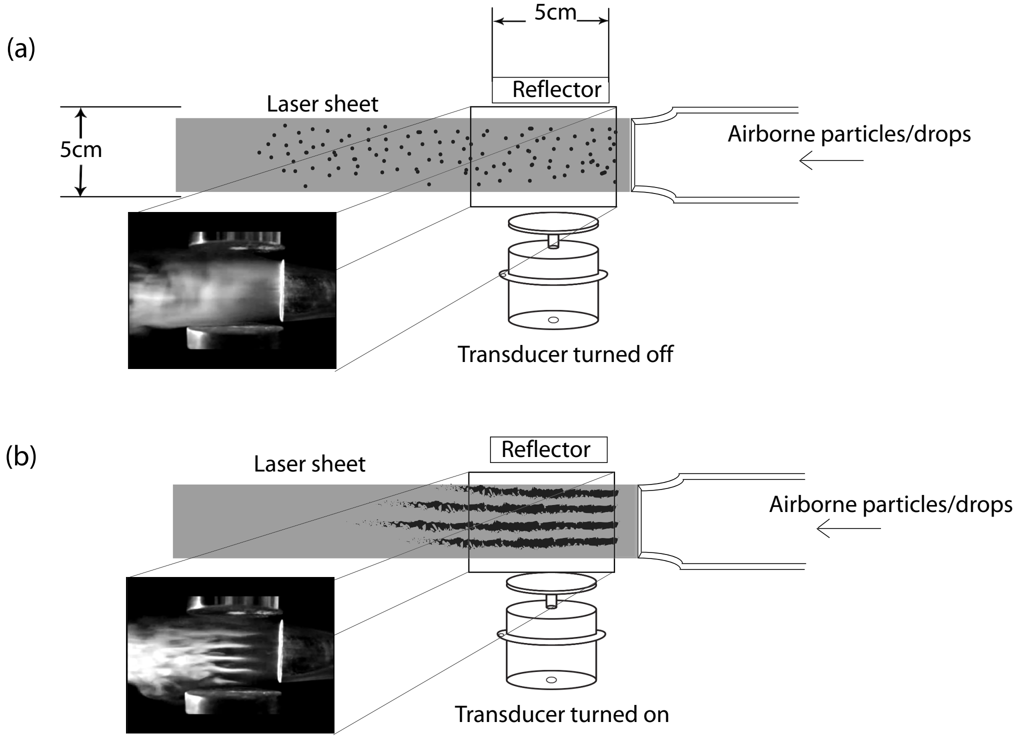

Figure 3.2: Particles in a standing wave field illuminated by a laser sheet. (a) Transducer turned off. (b) Transducer turned on.

In order to vary the drop diameter, the drops generated by the ultrasonic fog generator were first fed into a condensation loop consisted of a system of copper tubes as shown in Fig. 3.4. Moist air with a relative humidity of 90% was generated by flowing dry, filtered air through a glass frit submerged in water. This moist air was used to carry the drops through the condensation loop. By changing the temperature of the water bath in which the condensation loop was submerged, the amount of water that condensed on the drops was varied, thereby creating different drop diameters.

The apparatus used to generate smoke particles with variable diameters is illustrated in Fig. 3.5. As Fig. 3.5 shows, cigarette or incense was burned inside a sealed combustion chamber with a single inlet and outlet. Dry and filtered air was used to convect these smoke particles, with a broad size distribution, through a series of cigarette filters and two polycarbonate membrane prefilters to eliminate coarse particles (diameters bigger than 3 μm). The remaining particles were flowed through a test filter, before they entering the region of the ultrasonic standing wave field. To control the smoke particle diameter, experiments were run using test filters having a pore size of 0.2 μm, 0.4 μm, 0.6 μm, and 0.8 μm. Both the prefilters and the test filters were polycarbonate

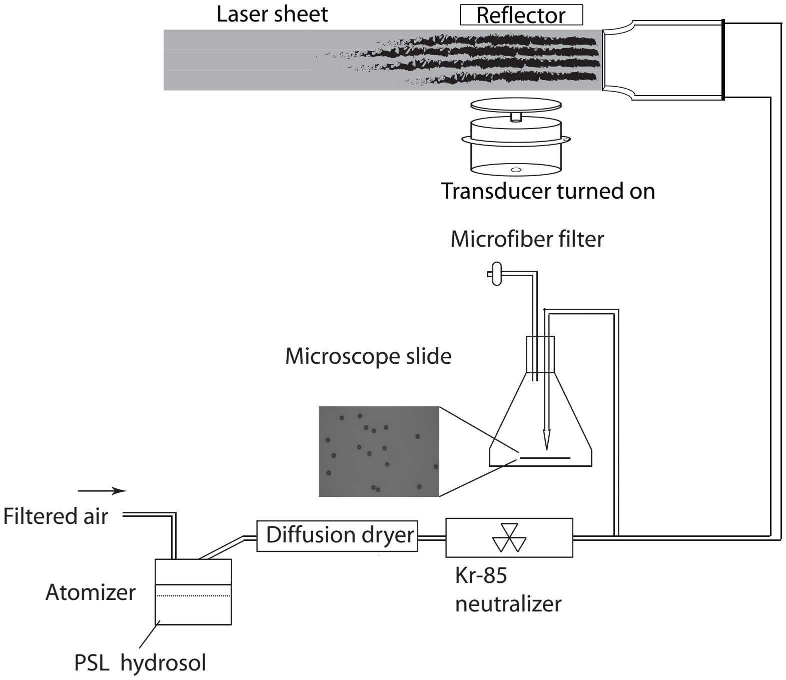

Figure 3.3: Apparatus used to disperse and test PSL particles.

membrane disc filters (Sterlitech). These filters are made for particulate analysis and are capable of capturing all particles larger than their precisely controlled pore diameter. With this configuration, the upper bound in the diameter of the smoke particles entering the standing wave field are controlled by the pore diameter.

The method used to measure the diameters of the PSL particles is exactly the same as the particle size distribution measurement apparatus used in the particle scavenging experiments described in Chapter 2. The diameters of the fine water drops were estimated using a method similar to that used to measure the PSL particles. First, the ultrasonic fog generator was used to atomize a solution containing a green dye (disodium fluorescein salt). The resulting drops were directed onto a glass microscope slide, leaving drop impact patterns with the color of the green dye. The same microscope and image processing algorithm used to obtain the diameters of the PSL particles were used to obtain the diameters of these impact patterns. The diameters obtained using each water bath temperature are presented in Section 3.3. The main concern of using this method to estimate the drop diameter is that the impact pattern diameter is not identical to the diameter of the drop that formed it. This is due to the fact that a drop will deform into a hemispherically shaped volume of liquid (a sessile drop) when it is in contact with the microscope slide. Widom[55] estimated the

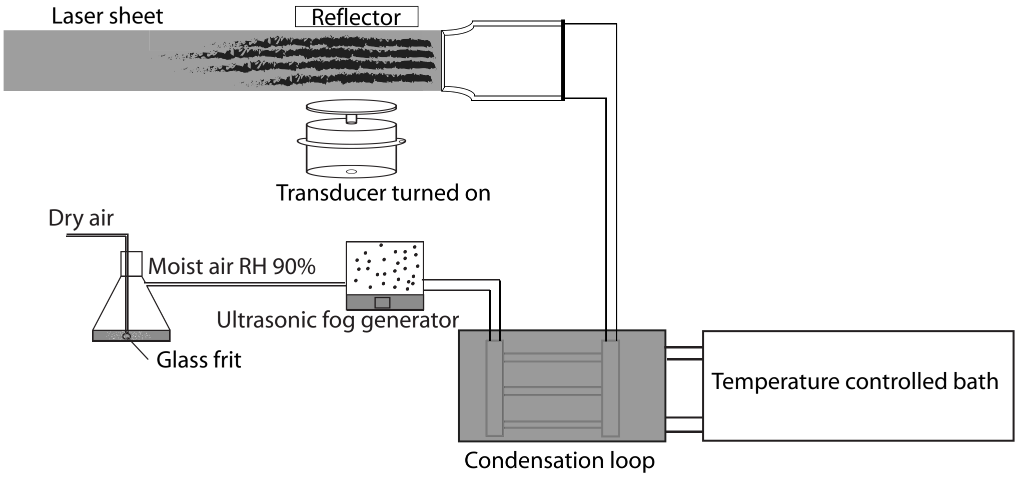

Figure 3.4: Apparatus used to generate and test fine water drops.

original drop diameter based on the diameter of the sessile drop using the equation:

$$d_d = d_s \left(\frac{(1 - \cos\theta)^2 (2 + \cos\theta)}{4 \sin\theta} \right)^{\frac{1}{3}} \tag{3.1}$$

where d_d is the diameter of the drop before impact, d_s is the diameter of the sessile drop and θ is the contact angle between the drop and the substrate. Of course Eq. (3.1) requires θ which is a complex function of the drop diameter, the drop impact velocity, the surface tension of the drop and the substrate, and the drop viscosity; this precluded it use here. But even without knowing the precise value of θ, due to the spread of the drop on the substrate surface, in most cases d_d should be smaller than d_s, and based on the form of Eq. (3.1), d_d should be a monotonic function of d_s, as will be shown below, this is sufficient for drawing the conclusions obtained here.

3.2 Experimental procedure

Before each experiment, the sinusoidal voltage applied to the transducer and the gap between the transducer and the reflector were tuned in order to establish a standing wave field. This process was similar to that described in Section 2.1.1 of Chapter 2. The frequency of the sinusoidal voltage applied to the transducer was tuned by attaching a piezoelectric sensor to the back of the transducer and monitoring its feedback on an oscilloscope. The frequency of the applied voltage was tuned until the amplitude of the feedback signal from the piezoelectric sensor reached a maximum,

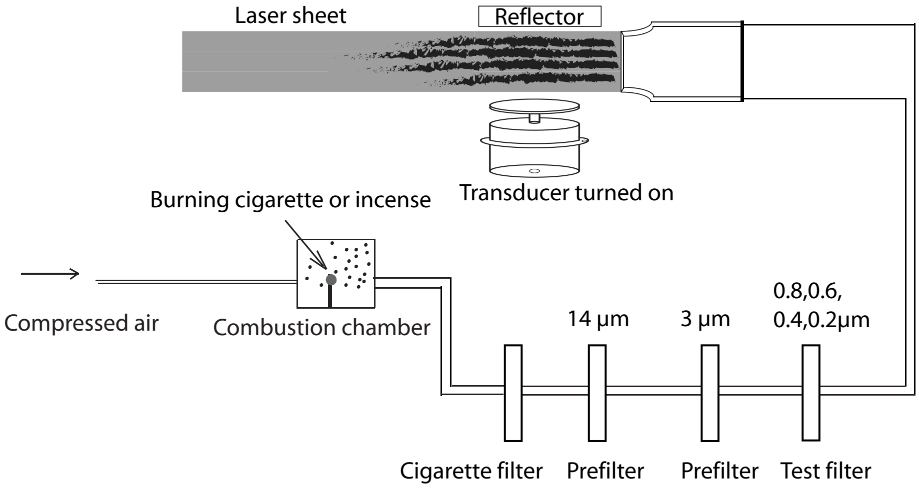

Figure 3.5: Apparatus used to generate and test smoke particles.

indicating that the transducer was vibrating at its resonance frequency. After that a water spray was introduced into the gap and the gap distance was tuned until the spray drops agglomerated into several millimeter sized water drops and levitated in the ultrasonic standing wave field between the gap. The ability of the ultrasonic standing wave field to levitate millimeter sized water drops, between the gap of the transducer and the reflector, indicated that a strong standing wave field had been established between the gap. The gap distance between the tip of the transducer and the reflector was 7 half wavelengths for the work presented below. Once the standing wave field had been established, the laser sheet was used to image the levitated drops. An example of such an image is shown in Fig. 3.6. The exposure time of the image was set to 30s to make sure only the time-averaged location of these drops were recorded.

For millimeter sized water drops in an ultrasonic standing wave field, the theories of Doinikov[43] and Settnes and Bruus[42] agree with each other; they predict that these drops would reside in the pressure nodes of the standing wave field. By imaging the location of these drops in the standing wave field, the location of the pressure nodes is recorded. Once the location of the pressure nodes are known, the location of the pressure anti-nodes is also known, since they are halfway between the pressure nodes. So, by injecting particles with different diameters into the same standing wave field and imaging their location, whether the acoustic radiation force drives them to the pressure nodes or the pressure anti-nodes can be determined.

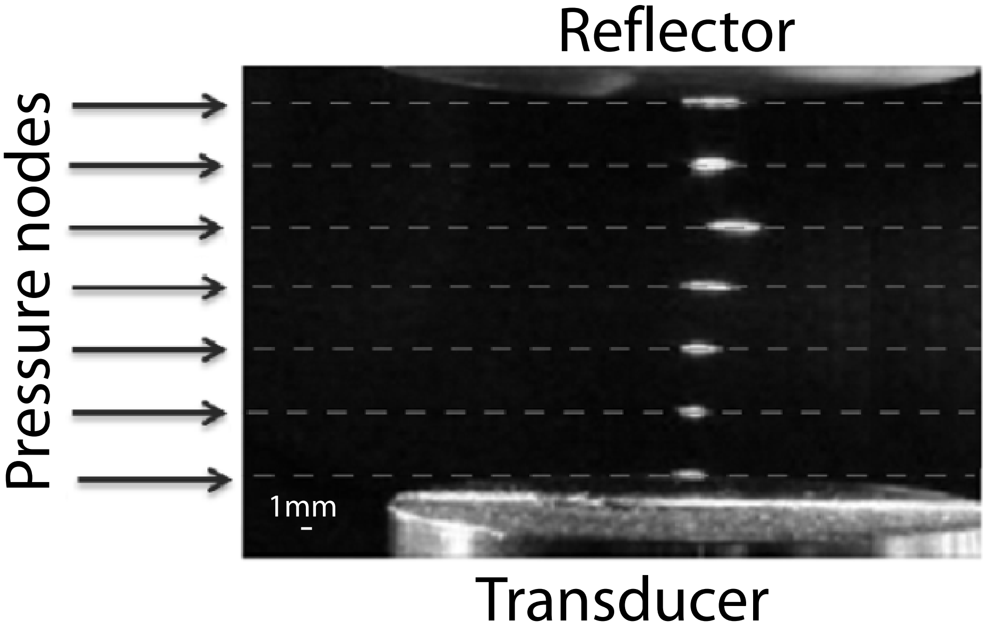

Figure 3.6: Location of the pressure nodes shown by millimeter scale water drops. These drops were formed by the agglomeration of spray drops that were introduced into the standing wave field. The blurring of these drops in the image is due to the long (30 seconds) exposure time.

The following procedure was used when working with fine water drops: First, the temperature controlled bath shown in Fig. 3.4 was turned on and set to 22 °C. Once the temperature in the condensation loop reached steady state, the ultrasonic fog generator and the air flow were turned on. Images of the locations of these drops in the standing wave field were then recorded. Then the standing wave field was turned off and a microscope slide was placed in front of the slit nozzle to collect the fine water drops, and the apparatus described in Section 3.1 was used to determine the drop diameter. After that, the temperature controlled bath was set to a lower temperature and the above procedures were repeated. Experiments were continued until the water bath temperature reached 1 °C.

For PSL particles, the following procedure was used. First, the atomizer shown in Fig. 3.3 was turned on. To ensure that the water drops generated during the PSL aerosol generation process evaporated completely prior to reaching the standing wave field, distilled water without PSL particles was first fed to the atomizer to generate only water drops. Then the imaging apparatus was used to acquire several images with 30s exposure time in the region of the standing wave field. These images were checked to ensure that nothing showed up in the standing wave field thereby ensuring complete evaporation of the drops. Then the distilled water in the atomizer was replaced by a diluted PSL hydrosol to generate the PSL aerosol. Images were then acquired of the patterns formed by these particles in the standing wave field with an exposure time of 30 s. Finally, the diameter of the PSL particles were measured using the apparatus described in Section 3.1. Once an experimental run was complete, the atomizer was cleaned and the above process was repeated. A total of six PSL diameters was explored.

For the smoke particles, a clean cigarette filter, a 14μm prefilter, a 3μm prefilter and a 0.8μm test filter were placed in series between the combustion chamber and the slit nozzle (see Fig. 3.5). An ignited cigarette or incense stick was inserted into the combustion chamber shown in Fig. 3.5, then the chamber was sealed. The flow of air was initiated, convecting smoke through the series of filters, and the imaging apparatus was used to acquire an image of the standing wave field region with an exposure time of 30 s. This process was then repeated for each test filter pore size until all four test filters were tested.

3.3 Results

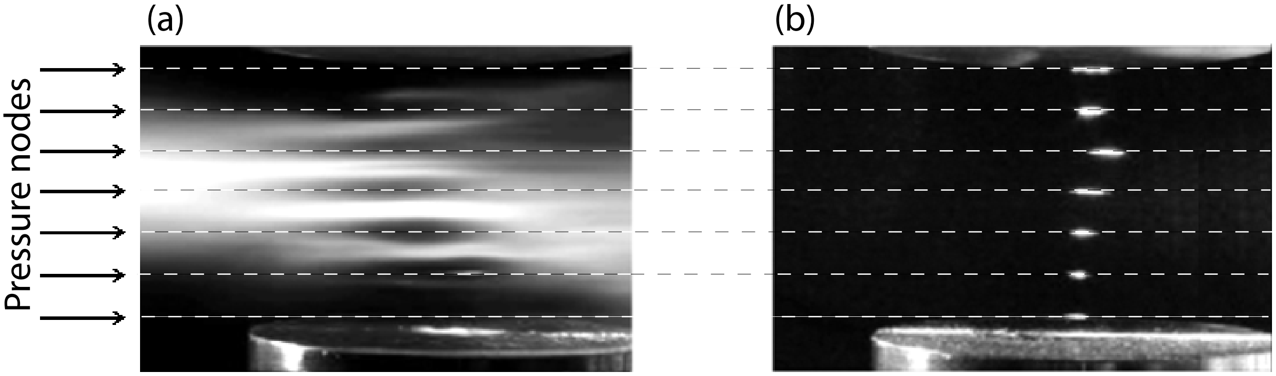

Figure 3.7: Locations of (a) micron scale and (b) millimeter scale water drops, in a standing wave field.

Figure 3.7 presents the images of water drops with very different diameters in a standing wave field. The drops presented in Fig. 3.7(a) are fine water drops without any condensation growth, therefore they are the smallest drops that could be generated by the setup shown in Fig. 3.4. The drops presented in Fig. 3.7(b) are millimeter scale water drops. It is clear that water drops with these two sizes do not migrate to the same locations in the standing wave field. The millimeter scale drops are located at the pressure nodes while the fine water drops are located at the pressure anti-nodes. Because the only difference between these two sets of drops was their diameter, this result shows that the sign of $\mathcal{F}$ is indeed dependent on the particle diameter. This result was one of the main objectives of this thesis research.

Table 3.1: Locations of fine water drops in a standing wave field as a function of the temperature of the water bath.

Water Bath Temperature	Location
10 °C – 22 °C	Pressure anti-nodes
3 °C – 9 °C	Ambiguous
< 2 °C	Pressure nodes

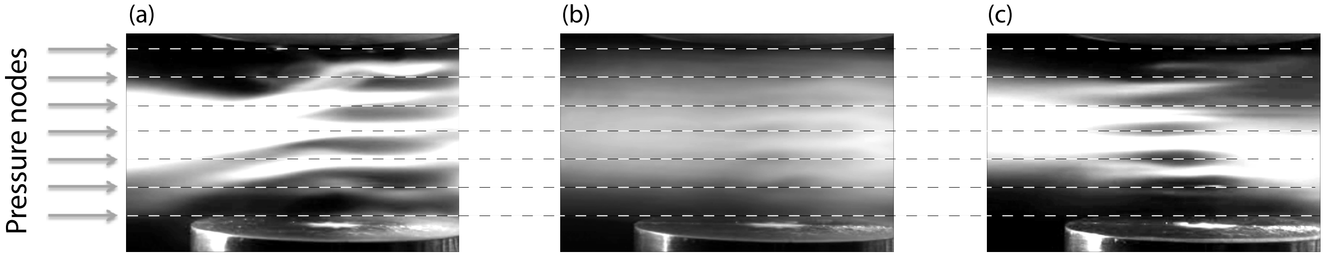

Figure 3.8: Locations of the fine water drops corresponding to different water bath temperatures in a standing wave field. (a). < 2 °C. (b). 3 °C – 9 °C. (c). 10 °C – 22 °C.

Knowing that $\mathcal{F}$ changes sign with diameter, the next step is to investigate at what critical diameter d_c the sign change for $\mathcal{F}$ occurs. The locations of the fine water drops in the standing wave field for the water bath temperatures investigated are presented in Table 3.1 and Fig. 3.8. As described in Section 3.1, lower water bath temperatures correspond to larger drop sizes. As shown in Table 3.1 and Fig. 3.8, for water bath temperatures < 2°C, the resulting fine water drops are located at the pressure nodes of the standing wave field (Fig. 3.8(a)). For water bath temperatures ranging from 10°C to 22°C, the location of the drops was in the pressure anti-nodes (Fig. 3.8(c)). For water bath temperatures in between (ranging from 3°C and 9°C), the resulting fine water drops were located in neither the nodes or the anti-nodes as seen in Figs. 3.8(b). These results suggest that for water bath temperature between 3 °C to 9 °C, the resulting drop diameters are close to d_c. The actual value of d_c can be obtained by converting these water bath temperatures into drop diameters. The diameters of these water drops were estimated based on the diameters of the patterns generated when these water drops impacted a microscope slide (Section 3.1).

Table 3.2: The average diameter of drop impact patterns as a function of the temperature of the water bath.

Water Bath Temperature (°C)	Average Diameter (μm)	95% Confidence Interval (μm)	Locations
$10 - 22$	2.722	0.007	Anti-nodes
$3 - 9$	3.060	0.009	Ambiguous
< 2	4.629	0.012	Nodes

These diameters are presented in Table 3.2 which shows that the transition from nodes to anti-nodes occurs when the average drop impact pattern diameter falls within the range 4.6μm to 3.1μm. However, as noted in Section 3.1, the drop impact pattern diameter d_s is an approximation of the actual drop diameter d_d and in most cases, due to the spread of the drop on the substrate surface, $d_s > d_d$. Thus the best that can be claimed based on the above results from fine water drops is that the upper bound of the d_c is 4.6 μm. For the conditions in these experiments, $\delta = 13$ μm, so the upper bound of the dimensionless critical diameter is $d_{c0} = 0.35$.

Another method for getting drop diameters is to use conservation of mass. In this way, water bath temperatures can be converted into drop diameters if the temperature and the relative humidity of the air entering and exiting the condensation loop, the air mass flow rate, and the drop number concentration in the condensation loop at each water bath temperature are known. The air mass flow rate and the air temperature and relative humidity are easy to obtain, however, there is no method to obtain the drop number concentration with the current setup preventing the use of this method.

Table 3.3: Locations of PSL particles in the standing wave field corresponding to different particle diameters.

Diameter	Position
4.5 ± 0.5 μm	Pressure nodes
4.2 ± 0.4 μm	Pressure nodes
2.8 ± 0.2 μm	Pressure nodes
1.7 ± 0.2 μm	Pressure nodes
1.3 ± 0.5 μm	Pressure nodes
0.9 ± 0.2 μm	Pressure nodes

The size distribution of PSL particles and the corresponding locations of these particles in the standing wave are presented in Fig. 3.9 and Table 3.3. These results show that all the PSL

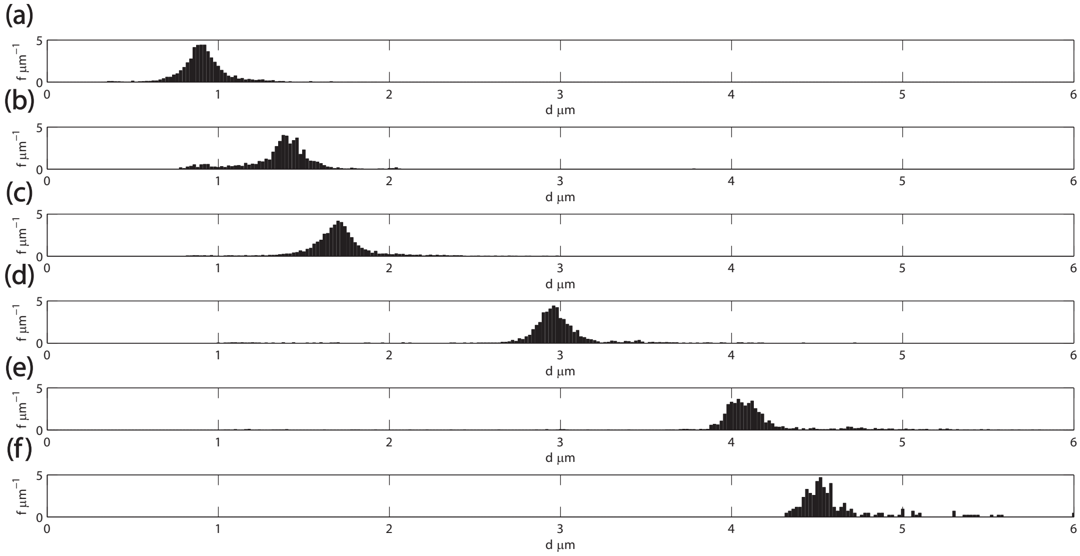

Figure 3.9: Particle size distributions for the six PSL particle solutions used. The average values plus/minus standard deviations were: (a) 0.9 ± 0.2 μm; (b) 1.3 ± 0.5 μm; (c) 1.7 ± 0.2 μm; (d) 2.8 ± 0.2 μm; (e) 4.2 ± 0.4 μm; (f) 4.5 ± 0.5 μm.

particles investigated here, whose diameters range from 0.9 μm to 4.5 μm, are located at the pressure nodes of the standing wave field. Because the smallest PSL particles ($d = 0.9$ μm) are located at the pressure nodes which is where particles larger than d_c are located, the best that can be claimed solely from these PSL particles is that the upper bound of d_c is 0.9 μm, and the upper bound of d_{c0} is $\frac{0.9\ \mu\text{m}}{13\ \mu\text{m}} = 0.07$. As noted earlier, d_{c0} obtained using water drops is 0.35. The reason for the discrepancy between results obtained from water and PSL particles is discussed in Chapter 4.

Table 3.4: Locations of smoke particles in the standing wave as a function of filter pore size. "None" means no particles where observed

Run #	Smoke type	d_f	Location	Indicate
Run 1	Cigarette smoke	0.8 μm	Pressure nodes	$d_c < 0.8$ μm
Run 2	Cigarette smoke	0.6 μm	Pressure nodes	$d_c < 0.6$ μm
Run 3	Cigarette smoke	0.4 μm	Pressure nodes	$d_c < 0.4$ μm
Run 4	Cigarette smoke	0.2 μm	None	0.2 μm$< d$
Run 5	Incense smoke	0.8 μm	Pressure anti-nodes	$d < d_c$, $d < 0.8$ μm
Run 6	Incense smoke	0.6 μm	Pressure anti-nodes	$d < d_c$, $d < 0.6$ μm
Run 7	Incense smoke	0.4 μm	Pressure anti-nodes	$d < d_c$, $d < 0.4$ μm
Run 8	Incense smoke	0.2 μm	None	0.2 μm$< d$

Table 3.4 presents the locations of the smoke particles in the standing wave field as a function

of the pore size of the test filter d_f and the smoke type use for each of the runs, as well as the upper bound or lower bound of d_c determined by each run. As noted in section 3.1, the burning of incense or cigarette forms a broad size distribution of particles, but only particles having $d < d_f$ can enter the standing wave field. Because the pressure nodes are where particles larger than d_c migrate, particles that go to the pressure nodes indicate $d > d_c$. Combining this information with $d < d_f$ enables the conclusion $d_c < d_f$. If these particles went to the pressure anti-nodes, because the pressure anti-nodes are where particles smaller than d_c are located, that would indicate $d_c > d$. If no particles are observed, that would indicate no particles passed the filter, so $d > d_f$.

With the above knowledge, the results from Table 3.4 are summarized. For cigarette smoke, Run 3 indicates that, $d_c < 0.4$ μm. For incense smoke, Run 7 indicates $d < d_c$ and Run 8 indicates that 0.2 μm$< d$, so 0.2 μm$< d_c$. If d_c for cigarette smoke and incense smoke are assumed to be the same, then it means that 0.2 μm$< d_c < 0.4$ μm. And for the conditions in these experiments, δ is 13 μm, so the non-dimensionalized critical particle diameter d_{c0} is between 0.015 and 0.03 for smoke particles.

It is possible that no particles were observed in Run 4 and Run 8 due to a simple inability to see particles of that size with the illumination and imaging setup. But even if that is true, the above conclusion is still valid. This is because Run 3 shows some particles went through 0.4 μm filter and were observed in the nodes, but these same particles were not seen in Run 4 when the filter size was reduced to 0.2 μm. Even if unobserved particles went through the 0.2 μm filter, this does not change the fact that particles having diameters smaller than 0.4 μm went to the pressure nodes and not to the pressure anti-nodes, which means $d_c < 0.4$ μm. This is same for the case of Run 7 and 8, which means $d_c > 0.2$ μm.

In summary, the results presented above clearly show that the sign of the dimensionless acoustic radiation force $\mathcal{F}$ does depend on particle diameter. These results also show that the dimensionless critical diameter at which the sign change for $\mathcal{F}$ occurs is different for different type of particles: $d_{c0} < 0.35$ for water drops, $d_{c0} < 0.07$ for PSL particles and $0.015 < d_{c0} < 0.031$ for smoke particles. The possible reasons for this discrepancy are discussed in Chapter 4.

Chapter 4

Discussion

In Chapter 2, an experimental study of an ultrasonic wet scrubber showed that compared to the use of a water spray alone, there is an increase in scavenging of micron-scale particles when a water spray is combined with an ultrasonic standing wave field. But the mechanism that causes this increase is not clear. In Chapter 3 the experimental results showed that the acoustic radiation force is bipolar, however, the dimensionless critical diameter d_{c0} at which the force changes direction obtained in the experiments does not agree with the predication made by Danilov and Mironov[44] presented in the introductory chapter. Below, explanations for both sets of results are presented.

4.1 Explanations for the increase in particle scavenging due to the standing wave field

There are several possible explanations for the increase in particle scavenging of a water spray in the presence of an ultrasonic standing wave field. One scenario is that the increased scavenging is due to drops entraining particles in their wakes, and bringing them to the pressure nodes where the drop number concentration is much higher than other locations in the ultrasonic wet scrubber, thereby increasing the chance for particles to combine with drops. Another scenario is that the increased scavenging is due to the acoustic radiation force driving both the drops and particles directly into the pressure nodes. For this scenario, the increase could be due to: (i) an increase in particles combining with each other in the pressure nodes, or (ii) an increase in particles combining with drops in the pressure nodes.

To determine which of these mechanisms causes the scavenging experimental results presented in Chapter 2, a simulation of the particles' and drops' trajectories is now presented. Combining the simulation results and the scavenging experimental results shows that the increased scavenging is caused by an increase in particles combining with drops in the pressure nodes due to the acoustic radiation force driving both drops and particles directly into the pressure nodes. The details are presented below.

4.2 Simulation of particle and drop trajectories in the standing wave field

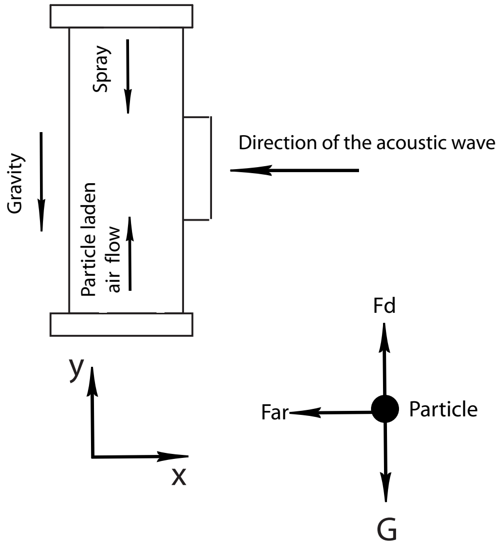

Figure 4.1: Direction of the forces on a particle in the scavenging chamber

In the scavenging chamber, there are three forces that act on a particle (PSL particle(s) and spray drop(s) are referred to collectively as "particle(s)" in this section unless noted otherwise). These are the acoustic radiation force, the aerodynamic drag force and the gravitational force. Figure 4.1 shows a single cross-section of the scavenging chamber and the direction of these forces relative to this cross-section. Here, the x-direction is parallel to the direction of the acoustic wave and perpendicular to the air velocity and gravity. The y-direction is perpendicular to the direction of the acoustic wave and parallel to the air velocity direction and gravity. This cross-section runs through the central axis of the cylindrical standing wave field. The analysis and the simulations conducted here are focused in this cross-section. The reason for choosing this cross-section is because compared to other cross-sections, particles have the longest residence time in the standing wave field in this cross-section. Therefore the ultrasonics is likely to be most effective in improving the particle scavenging in this cross-section. As shown in Fig. 4.1, the primary acoustic radiation force F_{ar} is in the x-direction, the aerodynamic drag force F_d is in the y-direction, and the gravitational force G is also in the y-direction.

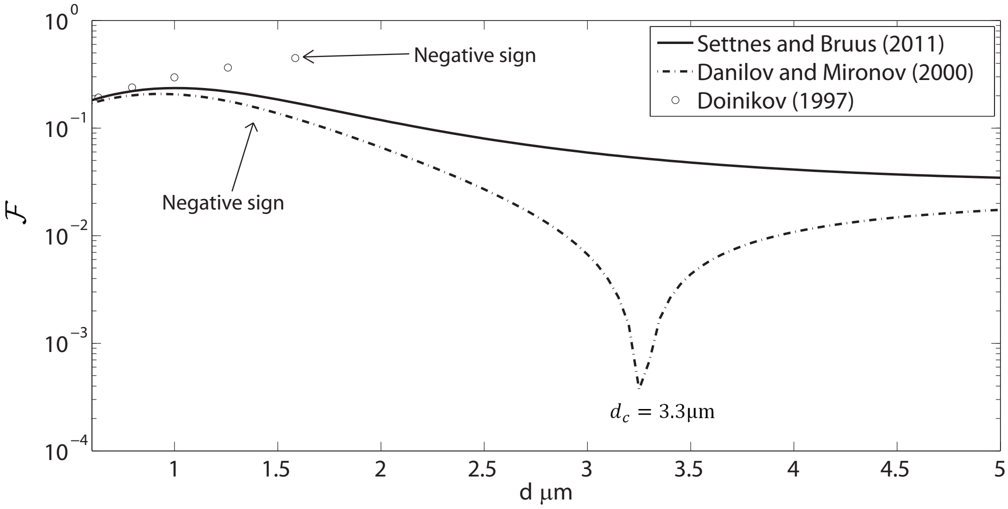

Figure 4.2: Dimensionless acoustic radiation force $\mathcal{F}$ on a PSL particle in a standing wave field predicted by the theories of Doinikov,[43] Danilov & Mironov[44] and Settnes & Bruus.[42] Arrows indicate regions where the sign of the $\mathcal{F}$ are different and d_c is the critical particle diameter where the sign of the force may flip. The frequency is $f = 30$ kHz (that used in the scavenging experiments). The critical diameter at which $\mathcal{F}$ changes sign in the theory of Danilov and Mironov[44] is $d_c = 3.3$ μm.

For the primary acoustic radiation force, the theory of Settnes and Bruus[42] is used here to calculate it. The reason for choosing this theory among others is: experimental results presented in Chapter 3 show that the PSL particles used in the scavenging experiments (diameter ranges from 0.9 μm to 4.5 μm) would migrate toward the pressure nodes under the influence of the acoustic radiation force, which means F_{ar} is unipolar for the particles in this size range. Figure 4.2 is a plot of the dimensionless acoustic radiation force $\mathcal{F}$ versus diameter of the PSL particle for the theories of Doinikov,[43] Danilov & Mironov[44] and Settnes & Bruus.[42] This plot indicates that regarding the sign of $\mathcal{F}$, only the theory of Settnes & Bruus[42] fits experimental results for the PSL particles with diameters range between 0.9 μm to 4.5 μm. As indicated above, 0.9 μm to 4.5 μm also lies in the diameter range of the PSL particles used in the scavenging experiments, so the theory of Settnes & Bruus[42] is selected among the other theories to conduct the force analysis as well as the simulations. Settnes and Bruus[42] predicts F_{ar} generated by a standing wave field as:

$$F_{ar} = F_{max} sin\left(2kx\right) \tag{4.1}$$

$$F_{max} = \frac{1}{2}\pi\Phi\left(\frac{\kappa_p}{\kappa}, \frac{\rho_p}{\rho}, \frac{2\delta}{d}\right) kE_{ac}d^3 \tag{4.2}$$

$$\Phi\left(\frac{\kappa_p}{\kappa}, \frac{\rho_p}{\rho}, \frac{2\delta}{d}\right) = \frac{1}{3}f_1\left(\frac{\kappa_p}{\kappa}\right) + \frac{1}{2}f_2\left(\frac{\rho_p}{\rho}, \frac{2\delta}{d}\right) \tag{4.3}$$

$$f_1\left(\frac{\kappa_p}{\kappa}\right) = 1 - \frac{\kappa_p}{\kappa} \tag{4.4}$$

$$f_2\left(\frac{\rho_p}{\rho}, \frac{2\delta}{d}\right) = \Re\left[\frac{2\left[1-\gamma\left(\frac{2\delta}{d}\right)\right]\left(\frac{\rho_p}{\rho}-1\right)}{2\frac{\rho_p}{\rho}+1-3\gamma\left(\frac{2\delta}{d}\right)}\right] \tag{4.5}$$

$$\gamma\left(\frac{2\delta}{d}\right) = -\frac{3}{2}\left[1+i\left(1+\frac{2\delta}{d}\right)\right]\frac{2\delta}{d} \tag{4.6}$$

where E_{ac} is the acoustic energy density, d is the diameter of the particle, $k = 2\pi/\lambda$, where λ is the wavelength, ρ is the density of the air, ρ_p is the density of the particle, κ_p is the compressibility of the particle, κ is the compressibility of the air, and δ is the thickness of the acoustic boundary layer (Eq. (1.2)). To obtain numerical values for F_{ar}, the values for all the variables in Eq. (4.2) are needed. All of these variables are easily obtained excepted for E_{ac}, which is difficult to measure. A force balance method was used to estimate the E_{ac} here. First, a voltage was added on the ultrasonic transducer equal to the voltage used in the scavenging experiments. Then it was tuned to levitate a water drop in the standing wave field. The diameter of the levitated water drop was measured via a camera with a known pixels/mm calibration. After that, the voltage applied to the transducer was slowly decreased until the drop fell. Then the weight of the drop was set equal to F_{max} in Eq. (4.2). Finally, E_{ac} was solved using Eqs. (4.2)-(4.6) using properties for water. Settnes & Bruus's theory[42] only predicts the primary acoustic radiation force (in the x-direction). The secondary acoustic radiation force (in the y-direction) is estimated to be orders of magnitude smaller than the primary radiation force,[52] and is not considered here.

For the aerodynamic drag force, F_d, if the flow around the particle for conditions in the scavenging chamber is assumed to be Stokes flow, then the aerodynamic drag force acting on the particle is:

$$F_d = 3\pi\nu\rho U d \tag{4.7}$$

where ν is the air kinematic viscosity, ρ is the air density, d is the diameter of the particle, and U is the relative velocity between the particle and the surrounding air. The aerodynamic drag force on the particle in the x-direction is ignored since the main air velocity is in the y-direction. In order to check whether the Stokes' flow assumption is suitable for the flow condition investigated here, the maximum steady-state relative velocity between the particle and the air flow in the scavenging chamber is estimated. This maximum steady-state relative velocity is achieved when the driving acoustic radiation force or gravitational force, depending on the direction being considered, is equal to the drag force. By equating the driving force to the drag force in each direction, gives:

$$U_x = \frac{F_{ar}}{3\pi\nu\rho d} \tag{4.8}$$

$$U_y = -\frac{mg}{3\pi\nu\rho d} \tag{4.9}$$

where U_x and U_y are the maximum relative velocities between the particle and the air flow in the x and y directions. The magnitudes of U_x and U_y for typical conditions in the scavenging experiments are presented in Table 4.1 where the diameter of the PSL particle is ~ 1 μm and the diameter of the water spray drop is ~ 100 μm. Because the analysis here is only an estimate of the maximum velocities, for the sake of simplicity, the spatial variation of F_{ar} is not considered, and F_{ar} is assumed to be equal to F_{max} (see Eqs. (4.1) and (4.2)). The spatial variation of F_{ar} is considered during the simulation of particle trajectories. Based on the maximum velocities presented in Table 4.1, the Reynolds number Re for the PSL particles and the spray drops are on the order of 10^{-3} and 1 respectively, so Stokes flow is a reasonable approximation for flow around the particle and the drop in the scavenging chamber.

One of the possible mechanisms that causes the increased scavenging (noted in Section 4.1),

Table 4.1: Magnitude of maximum velocities of a PSL particle and a spray drop

Direction	PSL particle	Water spray drop
x	10^{-3} (m/s)	10^{-1} (m/s)
y	10^{-2} (m/s)	10^{-1} (m/s)

drops entraining particles in their wakes, can now be excluded. This is because experimental[56] and simulation[57] results in the literature shows that the wake behind a drop does not appear until $Re > 20$. So the remaining mechanisms that could cause the increased scavenging are: particles combining with each other in the pressure node or particles combining with drops in the pressure node. A simulation of the detailed trajectories of PSL particles and spray drops is presented below to determine which mechanism is responsible for the increased scavenging.

The domain dimensions and the origin of the $x - y$ coordinate system of the simulation are shown in Fig. 4.3. The domain is a rectangular shaped area (shaded area in Fig. 4.3) with dimensions of 31 mm × 153 mm in the cross-section of the scavenging chamber mentioned above (see Fig. 4.1). The hatched area in the domain represents the area occupied by the standing wave field.

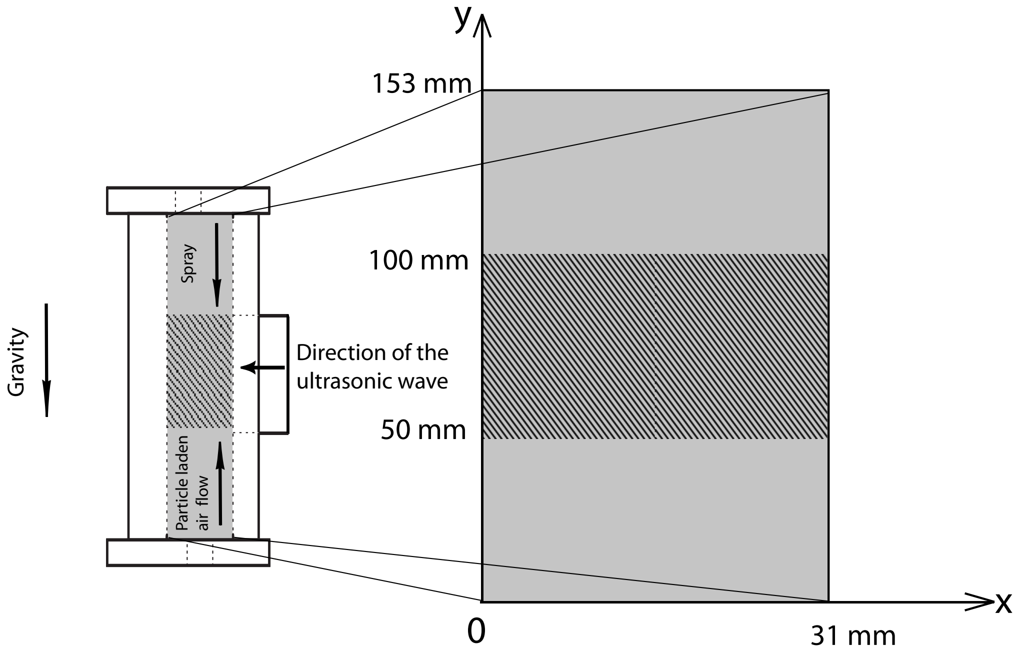

Figure 4.3: Domain dimensions and the origin of the $x - y$ coordinate system. The shaded area represents the simulated domain. The hatched area represents the area occupied by the standing wave field.

Figure 4.4 shows the spatial variation of the primary acoustic radiation force F_{ar} (predicted by Eq. (4.1)) in the x-direction of the domain and the position of the pressure nodes and pressure anti-nodes; F_{ar}=0 at both the pressure nodes and anti-nodes. The anti-nodes are points of meta-stability and hence F_{ar} drives particles to the nodes. In the simulations, F_{ar} is assumed to be insensitive to the y-direction.

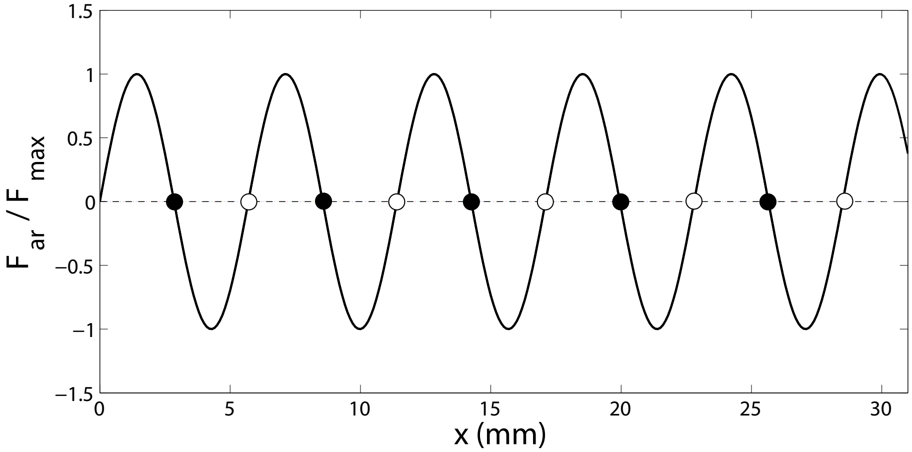

Figure 4.4: Spatial variation of the primary acoustic radiation force generated by a 30 kHz standing wave field in the domain. Filled circles represent the pressure nodes, empty circles represent the pressure anti-nodes.

Because the standing wave field only occupies a certain region of the simulation domain (see Fig. 4.3), so the governing equations of motion for the particles in different regions of the domain are different. For a particle or a drop in the region occupied by the standing wave field (50 mm< y <100 mm), the forces in the y-direction is the aerodynamic drag force and the gravitational force and the forces in the x-direction is F_{ar} and the aerodynamic drag force. For a particle or a drop in other regions of the domain where there is no standing wave field, the forces in the y-direction is the same as the region with the standing wave field and the force in the x-direction is only the aerodynamic drag force. A force balance gives:

$$m\ddot{x} = \begin{cases} F_{ar} - 3\pi\nu\rho d\dot{x} & (50 \text{ mm} < y < 100 \text{ mm}) \\ -3\pi\nu\rho d\dot{x} & (\text{otherwise}) \end{cases} \tag{4.10}$$

and

$$m\ddot{y} = -mg + 3\pi\nu\rho d(U_g - \dot{y}) \tag{4.11}$$

where m is the particle or drop mass, d is the particle or drop diameter, U_g is air velocity in the y-direction, (x,y) is the particle or drop location, ($\ddot{x}$,$\ddot{y}$) are the accelerations of the particle or drop, ($\dot{x}$,$\dot{y}$) are the absolute velocities of the particle or drop, and F_{ar} is the acoustic radiation force calculated using Eqs. (4.1)-(4.6).

By combining initial position and velocity conditions of the particle or drop with the equations listed above, their position (x,y) as a function of time is solved numerically using the explicit Runge-Kutta method[58] with a maximum relative error of 0.1% (the relative error is the estimated error of the numerical method at each time step divided by the solution at that time step). The trajectories of the particles and drops obtained from the simulations are presented in Section. 4.3.

4.3 Results of particle trajectory simulations

A sample simulation is shown in Fig. 4.5 where 50 PSL particles and 50 spray drops are initially introduced from the bottom (y=0 mm) and the top (y=153 mm) of the domain spaced $\frac{\lambda}{20}$ apart in the x-direction. For the PSL particles, due to their small mass, if they are released in the flow with zero absolute velocity, they will accelerate to 99% of the flow velocity in $\sim 10^{-5}$ s and in that amount of time they will only travel $\sim 10^{-4}$ mm. So for the sake of simplicity, their initial $\dot{y}$ is assumed to be the same as the flow velocity U_g. For the drops, their initial $\dot{y}$ was set to 0.13 m/s and directed downwards. This velocity was obtained by dividing the water spray flow rate by the cross-sectional area of the nebulizer nozzle. The initial $\dot{x}$ was set to zero for both PSL particles and spray drops. The other parameters are the same as for typical conditions in the scavenging experiments: d_p = 0.9 μm, d_d = 87 μm, and U_g = 2.8 cm/s. One thing to note here is that the trajectories of the PSL particles and the spray drops are independently simulated; the simulation does not include the interaction between them. Fig. 4.5 presents sample simulations to show the qualitative difference between the motion of particles and drops in the standing wave field. The motion of the particles is over-damped oscillation and the motion of the drops is under-damped oscillation. For the particle sizes explored in the scavenging experiments, d_p ranges from 0.7 μm to 4.2 μm, the trajectories of the particles in this size range all look similar to the plot shown in

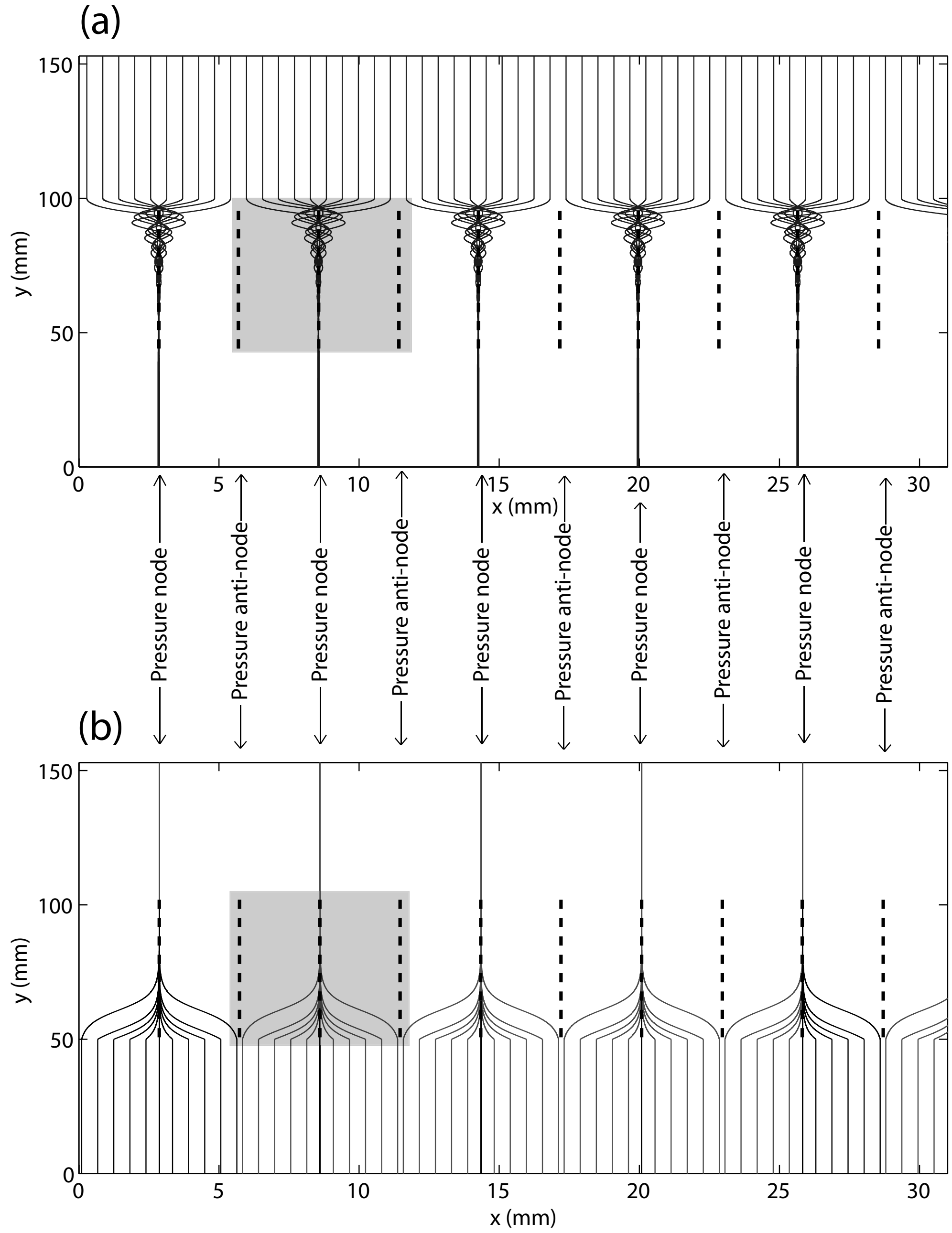

Figure 4.5: The simulated trajectories of the spray drops (a) and the PSL particles (b). Solid lines are trajectories, dashed lines are pressure node or pressure anti-node locations (a detailed view of these trajectories around a single pressure node (shaded areas) is presented in Fig. 4.8).

Fig. 4.5(b), so the trajectories of other particles in this size range are not presented here. For the drops explored in the scavenging experiments, the average d_d ranges from 40 μm to 97 μm and the trajectories vary significantly with diameter. Figure 4.6 shows this. However, it is noted that for drops in the size range explored here, the trajectories are all under-damped oscillation.

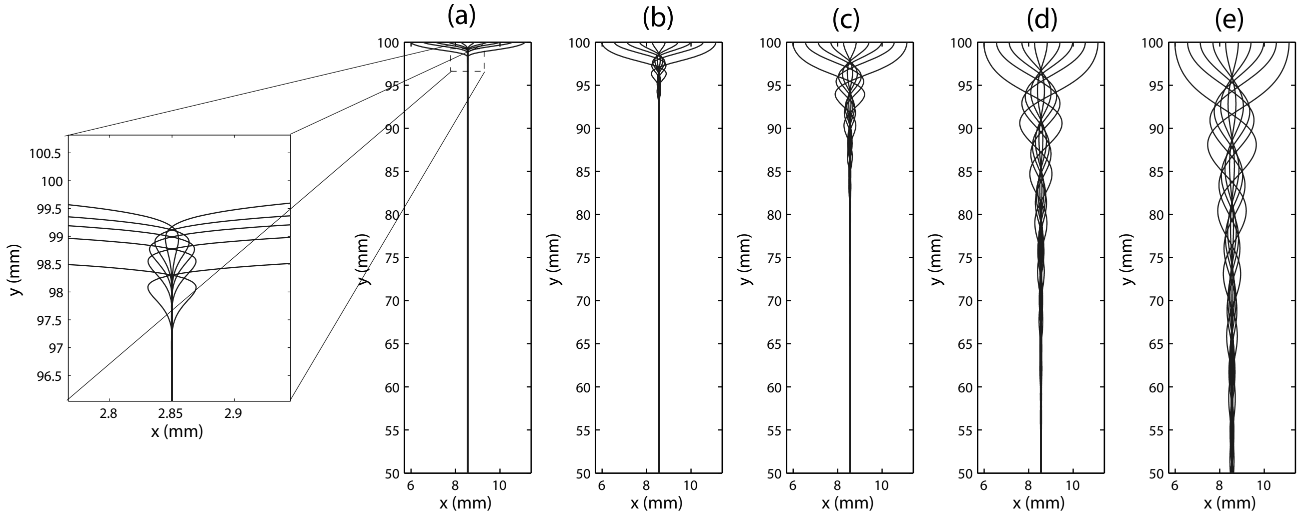

Figure 4.6: The simulated trajectories of the spray drops with different diameters for a single pressure node. (a) $d_d = 40$ μm. (b) $d_d = 56$ μm. (c) $d_d = 71$ μm. (d) $d_d = 87$ μm. (e) $d_d = 97$ μm. $U_g = 2.8$ cm/s for all cases in this figure.

The trajectories of PSL particles and spray drops at the different air velocities (U_g) explored in the scavenging experiments are shown in Fig. 4.7. The air velocities are estimated by dividing the air flow rates used in the experiments by the cross-sectional area of the scavenging chamber. Figure 4.7 shows that the trajectories of the drops are not significantly affected by varying U_g. However, the trajectories of the particles are affected by varying U_g. The higher U_g is, the less the particles are focused in the pressure node.

In Section 4.1, two possible mechanisms that could explain the increase in particle scavenging due to an ultrasonic standing wave field were described. The first mechanism, drops entraining PSL particles in their wakes, is excluded as the cause of the increased particle scavenging as shown in Section 4.2. So the remaining mechanism possibly causing the increased scavenging is the acoustic radiation force driving both the PSL particles and spray drops into the pressure nodes. Referring to Figs. 4.5-4.7, it is clear that both the PSL particles and the spray drops migrate to pressure nodes and form accretion disks after they enter the region of the standing wave field. Therefore, the mechanism mentioned above (acoustic radiation force driving both the PSL particles and spray drops into the pressure nodes) is very likely to cause the increased scavenging. However, for this mechanism, the increase could be due to (i) an increase in PSL particles combining with each other

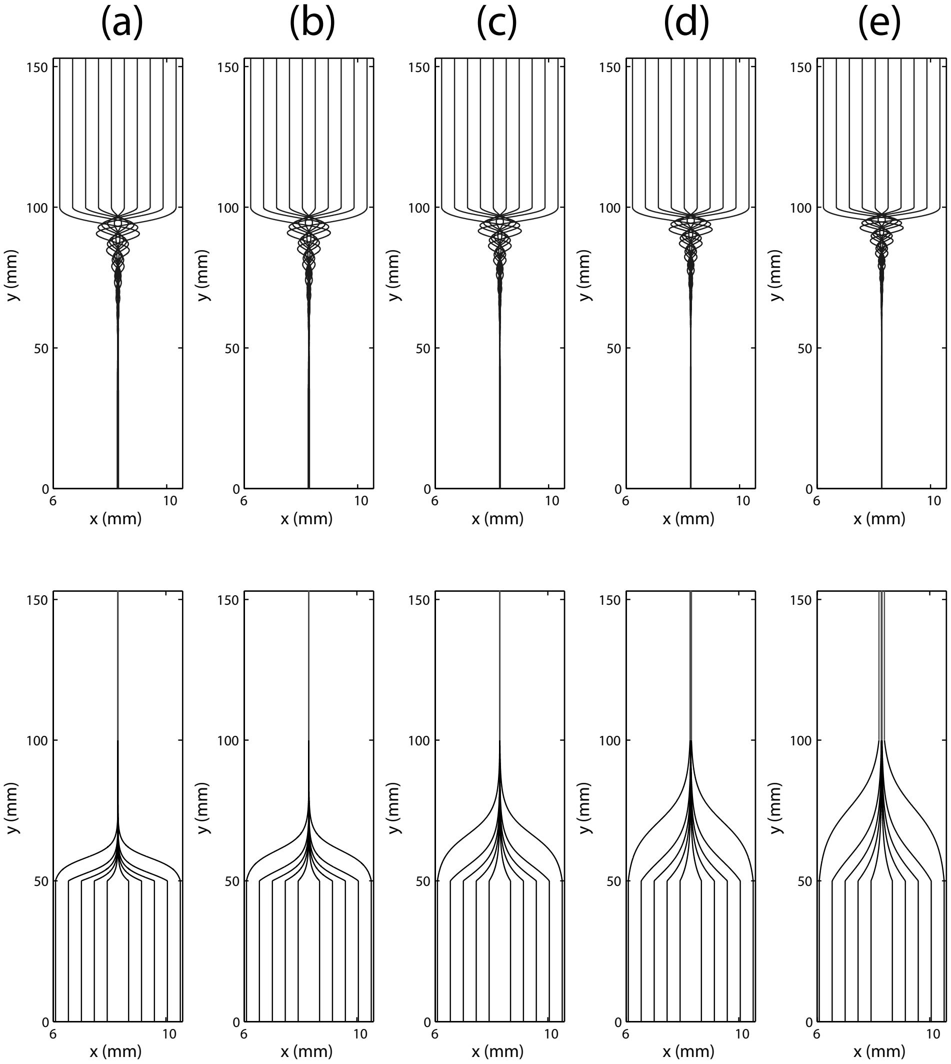

Figure 4.7: The simulated trajectories of the spray drops (top) and the PSL particles (bottom) around a single pressure node under varying air flow velocity U_g. These air velocities were used in the scavenging experiments. (a) $U_g = 2.1$ cm/s. (b) $U_g = 2.8$ cm/s. (c) $U_g = 4.2$ cm/s. (d) $U_g = 5.4$ cm/s. (e) $U_g = 6.7$ cm/s. In these simulations, $d_p = 0.9$ μm and $d_d = 87$ μm. (Additional data for this figure were obtained during the last period of this thesis research, these data are presented in Appendix B)

in the pressure nodes, or (ii) an increase in PSL particles combining with spray drops in the pressure nodes. In order to determine whether the increased scavenging is due to (i) or (ii) or a combination of these, the number concentration of drops and PSL particles in the pressure nodes is estimated based on the simulation results.

It can be noted from Figs. 4.5-4.7 that as PSL particles and spray drops move further into the standing wave field in the y-direction, their trajectories become closer together. That means their concentration should also become higher in the pressure nodes compared to other regions. To quantify the concentration increase of these particles, the envelope that bounds the trajectories in a typical region in the standing wave field are calculated. This region is bounded by two pressure anti-nodes and with a pressure node at the region's center (shaded area in Fig. 4.5). This envelope is defined as W here, and an example is illustrated in Fig. 4.8 for trajectories of the PSL particles and the spray drops in the region mentioned above.

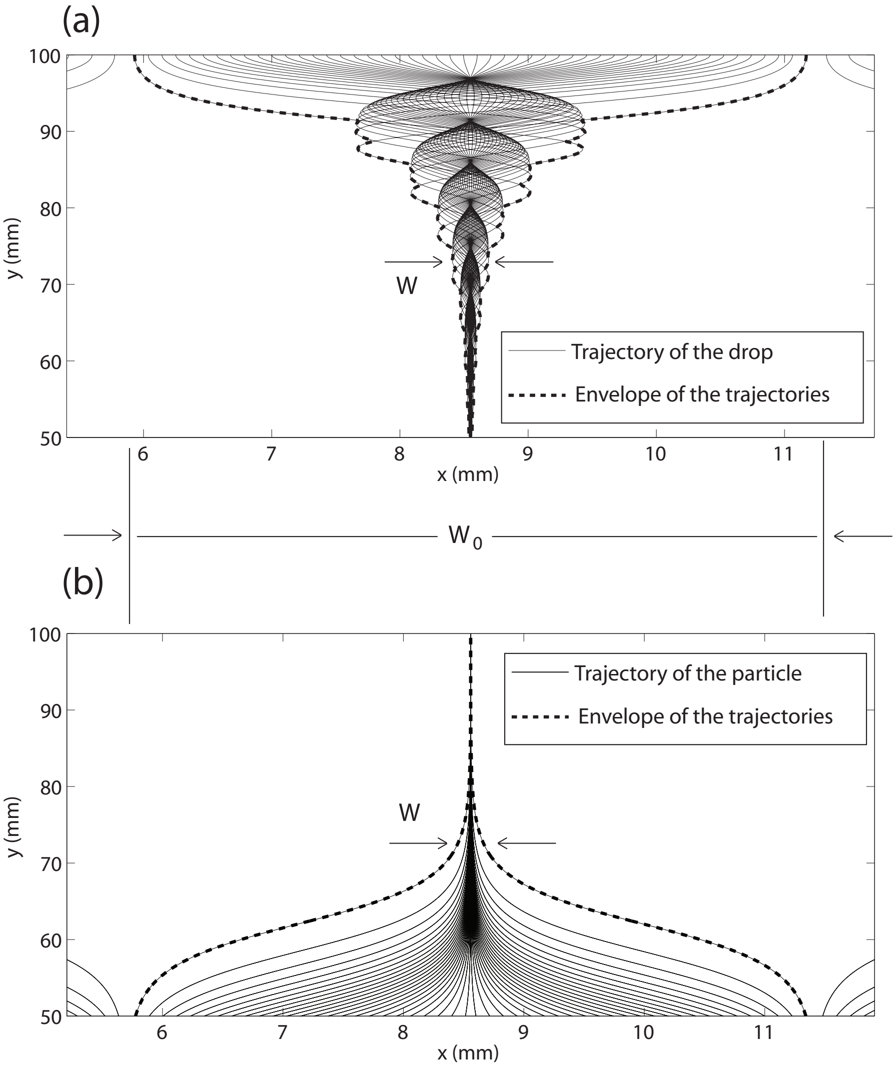

Figure 4.8: (a) Boundary of the trajectories of the spray drops that envelope a pressure node ($d_p = 87$ μm). (b) Boundary of the trajectories of the PSL particles that envelope a pressure node ($d_d = 0.9$ μm). $U_g = 2.8$ cm/s for both (a) and (b)

As shown in Figs. 4.8, W is a function of y, having a value of W_0 before entering the standing wave field; W_0 is roughly the same as the distance between two pressure anti-nodes. A particle concentration compression ratio is defined as:

$$O = \frac{W_0}{W} \tag{4.12}$$

Figures. 4.9 and 4.10 show O versus y plots for PSL particles at different air velocities and particle diameters, respectively. These air velocities and particle diameters correspond to those used in the scavenging experiments. The air velocities are estimated by dividing the air flow rates by the cross-sectional area of the scavenging chamber.

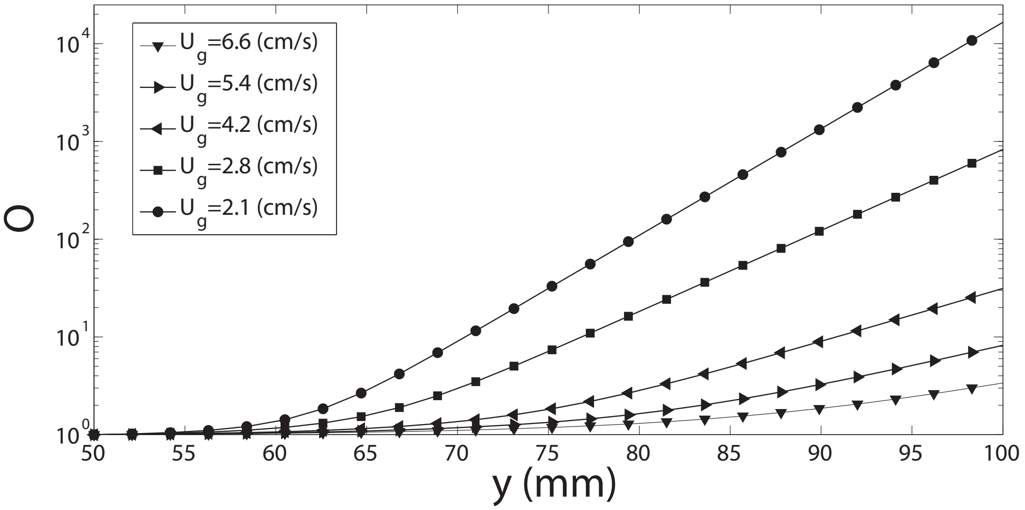

Figure 4.9: The PSL particle concentration compression ratio versus y for different air velocities U_g when particle diameter $d_p = 0.9$ μm. (Additional data for this figure were obtained during the last period of this thesis research, these data are presented in Appendix B)

It can be noted from Figs. 4.9 and 4.10 that the highest O is on the order of 10^4 (d_p=0.9 μm, U_g=2.1 cm/s). These plots cover all the scavenging experimental conditions that can affect O, so 10^4 is the global maximum of O. With the knowledge of O, the number concentration of particles at each y-location of the pressure node C can be calculated as:

$$C = C_0 O \tag{4.13}$$

where C_0 is the concentration of the particles at W_0 for the actual experiments. The highest C_0 of

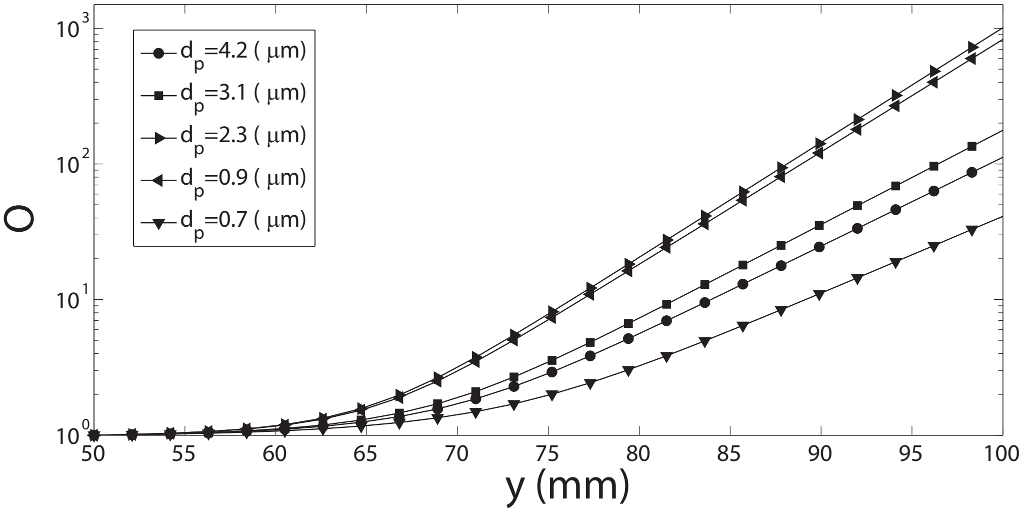

Figure 4.10: The PSL particle concentration compression ratio versus y for different particle diameters d_p when $U_g = 2.8$ cm/s.

the PSL particles in the scavenging experiments, based on measurements of the upstream particle counter, is $4 \times 10^7/\mathrm{m}^3$. As shown above, the highest O for the PSL particles is on the order of 10^4 for the conditions used in the scavenging experiments. Thus the highest possible concentration of PSL particles in the pressure nodes for the scavenging experiments is around $4 \times 10^{11}/\mathrm{m}^3$. When the number concentration of the particles becomes high enough, relative motion between the particles caused by Brownian motion, causes particles to collide and combine with each other to form larger particles. The net result is a decrease in the number concentration of particles with time. The decrease of particle number concentration with time for monodisperse particles due to particles combining with each other caused by Brownian motion is well studied and can be described as:[59]

$$E_c = \left(1 - \frac{1}{1 + C_{t_0} K \left(t - t_0\right)}\right) \times 100\% \tag{4.14}$$

where E_c is the percent decrease of particle number concentration, C_{t_0} is the original particle concentration at time t_0, t is time, and K is the particle coagulation coefficient, which for 0.9 μm particles in standard conditions is[59] $3.4 \times 10^{-16}\mathrm{m}^3/\mathrm{s}$. The above equation is based on the assumptions that every particle collision leads to a combination, for each combination there is a reduction of one in the number of particles, and the change of particle size due to particle combinations does not affect further particle combinations. One thing to note here is that particle-particle combinations do not result in the elimination of these particles; though the total particle number is reduced in this process, the total mass of the particles is conserved. According to Eq. (4.14), for monodisperse particles with $d_p = 0.9\ \mu\text{m}$ and $C_{t0} = 4 \times 10^{11}/\text{m}^3$, the particle number concentration will reduce by 0.1% after 10 s. According to the simulation, the longest residence time (under the lowest air flow rate) of the PSL particles in the scavenging chamber is 7.5s. Accordingly, the particle-particle interactions in the pressure nodes is not likely to cause the increased scavenging observed in these experiments.

Of the mechanisms described earlier, the only one left is the increase in scavenging due to an increase in PSL particles combining with spray drops in the pressure nodes. Of course some unknown mechanism that is not considered here could also be the cause. So, to go beyond a process-of-elimination proof that drop-particle interactions are the cause of increased scavenging observed here these simulations are used to estimate the PSL scavenging by drops, and these are compared to the experimental results.

It is not possible to predict the particle-drop scavenging solely from the trajectory simulation presented here. However, these trajectories can be used to show that particle-drop scavenging explains the experimental results. The first step in this process is to calculate the number concentration C for the PSL particles and the spray drops in the pressure node. This is done using Eq. (4.13) in the same way for spray drops as for PSL particles. The original number concentration of spray drops before they enter the standing wave field C_0 is estimated based on the water flow rate Q_l and the average drop diameter d_d (here all drops are assumed to have the same size). The number of drops generated per unit time is:

$$N_t = \frac{6Q_l}{\pi {d_d}^3} \tag{4.15}$$

If the time a drop travels in the scavenging chamber before hitting the bottom of the chamber is t_s (which can be obtained from the simulation results) then, the total number of drops in the scavenging chamber N is:

$$N = N_t t_s \tag{4.16}$$

If the total volume of the scavenging chamber is V_s, then the number concentration of the drops in the scavenging chamber (assuming the spray drops are evenly distributed) is:

$$C_0 = \frac{N}{V_s} = \frac{6Q_l t_s}{\pi {d_d}^3 V_s} \tag{4.17}$$

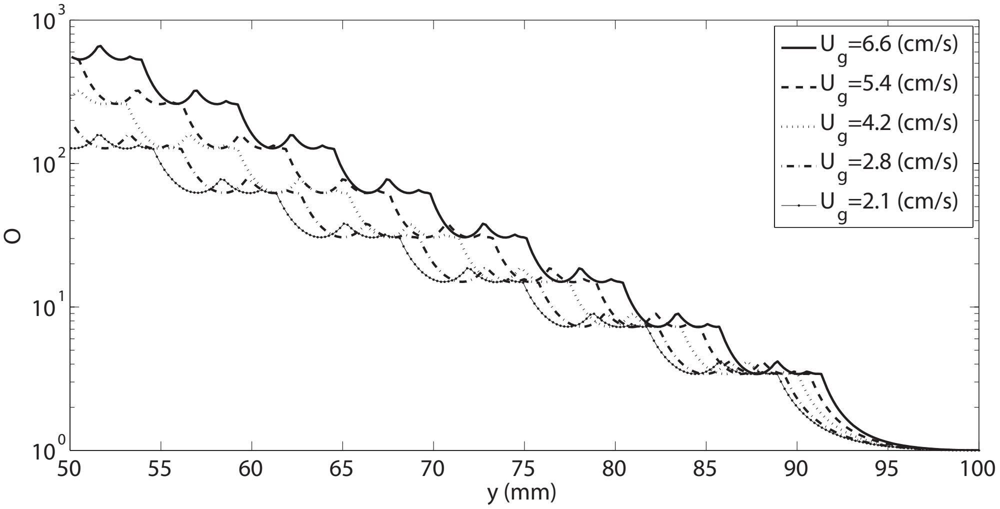

Figure 4.11: The spray drop concentration compression ratio versus y for different air velocities U_g when drop diameter $d_d = 87$ μm.

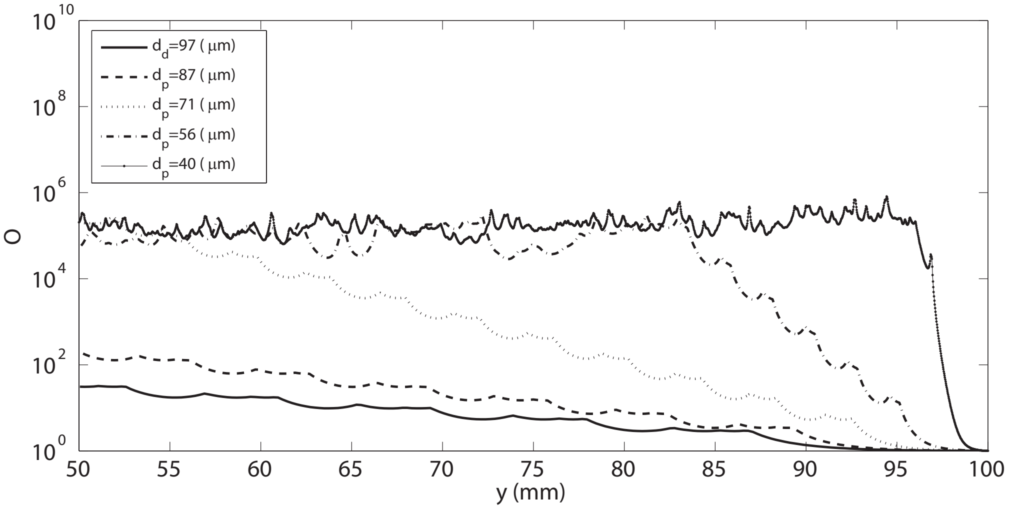

Figure 4.12: The spray drop concentration compression ratio versus y for different drop diameters d_d when $U_g = 2.8$ cm/s.

Similar to Figs. 4.9 and 4.10, Figs. 4.11 and 4.12 show O versus y plots for spray drops at different air velocities and drop diameters, respectively. With O for PSL particles and spray drops, the number concentrations of particle or drop at each y-location of the pressure node, C, can be obtained using Eq. (4.13). An example plot of C versus y for PSL particles and spray drops in the pressure node is shown in Fig. 4.13, for the case where $d_p = 0.9$ μm, $d_d = 87$ μm, $U_g = 2.8$ cm/s and $Q_l = 0.92$ ml/s. Figure 4.13 shows that the concentration of the PSL particles increases with y while the concentration of the spray drops decreases with y. This is simply because the particles enter the standing wave field from the bottom of the scavenging chamber while the drops enter from the top as shown in Fig. 4.5.

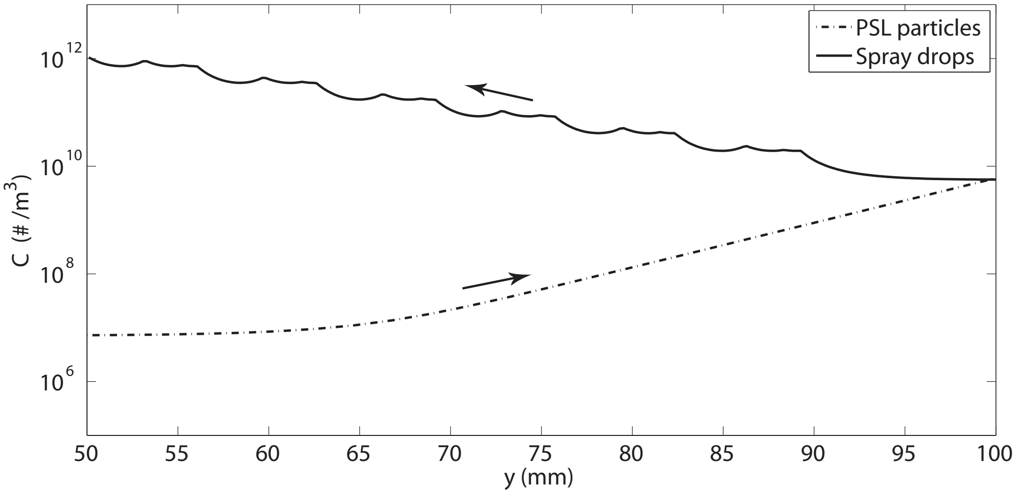

Figure 4.13: The number concentration versus y for PSL particles and spray drops in the pressure node. Here $d_p = 0.9$ μm, $d_d = 87$ μm, $U_g = 2.8$ cm/s and $Q_l = 0.92$ ml/s. The arrows indicate the direction of travel of the particles/drops.

Given the particle and drop number concentration as a function of y, C_p and C_d, respectively, the frequency of drop-particle collision can be written as:[59]

$$f_c = K_c C_p C_d, \tag{4.18}$$

where f_c is the potential collision frequency per unit volume between particles and drops, and K_c is the collision coefficient, which quantifies the rate of collisions between particles and drops in a certain volume of space, and has units of m^3/s.

To apply Eq. (4.18) for the case of the pressure node, one needs to consider two facts:

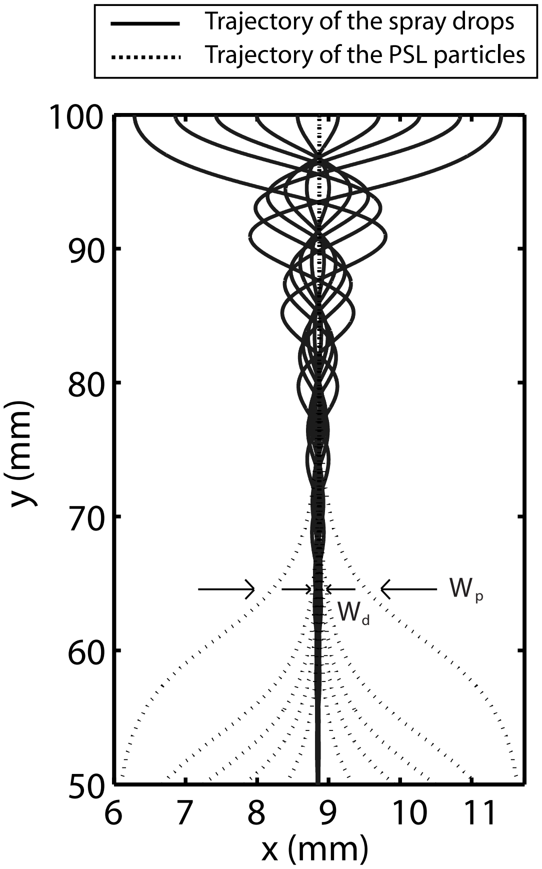

Figure 4.14: Overlapped trajectories of PSL particles and spray drops. Here $d_p = 0.9$ μm, $d_d = 87$ μm, $U_g = 2.8$ cm/s.

First C_p and C_d are a function of y in the pressure node as shown in Fig. 4.13. Second the envelope containing the PSL particles and the spray drops occupy different volumes. This is best illustrated by Fig. 4.14 which shows the overlapped trajectories of PSL particles and spray drops. From Fig. 4.14, it can be noted that in some y locations, W is smaller for the spray drops than for the PSL particles. In these locations, only a portion of the PSL particles are exposed to the spray drops. To consider these two facts, Eq. (4.18) is modified as:

$$f_c = \begin{cases} K_c C_p C_d \frac{W_d}{W_p} & (W_p > W_d) \\ K_c C_p C_d & (\text{otherwise}) \end{cases} \tag{4.19}$$

In Eq. (4.19), when $W_p > W_d$, the width of the trajectories of the spray drops is smaller than the width of the trajectories of the PSL particles and so only a portion of the PSL particles is exposed to the spray drops (see Fig. 4.14); f_c is reduced accordingly. The reason to reduce f_c as shown in Eq. (4.19) is: when $W_p > W_d$, the volume occupied by both the PSL particles and spray drops is proportional to W_d, so $f_c = K_c C_p C_d$ within this volume. Outside this volume $f_c = 0$. Because the total volume that the PSL particles occupy is proportional to W_p, so the average f_c for the PSL particles should be $K_c C_p C_d W_d + 0 \times (W_p - W_d)$ divided by W_p, which equals $K_c C_p C_d \frac{W_d}{W_p}$.

The variable f_c is defined as the *potential* collision frequency because even if a particle and a drop are on a potential collision path, that does not guarantee that the particle will eventually combine with the drop. As described in the introductory chapter, when a particle approaches a drop, it may follow the streamline around the drop and avoid collision with the drop. Whether a particle on a collision path with a drop will eventually combine with the drop depends on the scavenging coefficient for a single drop:

$$E_s = \frac{n_1}{n_2} \tag{4.20}$$

Where n_2 is the total number of particles on a collision path with the drop and n_1 is the number of particles that will eventually combine with the drop. E_s is a complex function of the size of the particle and the drop, their relative velocity and other parameters.[60] Knowing E_s, one can estimate the rate of PSL particles scavenging by drops per unit volume at a location y in the pressure node (defined as S here) as:

$$S = f_c E_s \tag{4.21}$$

One thing to note here is though $S > 0$ in the pressure nodes, the concentration of particles in the pressure nodes at any location should not vary with time (i.e. $\frac{dC_p}{dt} = 0$). This is because the scavenging chamber is operated in a nominally steady-state condition, the particles scavenged by drops at any location will be balanced by particles flowing into this location. The rate of PSL particles scavenging by drops per unit volume for the whole pressure node, $\bar{S}$, is estimated by taking the average of S over the whole pressure node as:

$$\bar{S} = \frac{\int_{y_1}^{y_2} S dy}{y_2 - y_1} \tag{4.22}$$

because in the simulation S is not contentious, the discrete form of Eq. (4.22) is:

$$\bar{S} = \frac{\sum\limits_{y=y_1}^{y=y_2} S\Delta y}{y_2 - y_1} \tag{4.23}$$

where y_1 and y_2 are the locations at either end of the pressure node, for the case shown in Fig. 4.13, y_1 = 50 mm, y_2 = 100 mm and Δy = 0.05 mm. By combining Eqs. (4.19), (4.21) and (4.23) and assuming E_s and K_c are not a function of y yields:

$$\bar{S} = \begin{cases} E_s K_c \frac{\sum\limits_{y=y_1}^{y=y_2} C_p C_d \frac{W_d}{W_p} \Delta y}{y_2 - y_1} & (W_p > W_d) \\ E_s K_c \frac{\sum\limits_{y=y_1}^{y=y_2} C_p C_d \Delta y}{y_2 - y_1} & \text{(otherwise)} \end{cases} \tag{4.24}$$

Since the scavenging chamber is operated in a nominally steady-state condition, all of the variables on the right hand side of Eq. (4.24) do not vary with time. Hence, $\bar{S}$ should be a constant at any particular location (balanced by particles flowing into the chamber). Therefore, E_p, the scavenging coefficient of PSL particles by spray drops in the pressure node can be estimated as:

$$E_p = \frac{\bar{S} t_s}{C_0} = \begin{cases} E_s K_c t_s \frac{\sum\limits_{y=y_1}^{y=y_2} C_p C_d \frac{W_d}{W_p} \Delta y}{(y_2 - y_1) C_0} & (W_p > W_d) \\ E_s K_c t_s \frac{\sum\limits_{y=y_1}^{y=y_2} C_p C_d \Delta y}{(y_2 - y_1) C_0} & \text{(otherwise)} \end{cases} \tag{4.25}$$

where t_s is the time the PSL particles reside in the pressure node and C_0 is the concentration of the PSL particles before they enter the pressure node. Without values for E_s and K_c, E_p can not be obtained. However, if E_s and K_c are assumed constant, then the variation in the scavenging for different experimental conditions can be determined. That is, writing

$$E_p = \Lambda E_s K_c \tag{4.26}$$

where

$$\Lambda = \begin{cases} \frac{t_s \sum\limits_{y=y_1}^{y=y_2} C_p C_d \frac{W_d}{W_p} \Delta y}{C_0 (y_2 - y_1)} & (W_p > W_d) \\ \frac{t_s \sum\limits_{y=y_1}^{y=y_2} C_p C_d \Delta y}{C_0 (y_2 - y_1)} & \text{(otherwise)} \end{cases} \tag{4.27}$$

then, assuming E_s and K_c remain unchanged when Λ is varied (the conditions that must be satisfied for this assumption to be valid is discussed later):

$$E_p \propto \Lambda \tag{4.28}$$

If this is the case, then a value for Λ can be calculated from the simulated trajectories of PSL particles and spray drops under a single set of conditions (air flow rate, water flow rate, particle size and drop size) and compared to other conditions. If these variations track the actual experimental data, then it is likely that the increased scavenging observed here is due to a drop-particle combinations.

For each experiment presented in this study a scavenging coefficient was computed with and without the ultrasonic standing wave field, E_w and E_{wo}, respectively. Here a variable (E_I) is defined to quantify the increased particle scavenging due to the standing wave field as:

$$E_I = E_w - E_{wo} \tag{4.29}$$

Figure 4.15 presents plots of E_I and Λ versus air flow rate Q_g. It is clear from Fig 4.15 that I and Λ share a similar trend when plotted versus Q_g. The error bars of E_I in Fig. 4.15(a) are calculated based on the theory of propagation of uncertainty[50] from 95% confidence intervals of E_w and E_{wo}. Figure 4.16 is a plot of E_I versus Λ obtained by combining plots (a) and (b) in Fig. 4.15. This plot shows that there is a linear correlation (the straight line shown in Fig. 4.16) between E_I and Λ (on log scale). Figure 4.17 presents plots of E_I and Λ versus water flow rate Q_l. To make it comparable to Fig 4.15, the scale of vertical axises of plots in Fig. 4.17 are set to be the same as the plots in Fig 4.15. Figure 4.17 shows that the trend E_I and Λ share when plotted versus Q_l is not as strong as the trend E_I and Λ share when they are plotted versus Q_g. When plots (a) and (b) in Fig. 4.17 are combined to generate a plot of E_I versus Λ and the new data points are added to Fig. 4.16, the resulting plot (Fig. 4.18) shows that E_I and Λ obtained based on results from varying the water flow rate Q_l can also be collapsed into the same straight line with E_I and Λ obtained based on results from varying the air flow rate Q_g. Similar to Q_g and Q_l, Fig. 4.19 presents plots of E_I and Λ versus PSL particle size d_p and Fig. 4.20 presents plots of E_I and Λ versus spray drop size d_d. However, as shown in Fig. 4.21, when E_I and Λ obtained based on results from varying the PSL particle size d_p and spray drop size d_d are also added to the plot in Fig. 4.18, the linear correlation between E_I and Λ (on log scale) disappears.

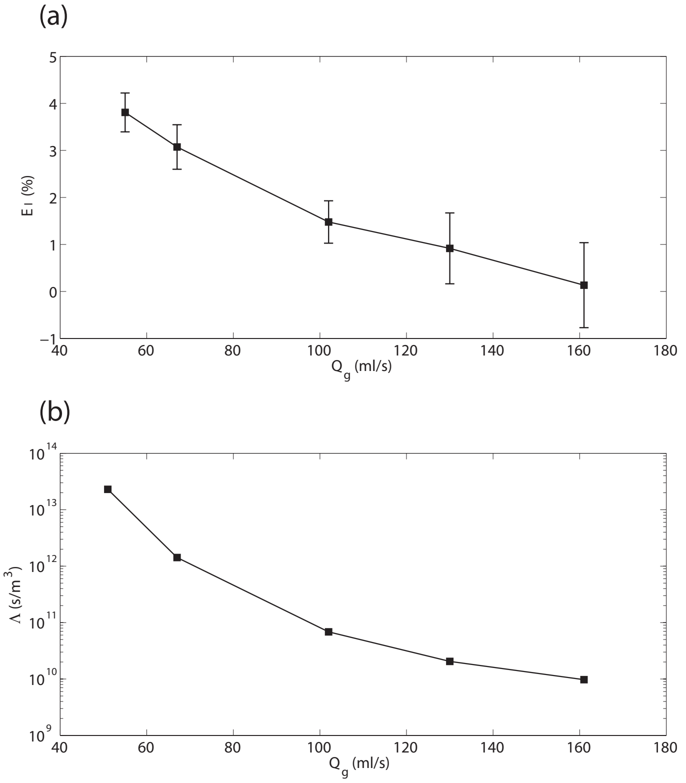

Figure 4.15: Compare E_I and Λ versus air flow rate Q_g. (a) E_I versus Q_g. (b) Λ versus Q_g. (Additional data for this figure were obtained during the last period of this thesis research, these data are presented in Appendix B)

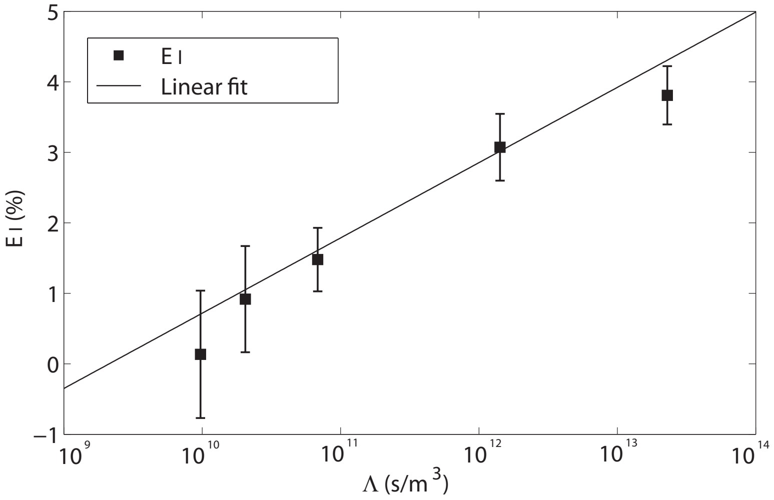

Figure 4.16: Plot of E_I versus Λ for varying air flow rate Q_g (Additional data for this figure were obtained during the last period of this thesis research, these data are presented in Appendix B)

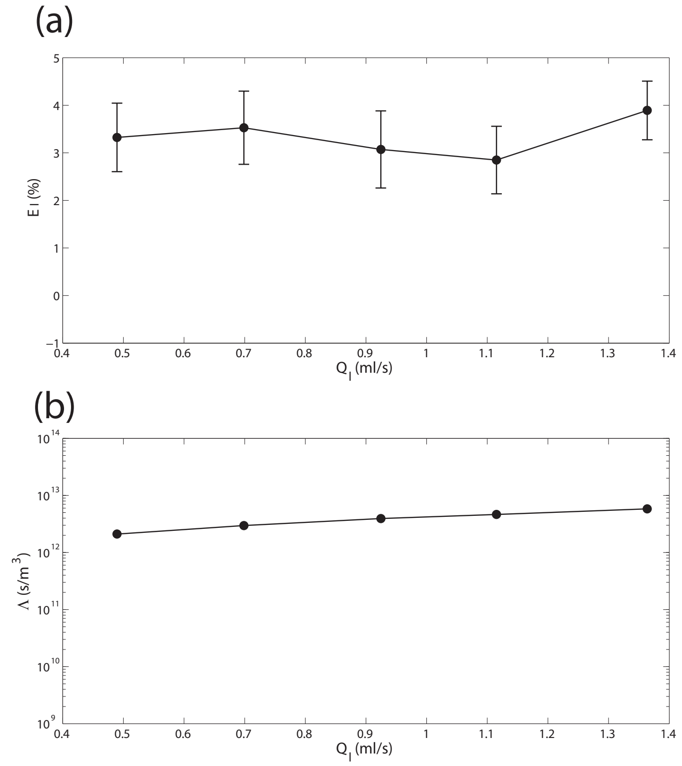

Figure 4.17: Compare E_I and Λ versus water flow rate Q_l. (a) E_I versus Q_l. (b) Λ versus Q_l . (Additional data for this figure were obtained during the last period of this thesis research, these data are presented in Appendix B)

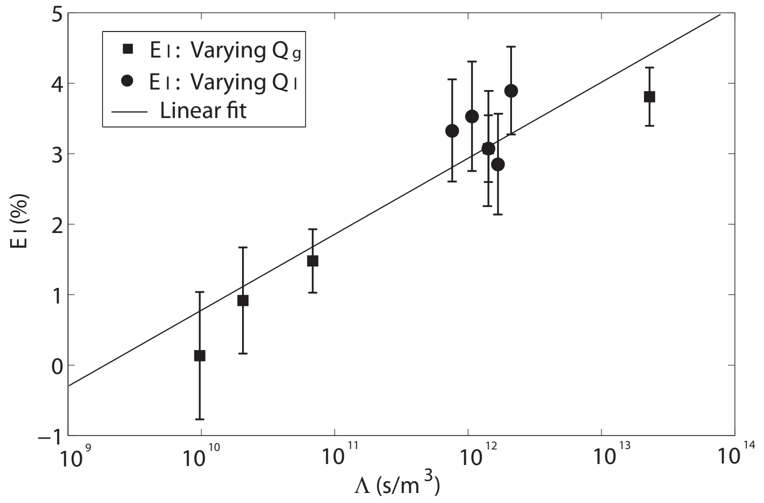

Figure 4.18: Plot of E_I versus Λ for varying air flow rate Q_g and varying water flow rate Q_l. (Additional data for this figure were obtained during the last period of this thesis research, these data are presented in Appendix B)

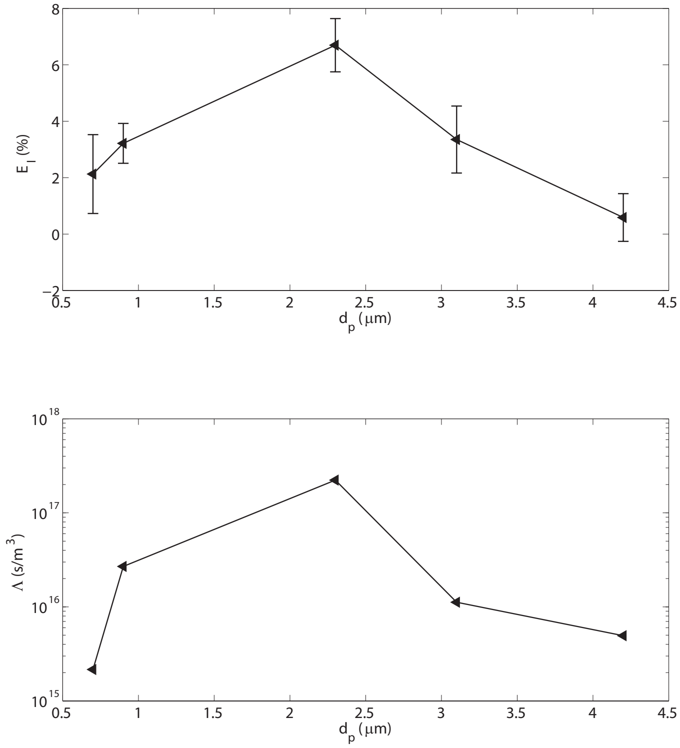

Figure 4.19: Compare E_I and Λ versus PSL particle size d_p. (a) E_I versus d_p. (b) Λ versus d_p.

There are two possible reasons why data obtained from varying d_p and d_d can not be collapsed with data obtained from varying Q_g and Q_l. The first reason is that the positive correlation between Λ and E_p is based on the assumption that E_s and K_c remained unchanged for different Λ. As shown below, this is probably true for Λ in the case of varying Q_g and Q_l, but not true for Λ when d_p and d_d are varied. Based on the theory by Slinn,[60] E_s is a strong function of Stokes number:

$$Stk = \frac{\rho_p U_{pd} {d_p}^2}{9 \nu d_d} \tag{4.30}$$

where ρ_p is the density of the particle, U_{pd} is the relative velocity between the particle and drop, and ν is the kinematic viscosity of the surrounding gas. Stk will not be affected when Q_l, the water flow rate, is varied. When Q_g, the air flow rate, is varied, Stk may vary since U_{pd} may change with Q_g. However, U_{pd} actually remains unchanged when Q_g is varied becasue the simulations show the drops used in the experiments are falling at their terminal velocity in the y-direction when they

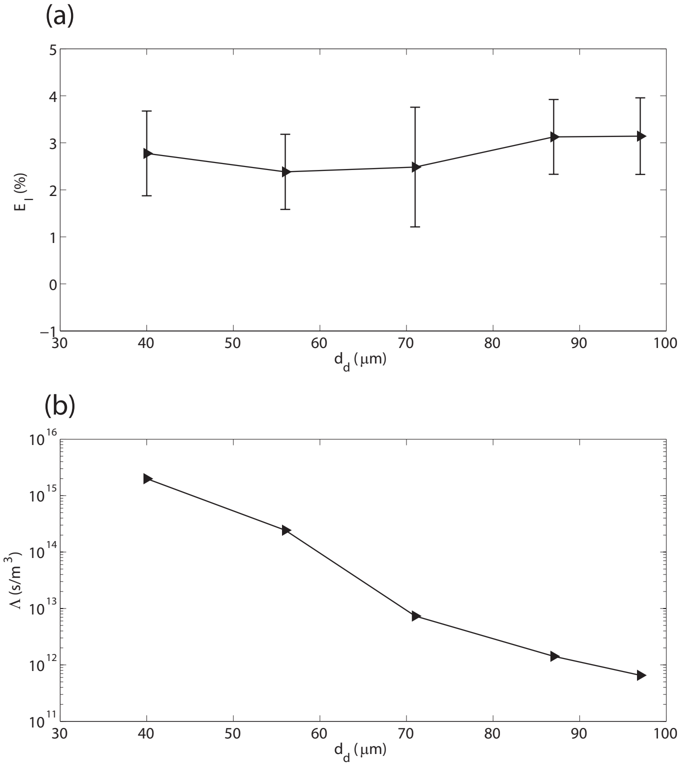

Figure 4.20: Compare E_I and Λ versus spray drop size d_d. (a) E_I versus d_d. (b) Λ versus d_d.

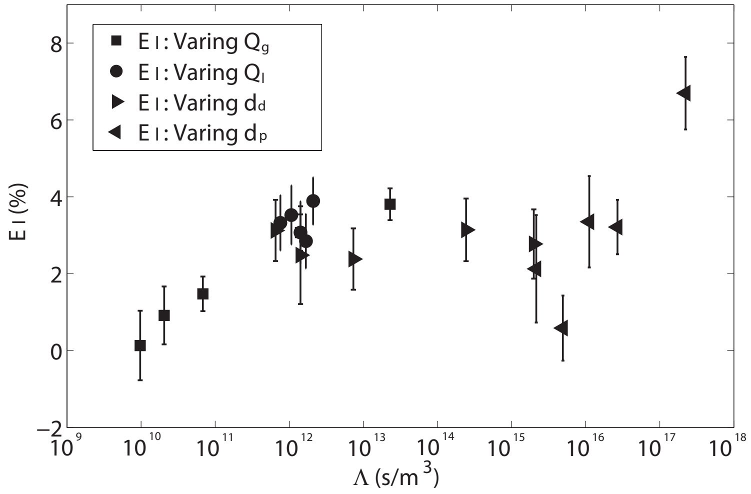

Figure 4.21: Plot of I versus Λ for varying air flow rate Q_g, water flow rate Q_l, PSL particle size d_p and spray drop size d_d. (Additional data for this figure were obtained during the last period of this thesis research, these data are presented in Appendix B)

enter the pressure node. So the velocity of the drop in the y-direction is:

$$U_d = U_g - \frac{mg}{3\pi\nu\rho d_d} \tag{4.31}$$

where U_g is the air velocity in the y-direction, which is the only parameter that is dependent on Q_g in Eq. (4.31), and m is the mass of the drop. Due to the small mass of particles used in the experiments, particle velocity in the y-direction can be approximated to be the same as U_g, so U_{pd} can be calculated as:

$$U_{pd} = U_d - U_g = -\frac{mg}{3\pi\nu\rho d_d} \tag{4.32}$$

The above equation shows U_{pd} is independent of Q_g, so Stk is independent of Q_g. But Stk is a function of d_p and d_d as shown in Eq. (4.30). So varying d_p and d_d can affect E_s.

For the parameter K_c, depending on the mechanisms that cause the relative motion between the particles and drops: difference in diffusion rate, difference in settling velocity, difference in electrostatic mobility, and turbulence,[61, 59, 62, 63] the functional form of K_c varies. Because the potential electrostatic charges on the particles were neutralized and Re of the flow in the scavenging chamber (assuming the chamber is a rectangular pipe) was 60 for the conditions of scavenging experiments, the effect of difference in electrostatic mobility and the effect of turbulence can be excluded. Therefore, in the scavenging experiments, the mechanisms that cause the relative motion between the particle and the drop are most likely due to the difference in their diffusion rate and inertia. The diffusion rate and inertia of the particle and the drop are dependent on their diameters, d_p, d_d. Accordingly, it can be concluded that, like E_s, K_c remains unchanged for varying air flow rate Q_g or water flow rate Q_l, but does change when particle diameter d_p or drop diameter d_d is varied.

The second possible explanation for why data obtained from varying d_p and d_d can not be collapsed with data obtained from varying Q_g and Q_l is: Λ is calculated from the simulation results and relies on F_{ar} predicted by the theory of Settnes and Bruus.[42] The direction of F_{ar} on the PSL particles has been verified by the experiments presented in Chapter 3, however, the magnitude of F_{ar} has never been verified. It is possible that the prediction of the magnitude of F_{ar} by Settnes and Bruus[42] as a function of d_p and d_d is not accurate. So it is also possible that the results where d_p and d_d are varied need to be better simulated with a more accurate theory of F_{ar}.

Though there are some limitations of the analyses presented above, these analyses still show: First, Λ and E_I obtained from the simulations and the scavenging experiments with varying Q_g and Q_l are positively correlated to each other. Secondly, Λ is also positively correlated to E_p. So E_I also should be positively correlated to E_p. Because E_p is the scavenging coefficient of PSL particles by spray drops in the pressure node, and E_I quantifies the increased particle scavenging due to the standing wave field, this adds additional evidence to the conclusion that the mechanism caused increased scavenging is due to an increase in PSL particles combining with spray drops in the pressure nodes.

With the correlation between E_I and Λ established above, it can be useful for future industrial applications of ultrasonic scrubber by predicting E_I for particle concentrations outside of the range investigated in scavenging experiments in Chapter 2. Because the particle concentrations of uncontrolled industrial emissions are much higher than the particle concentrations used in the scavenging experiments. The concentrations of fine particles (particles with $\sim$1 μm diameter) of uncontrolled industrial emissions range from 10^{10} /m^3 to 10^{13} /m^3,[64] which is much higher than 4×10^7 /m^3 investigated in the scavenging experiments. If the ultrasonic scrubber is used to treat these emissions and keeping other parameters the same as the typical scavenging experiments, (e.g. d_p=0.9 μm, d_d=87 μm, Q_l=0.92 ml/s and Q_g=67 ml/s), then Λ calculated from Eq. (4.27) increases to 10^{22} s/m^3 – 10^{25} s/m^3 from $\sim 10^{10}$ s/m^3 – $\sim 10^{14}$ s/m^3. This is a significant increase. From Fig. 4.18, a correlation between E_I and Λ can be obtained:

$$E_I = 1.18 \log_{10} \Lambda - 11.27 \tag{4.33}$$

Based on the above correlation, E_I of the ultrasonic scrubber at the particle concentrations typically found in industrial emissions is estimated to range from 15% to 18%. However, E_I could be even higher than this estimate. This is because the effect of particle-particle interactions is not considered in the estimation of E_I (E_I is estimated based only on the particle-drop interactions) since the analysis presented earlier showed that for the particle concentrations investigated in the scavenging experiments, the effect of particle-particle interactions was negligible. But at the higher particle concentrations found in industrial emissions, particle-particle interactions are significant. If the ultrasonic scrubber is used to treat industrial emissions, and assuming other parameters are the same as the typical scavenging experiments, where the particle concentration compression ratio is $O \simeq 5 \times 10^3$, the residence time of particles in the ultrasonic scrubber is 2 s, and the particles are monodisperse with $d_p = 0.9$ μm, and only particle-particle interactions are considered, then using Eqs. (4.13) and (4.14), E_c is found to be ranging from 3% to 97%, which is significant compared with E_I estimated based only on the particle-drop interactions.

4.4 Limitations of the simulation

There are limitations of the trajectories simulation of PSL particles and spray drops presented above. In the actual experiment, these particles are probably less focused in the pressure nodes than predicted by the simulation due to the following three limitations of the simulation: First, the standing wave field in the scavenging chamber is assumed to be a perfect plane wave field in the simulation. However, a true plane wave can only be generated by an infinite sized transducer with a perfectly smooth surface, which is not true for the case in the actual experiment. Second, the air velocities in the x-direction are ignored in the simulation because the dominant air flow is in the y-direction. However, in the actual experiment, small air velocities in the x-direction may disperse the well focused particles in the pressure nodes. Third, compared to other cross-sections of the scavenging chamber, the particles moving in the cross-section used to conduct the simulation have the longest residence time in the standing wave field, so particles in all other cross-sections of the scavenging chamber should be less focused in the pressure nodes than predicted by the simulation.

4.5 Possibilities of discrepancy of d_{c0}

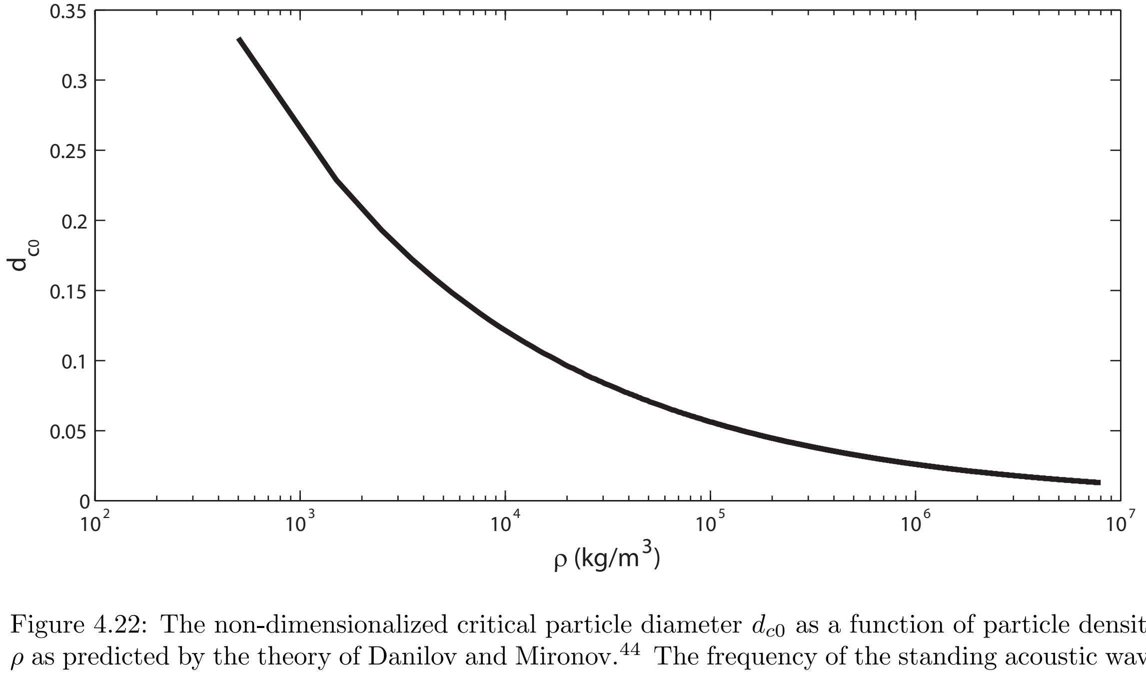

Figure 4.22: The non-dimensionalized critical particle diameter d_{c0} as a function of particle density ρ as predicted by the theory of Danilov and Mironov.[44] The frequency of the standing acoustic wave field was 30 kHz and the surrounding fluid was air, same as the experiments.

The experimental results presented in Chapter 3 show that the acoustic radiation force could either drive a micron-scale particle to migrate to the pressure nodes or the pressure anti-nodes of a standing wave field depends on the particle's diameter. However, the dimensionless critical diameter d_{c0} at which the force changes direction obtained in the experiments does not agree with the predication made by Danilov and Mironov[44] presented in the introductory chapter. The theory's predication of d_{c0} for water drops ($d_{c0} < 0.35$) is around an order of magnitude larger than the experimental results obtained using smoke particles ($0.015 < d_{c0} < 0.031$) and PSL particles ($d_{c0} < 0.07$), though in agreement with the results obtained from the water drop experiments.

One possibility of this discrepancy may be due to the difference in the density of water and PSL/smoke particles. However, as shown in Fig. 4.22, Danilov and Mironov's theory[44] requires that the density of the particles would needs to be unrealistic high ($\rho \sim 10^5$ kg/m^3 or $\rho \sim 10^7$ kg/m^3) in order for d_{c0} obtained for the PSL and smoke particles in the experiments to agree with the theory. So this possibility is eliminated here.

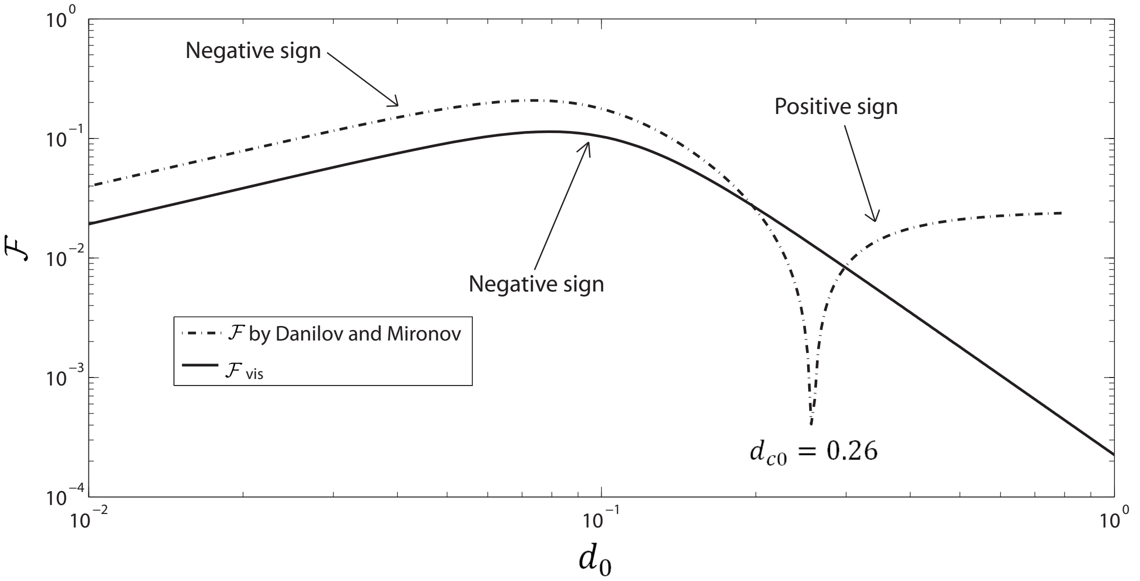

Figure 4.23: Comparison between the $\mathcal{F}$ on a water drops generated by a standing wave field at a frequency of 30 kHz in air predicted by Danilov and Mironov[44] and due to the change of the viscosity of the fluid in the sound wave predicted by Czyz.[65] Arrows indicate regions where the sign of the $\mathcal{F}$ are different and d_{c0} is the non-dimensionalized critical particle diameter where the sign of the force may flip.

The second possibility is that the discrepancy is due to mechanisms that contribute to the force on particles in the acoustic field, that were not considered in the theory of Danilov and

Mironov.[44] One such mechanism is the change of the viscosity of the fluid due to the periodic adiabatic compressions and rarefactions of the sound wave.[44] Danilov and Mironov used constant viscosity for the fluid medium in their theory, which is not true in the sound wave. The change of the fluid viscosity in the sound wave may alter $\mathcal{F}$. This has been investigated by Westervelt[66] and Czyz.[65] Figure. 4.23 shows a comparison between $\mathcal{F}$ predicted by Danilov and Mironov[44] and the force caused by the change of the viscosity of the fluid predicted by Czyz.[65] In order to compare these two forces, the force predicted by Czyz[65] is transformed into dimensionless form $\mathcal{F}_{vis}$ using Eq. (1.4). From Fig. 4.23, it is clear that at certain particle diameters, $\mathcal{F}_{vis}$ is on the same order or even larger than $\mathcal{F}$, and it is possible that d_{c0} could shift due to interactions between $\mathcal{F}_{vis}$ and $\mathcal{F}$. But even with the knowledge of $\mathcal{F}_{vis}$, it is not clear how to use it to correct $\mathcal{F}$. One could simply add these two forces. However, because the potentially complex, nonlinear interactions between the different mechanisms, simple addition or linear combination of these two forces are not likely to work. To have a more accurate predication of $\mathcal{F}$, further investigation is needed to understand the interaction between these mechanisms.

The last possibility is that d_{c0} may depends on other material properties of the particle such as compressibility. Though other theories[41,42,43] that predict $\mathcal{F}$ do not predict the sign change and d_{c0}, particle compressibility is nevertheless an important parameter used in these theories to decide $\mathcal{F}$. So the discrepancy may caused by the difference in the compressibility between water and PSL/smoke particles.

4.6 Conclusion

The particle scavenging experiments presented in this thesis research demonstrate that an ultrasonic standing wave field can be used to improve the scavenging of micron-scale particles by water sprays. The increase in the scavenging coefficient due to an ultrasonic standing wave field was observed over a range of water flow rates, particle sizes, spray drops sizes, and air flow rates.

The experimental validation of the direction of the acoustic radiation force $\mathcal{F}$ shows the direction of $\mathcal{F}$ is dependent on the particle diameter. The direction change behavior was observed for water drops and smokes particles. The critical diameter d_c where $\mathcal{F}$ changes direction is roughly estimated to be smaller than 4.6 μm for water drops and between 0.2 μm to 0.4 μm for smoke particles. The direction change behavior was not observed for PSL particles ranging from 0.9 μm to

4.5 μm. This investigation suggests that the difference in d_c for varying types of particles is probably caused by the difference in the compressibilities of different types of particles. And the difference between d_c predicted by the theory of Danilov and Mironov[44] and d_c obtained through experiments may be caused by the effect of changes in the viscosity of the fluid within the sound wave, this effect has not been considered by the theory.

Theory of Settnes and Bruus[42] was used to simulate the trajectories of the spray drops and the particles in an ultrasonic standing wave field. By analyzing the results obtained from both the simulations and the scavenging experiments, it was concluded that the increased scavenging is caused by an increase in particles combining with spray drops in the pressure nodes due to the acoustic radiation force driving both spray drops and particles into the pressure nodes. If the ultrasonic scrubber is used to treat industrial emissions, the analysis also estimated that if only particle-drop interactions are considered the scavenging coefficient can increase 15% to 18%, and if only particle-particle interactions are considered, the scavenging coefficient can increase 3% to 97%.

Appendices

Appendix A

Additional Data for some Figures in Chapter 2

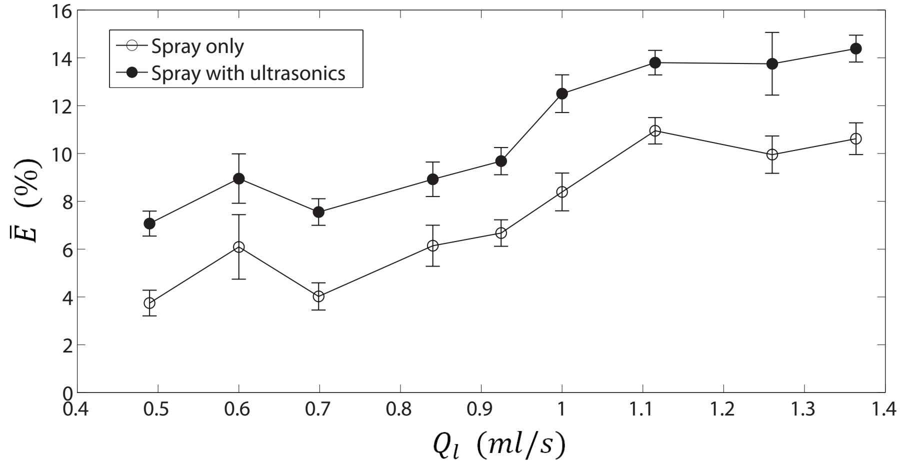

Figure A.1: Average scavenging coefficient $\bar{E}$ versus water flow rate Q_l for PSL particles. Open symbols represent runs without an ultrasonic standing wave field and filled symbols represent runs with an ultrasonic standing wave field. (This figure is samilar to Fig. 2.22 but with additional data points)

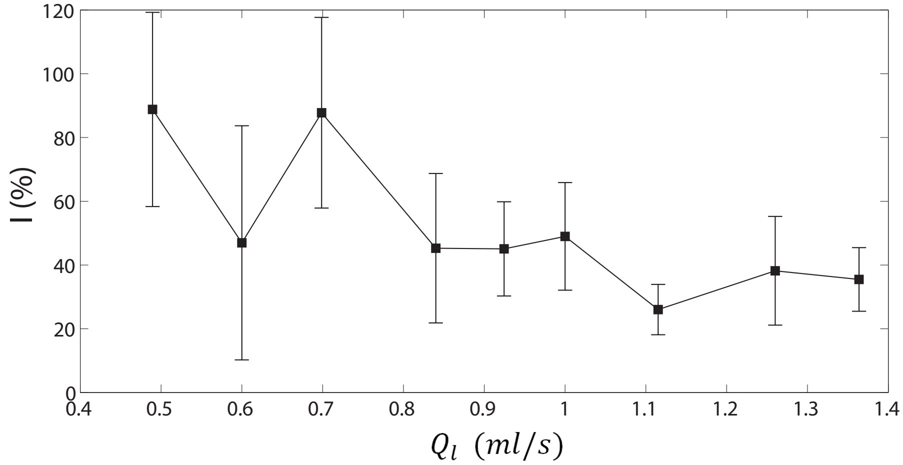

Figure A.2: Percent improvement of scavenging coefficient I versus water flow rate Q_l for PSL particles. (This figure is samilar to Fig. 2.22 but with additional data points)

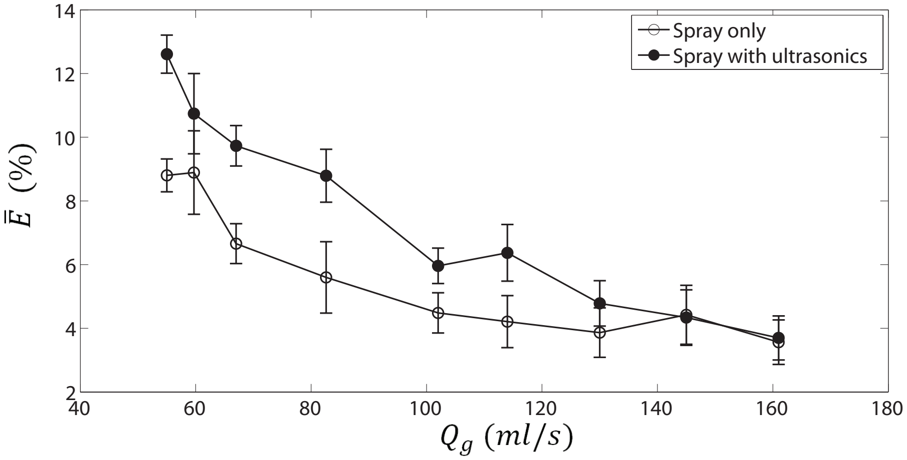

Figure A.3: Plot of the average scavenging coefficient $\bar{E}$ versus air flow rate Q_g of the ultrasonic wet scrubber for PSL particles. Open symbols represent runs without an ultrasonic standing wave field, and filled symbols represent runs with an ultrasonic standing wave field. (This figure is samilar to Fig. 2.27 but with additional data points)

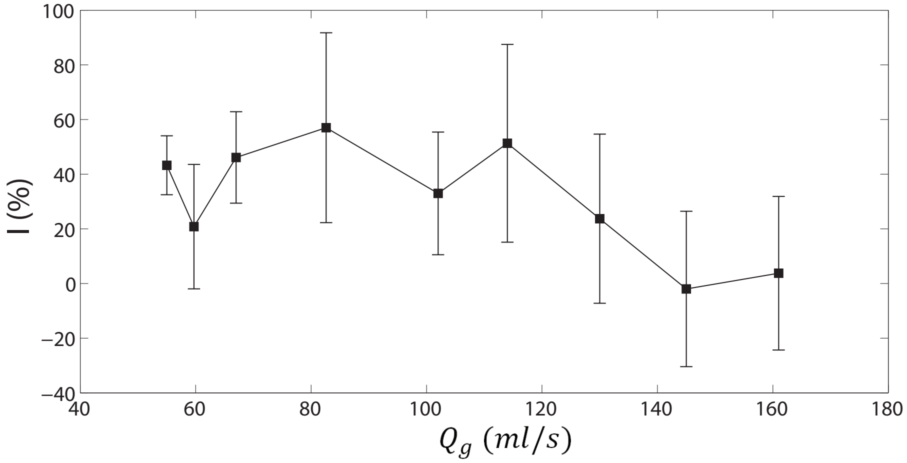

Figure A.4: Plot of the percent improvement of scavenging coefficient I versus air flow rate Q_g of the ultrasonic wet scrubber for PSL particles. (This figure is samilar to Fig. 2.28 but with additional data points)

Appendix B

Additional Data for some Figures in Chapter 4

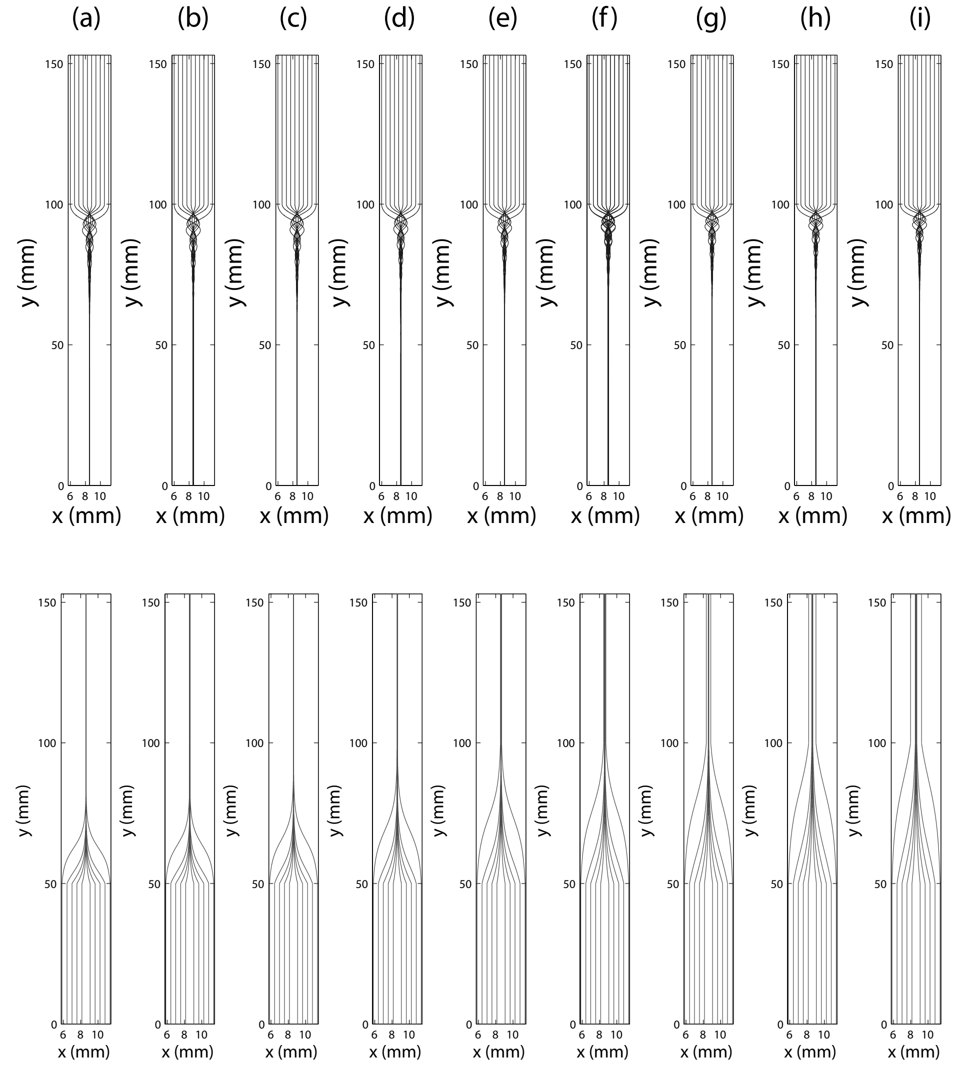

Figure B.1: The simulated trajectories of the spray drops (top) and the PSL particles (bottom) around a single pressure node under varying air flow velocity U_g. These air velocities were used in the scavenging experiments described in Chapter 2. (a) $U_g = 2.1$ cm/s. (b) $U_g = 2.5$ cm/s. (c) $U_g = 2.8$ cm/s. (d) $U_g = 3.4$ cm/s. (e) $U_g = 4.2$ cm/s. (f) $U_g = 4.7$ cm/s. (g) $U_g = 5.4$ cm/s. (h) $U_g = 6.0$ cm/s. (i) $U_g = 6.6$ cm/s. In these simulations, $d_p = 0.9$ μm and $d_d = 87$ μm. (This figure is similar to Fig. 4.7 but with additional air flow rates simulation results)

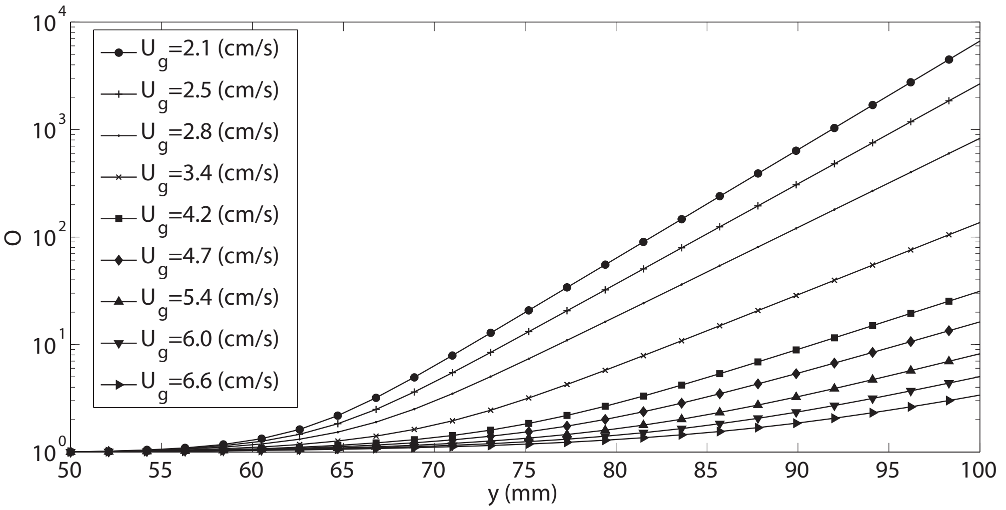

Figure B.2: The PSL particle concentration compression ratio versus y for different air velocities U_g when particle diameter $d_p = 0.9\mu$m. (This figure is similar to Fig. 4.9 but with additional data points)

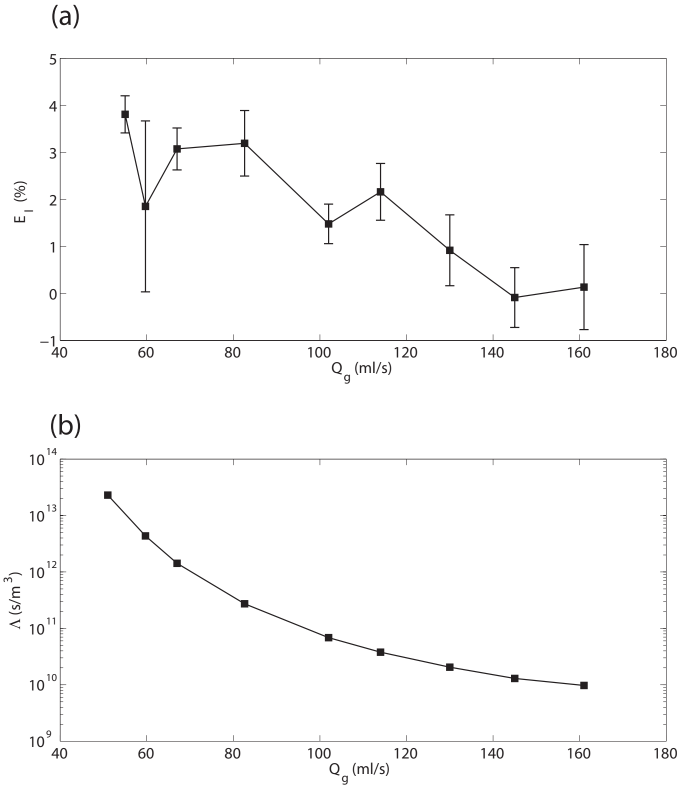

Figure B.3: Compare E_I and Λ versus air flow rate Q_g. (a) E_I versus Q_g. (b) Λ versus Q_g. (This figure is similar to Fig. 4.15 but with additional data points)

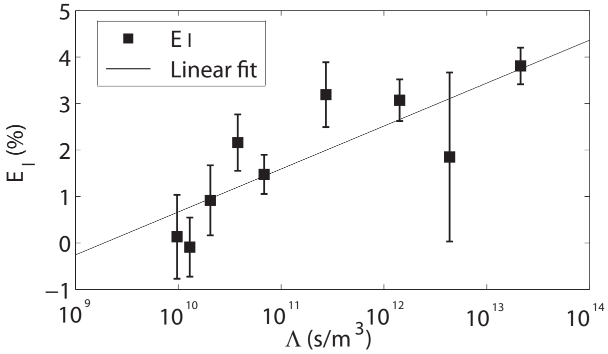

Figure B.4: Plot of E_I versus Λ for varying air flow rate Q_g (This figure is similar to Fig. 4.16 but with additional data points)

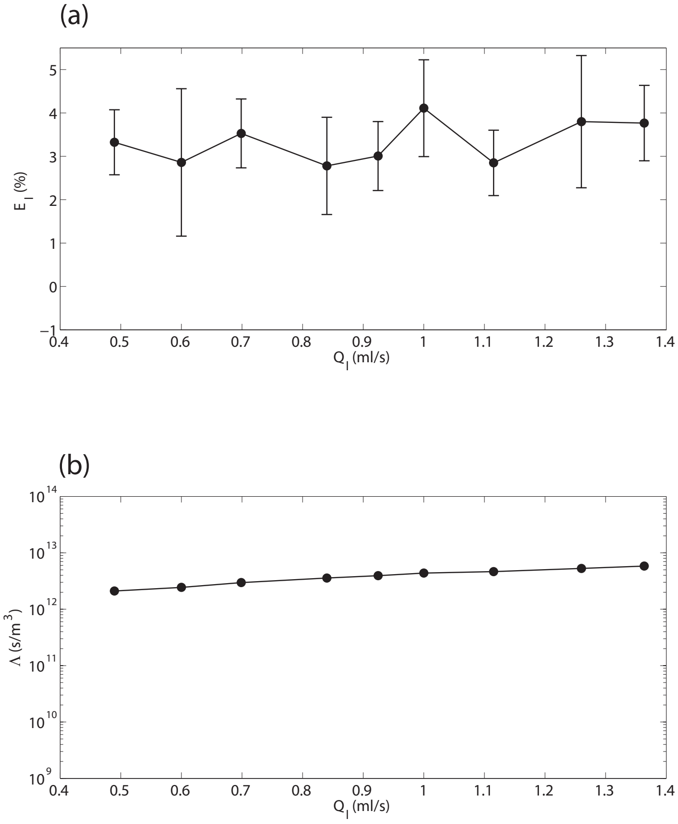

Figure B.5: Compare E_I and Λ versus water flow rate Q_l. (a) E_I versus Q_l. (b) Λ versus Q_l . (This figure is similar to Fig. 4.17 but with additional data points)

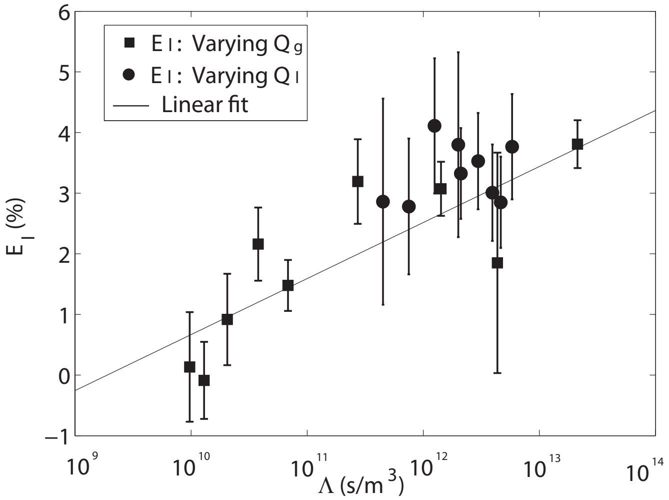

Figure B.6: Plot of E_I versus Λ for varying air flow rate Q_g and varying water flow rate Q_l. (This figure is similar to Fig. 4.18 but with additional data points)

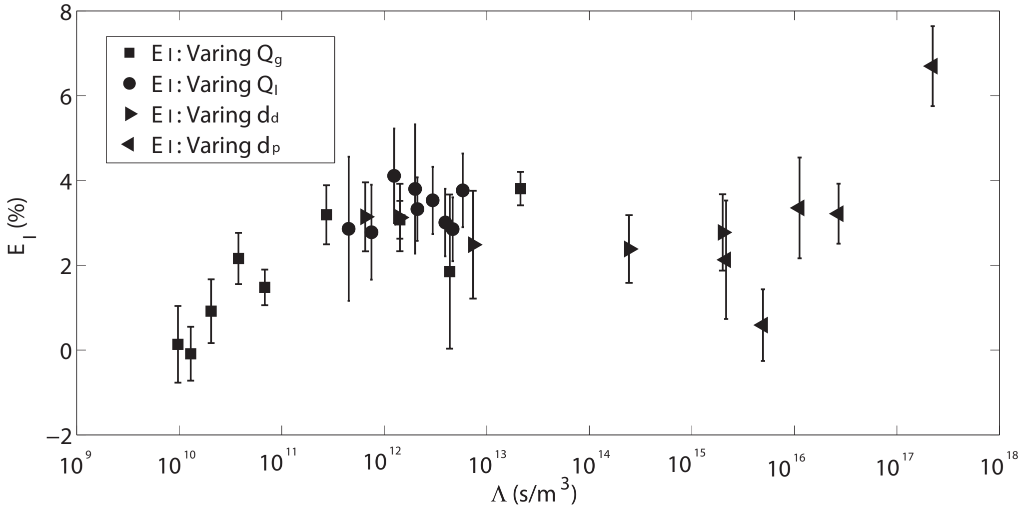

Figure B.7: Plot of I versus Λ for varying air flow rate Q_g, water flow rate Q_l, PSL particle size d_p and spray drop size d_d. (This figure is similar to Fig. 4.21 but with additional data points)

Bibliography

[1] W. G. Tucker. An overview of PM2.5 sources and control strategies. Fuel Processing Technology, 65-66:379–392, 2000.

[2] J. Schwartz. Why are people dying of on high air pollution days? Environ. Res., 64:26–35, 1994.

[3] D. L. Davis, M. L. Bell, and T. A. Fletcher. A look back at the Londion smog of 1952 and the half century since. Environ. Health Perspect., 110:A734–A735, 2002.

[4] T. Suwa, J. C. Hogg, K. B. Quinlan, A. Ohgami, R. Vincent, and S. F. van Eeden. Particulate air pollution induces progression of atherosclerosis. J. Am. Coll. Cardiol., 39:935–942, 2002.

[5] R. L. Verrier, M. A. Mittleman, and P. H. Stone. Air pollution: an insidious and pervasisve component of cardiac risk. Circulation, 106:890–892, 2002.

[6] C. A. Pope, R. T. Burnett, G. D. Thurston, M. J. Thun, E. E. Calle, D. Krewski, and J. J. Godleski. Cardiovascular mortality and long-term exposure to particulate air pollution. Circulation, 109:71–77, 2004.

[7] R. L. Johnson. Relative effects of air pollution on lungs and heart. Circulation, 109:5–7, 2004.

[8] A. J. Cohen. Outdoor air pollution and lung cancer. Environmental Health Perspectives, 108:743–750, 2000.

[9] C. A. Pope, M. J. Thun, M. M. Namboodiri, D. W. Dockery, J. S. Evans, F. E. Speizer, and C. W. Heath. Particulate air pollution as a predictor of mortality in a prospective study of U.S. adults. Am. J. Respir. Crit. Care Med., 151:669–674, 1995.

[10] C. A. Pope, R. T. Burnett, M. J. Thun, E. E. Calle, D. Krewski, K. Ito, and G. D. Thurston. Lung cancer, cardiopulmonary mortality, and long-term exposure to fine particulate air pollution. JAMA, 287:1132–1141, 2002.

[11] A. Seaton, W. MacNee, K. Donaldson, and D. Godden. Particulate air pollution and acute health effects. The Lancet, 345:176–178, 1995.

[12] J. Schwartz, D. Slater, T. V. Larson, W. E. Pierson, and J. Q. Koenig. Particulate air pollution and hospital emergency room visits for asthma in Seattle. Am. Rev. Respir. Dis., 147:826–831, 1993.

[13] D. W. Docker and C. A. Pope. Acute respiratory effects of particulate air pollution. Annu. Rev. Public Health, 15:107–132, 1994.

[14] H. Yi, X. Guo, J. Hao, L. Duan, and X. Li. Characteristics of inhalable particulate matter concentration and size distribution from power plants in China. Journal of the Air & Waste Management Association, 56(9):1243–1251, 2006.

[15] J.P. Pinto, A.S. Lefohn, and D.S. Shadwick. Spatial variability of PM2. 5 in urban areas in the United States. Journal of the Air & Waste Management Association, 54(4):440–449, 2004.

[16] J. Schwartz, F. Laden, and A. Zanobetti. The concentration-response relation between PM2.5 and daily deaths. Environmental Health Perspectives, 110(10):1025–1029, 2002.

[17] J. Heyder, J. Gebhart, G. Rudolf, Ch F. Schiller, and W. Stahlhofen. Deposition of particles in the human respiratory tract in the size range 0.005–15 μm. Journal of Aerosol Science, 17(5):811–825, 1986.

[18] A. Ogawa. Separation of particles from air and gases. CRC Press, Boco Raton, FL, USA, 1984.

[19] W. Strauss. Industrial gas cleaning: principles and practice of the control of gaseous and particulate emissions. Pergamon Press Inc., Elmsford, NY, 1975.

[20] H. S. Park, C. H. Jung, and K. W. Lee. Analytic solution for collection efficiency of electrostatic precipitators for polydisperse aerosols. Environmental Engineering Science, 21(4):451–461, 2004.

[21] M. Strand, J. Pagels, A. Szpila, A. Gudmundsson, E. Swietlicki, M. Bohgard, and M. Sanati. Fly ash penetration through electrostatic precipitator and flue gas condenser in a 6 MW biomass fired boiler. Energy & Fuels, 16(6):1499–1506, 2002.

[22] K. H. Yoo, J. S. Lee, and M. Do Oh. Charging and collection of submicron particles in two-stage parallel-plate electrostatic precipitators. Aerosol Science and Technology, 27(3):308–323, 1997.

[23] B. Raj Mohan, R. K. Jain, and B. C. Meikap. Comprehensive analysis for prediction of dust removal efficiency using twin-fluid atomization in a spray scrubber. Separation and Purification Technology, 63(2):269–277, 2008.

[24] T. Gemci and F. Ebert. Prediction of the particle capture efficiency based on the combined mechanisms by a 3-D simulation of a wet scrubber. Journal of Aerosol Science, 23:769–772, 1992.

[25] K. S. Lim, S. H. Lee, and H. S. Park. Prediction for particle removal efficiency of a reverse jet scrubber. Journal of Aerosol Science, 37(12):1826–1839, 2006.

[26] W. C. Hinds. Aerosol technology: Properties, behavior, and measurement of airborne particles. Wiley-Interscience, New York, NY, 1982.

[27] R. G. Stafford and H. J. Ettinger. Filter efficiency as a function of particle size and velocity. Atmospheric Environment (1967), 6(5):353–362, 1972.

[28] S. H. Kim and K. W. Lee. Experimental study of electrostatic precipitator performance and comparison with existing theoretical prediction models. Journal of Electrostatics, 48(1):3–25, 1999.

[29] H. T. Kim, C. H. Jung, S. N. Oh, and K. W. Lee. Particle removal efficiency of gravitational wet scrubber considering diffusion, interception, and impaction. Environmental Engineering Science, 18(2):125–136, 2001.

[30] K.W. Lee and B. Y. H. Liu. On the minimum efficiency and the most penetrating particle size for fibrous filters. Journal of the Air Pollution Control Association, 30(4):377–381, 1980.

[31] C. D. Cooper and F.C. Alley. Air pollution control: A design approach, volume 2. Waveland Press Prospect Heights, IL, 1994.

[32] K. Darcovich, K. Jonasson, and C. Capes. Developments in the control of fine particulate air emissions. Advanced Powder Technology, 8(3), 1997.

[33] K. Y. Lai, N. Dayan, and M. Kerker. Scavenging of aerosol particles by a falling water droplet. J. Atmos. Sci., 35:674–682, 1978.

[34] T. S. Pranesha and A. K. Kamra. Scavenging of aerosol particles by large water drops 1. Neutral case. J. Geophys. Res., 101:23,373–23,380, 1996.

[35] H. Zhao and C. Zheng. Stochastic algorithm and numerical simulation for drop scavenging of aerosols. Applied Mathematics and Mechanics, 27:1321–1332, 2006.

[36] S. M. Greenfield. Rain scavenging of radioactive particulate matter from the atmosphere. Journal of Meteorology, 14:115–125, 1957.

[37] T. Ferge, J. Maguhn, H. Felber, and R. Zimmermann. Particle collection efficiency and particle re-entrainment of an electrostatic precipitator in a sewage sludge incineration plant. Environmental science & technology, 38(5):1545–1553, 2004.

[38] L. V. King. On the acoustic radiation pressure on spheres. Proceedings of the Royal Society of London. Series A-Mathematical and Physical Sciences, 147(861):212–240, 1934.

[39] P. L. Marston and D. B. Thiessen. Manipulation of fluid objects with acoustic radiation pressure. Annals of the New York Academy of Sciences, 1027(1):414–434, 2006.

[40] L. P. Gor'Kov. On the forces acting on a small particle in an acoustical field in an ideal fluid. Soviet Physics Doklady, 6:773, 1962.

[41] T. Hasegawa and K. Yosioka. Acoustic-radiation force on a solid elastic sphere. The Journal of the Acoustical Society of America, 46(5B):1139–1143, 1969.

[42] M. Settnes and H. Bruus. Forces acting on a small particle in an acoustical field in a viscous fluid. Physical Review E, 85(1):016327, 2012.

[43] A. A. Doinikov. Acoustic radiation force on a spherical particle in a viscous heat-conducting fluid. I. General formula. The Journal of the Acoustical Society of America, 101:713, 1997.

[44] S. D. Danilov and M. A. Mironov. Mean force on a small sphere in a sound field in a viscous fluid. The Journal of the Acoustical Society of America, 107:143, 2000.

[45] R. Barnkob, P. Augustsson, T. Laurell, and H. Bruus. Acoustic radiation-and streaming-induced microparticle velocities determined by microparticle image velocimetry in an ultrasound symmetry plane. Physical Review E, 86(5):056307–056318, 2012.

[46] E. H. Trinh. Compact acoustic levitation device for studies in fluid dynamics and material science in the laboratory and microgravity. Rev. Sci. Instrum., 56:2059–2065, 1985.

[47] M.K. Hill, B.J. Brooks, S.J. Norris, M. H. Smith, I.M. Brooks, and G. De Leeuw. A compact lightweight aerosol spectrometer probe (CLASP). Journal of Atmospheric and Oceanic Technology, 25(11):1996–2006, 2008.

[48] K. T. Whitby and Y. H. Liu. Polystyrene aerosols-electrical charge and residue size distribution. Atmospheric Environment, 2:103–116, 1968.

[49] N. Ostu. A threshold selection method from gray-level histogram. IEEE Transactions on Systems, Man, and Cybernetics, 9:62–66, 1979.

[50] R. S. Figliola and D. E. Beasley. Theory and design for mechanical measurements. 2001.

[51] L.H. Princen and W.F. Kwolek. Coincidence corrections for particle size determinations with the coulter counter. Review of Scientific Instruments, 36(5):646–653, 1965.

[52] A. Hancock. Observation of forces on microparticles in acoustic standing waves. Master's thesis, University of California, Davis, 2001.

[53] L. E. Kinsler, A. R. Frey, A. B. Coppens, and J. V. Sanders. Fundamentals of acoustics. Fundamentals of Acoustics, 4th Edition, 1999.

[54] H. E. Bass, L. C. Sutherland, A. J. Zuckerwar, D. T. Blackstock, and D. M. Hester. Atmospheric absorption of sound: Further developments. The Journal of the Acoustical Society of America, 97(1):680–683, 1995.

[55] B. Widom. Line tension and the shape of a sessile drop. The Journal of Physical Chemistry, 99(9):2803–2806, 1995.

[56] S. Taneda. Experimental investigation of the wake behind a sphere at low Reynolds numbers. Journal of the Physical Society of Japan, 11(10):1104–1108, 1956.

[57] A.A. Zamyshlyaev and G.R. Shrager. Fluid flows past spheroids at moderate Reynolds numbers. Fluid Dynamics, 39(3):376–383, 2004.

[58] K.A. Hoffmann and S.T. Chiang. Computational Fluid Dynamics (Vol. 1). Wiley, 2000.

[59] W.C. Hinds. Aerosol technology: properties, behavior, and measurement of airborne particles. John Wiley & Sons, 1999.

[60] W.G.N Slinn. Precipitation scavenging. Atmospheric Science and Power Production, pages 466–532, 1984.

[61] E. Allen and P. Smith. A review of particle agglomeration. Surfaces, 85(86):87, 2001.

[62] E. Otto and H. Fissan. Brownian coagulation of submicron particles. Advanced Powder Technology, 10(1):1–20, 1999.

[63] K.W. Lee and H. Chen. Coagulation rate of polydisperse particles. Aerosol Science and Technology, 3(3):327–334, 1984.

[64] P.G. Shannon, L.J. Gorman and M. Reichel. Particulate Pollutant System Study: Fine Particle Emissions, Vol. II. U.S. Environmental Protection Agency, 2013.

[65] H. Czyz. On the concentration of aerosol particles by means of drift forces in a standing wave field. Acta Acustica united with Acustica, 70(1):23–28, 1990.

[66] P. J. Westervelt. The mean pressure and velocity in a plane acoustic wave in a gas. Acoustical Society of America Journal, 22:319–327, 1950.